

WL-TR-91-2067

AD-A243 391



DTIC  
ELECTE  
FEB 7 1991  
S C D



2

**RATES AND MECHANISMS OF METASTABLE  
DEACTIVATION OVER SURFACES**

W.T. RAWLINS, W.J. MARINELLI, A.M. WOODWARD,  
D. KAUFMAN, B.L. UPSCHULTE, and B.D. GREEN

Physical Sciences Inc.  
20 New England Business Center  
Andover, MA 01810

February 1991

Final Report for Period November 1985 to December 1988

Approved for public release; distribution unlimited.

91-17159



AERO PROPULSION AND POWER DIRECTORATE  
WRIGHT LABORATORY  
AIR FORCE SYSTEMS COMMAND  
WRIGHT-PATTERSON AIR FORCE BASE, OHIO 45433-6563

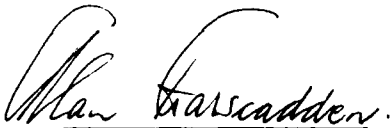
91 17 159

## NOTICE

When Government drawings, specifications, or other data are used for any purpose other than in connection with a definitely government-related procurement, the United States Government incurs no responsibility or any obligation whatsoever. The fact that the government may have formulated or in any way supplied the said drawings, specifications, or other data, is not to be regarded by implication, or otherwise in any manner construed, as licensing the holder, or any other person or corporation; or as conveying any rights or permission to manufacturer, use, or sell any patented invention that may in any way be related thereto.

This report is releasable to the National Technical Information Service (NTIS). At NTIS, it will be available to the general public, including foreign nations.

This technical report has been reviewed and is approved for publication.

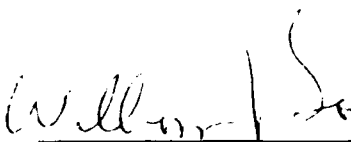


ALAN GARSCADDEN  
Power Components Branch  
Aerospace Power Division  
Aero Propulsion and Power Directorate



Chief, Power Components Branch  
Aerospace Power Division

FOR THE COMMANDER



WILLIAM U. BORGER  
Chief, Aerospace Power Division  
Aero Propulsion & Power Directorate

If your address has changed, if you wish to be removed from our mailing list, or if the addressee is no longer employed by your organization, please notify WL/POOC, WPAFB, OH 45433-6563 to help us maintain a current mailing list.

Copies of this report should not be returned unless return is required by security considerations, contractual obligations, or notice on a specific document.

UNCLASSIFIED

SECURITY CLASSIFICATION OF THIS PAGE

## REPORT DOCUMENTATION PAGE

1a. REPORT SECURITY CLASSIFICATION Unclassified			1b. RESTRICTIVE MARKINGS N/A since unclassified		
2a. SECURITY CLASSIFICATION AUTHORITY N/A since unclassified			3. DISTRIBUTION / AVAILABILITY OF REPORT Approved for public release; distribution unlimited		
2b. DECLASSIFICATION / DOWNGRADING SCHEDULE N/A since unclassified					
4. PERFORMING ORGANIZATION REPORT NUMBER(S) PSI-9561/TR-1101			5. MONITORING ORGANIZATION REPORT NUMBER(S) WL-TR-91-2067		
6a. NAME OF PERFORMING ORGANIZATION Physical Sciences Inc.		6b. OFFICE SYMBOL (if applicable)	7a. NAME OF MONITORING ORGANIZATION Aero Propulsion and Power Dir. (WL/POOC) Wright Laboratory		
6c. ADDRESS (City, State, and ZIP Code) 20 New England Business Center Andover, MA 01810			7b. ADDRESS (City, State, and ZIP Code) Wright Patterson AFB, OH 45433-6563		
8a. NAME OF FUNDING / SPONSORING ORGANIZATION Same as Monitoring Agency		8b. OFFICE SYMBOL (if applicable)	9. PROCUREMENT INSTRUMENT IDENTIFICATION NUMBER F33615-85-C-2561		
8c. ADDRESS (City, State, and ZIP Code)			10. SOURCE OF FUNDING NUMBERS		
			PROGRAM ELEMENT NO 61102F	PROJECT NO 2301	TASK NO S2
11. TITLE (Include Security Classification) Rates and Mechanisms of Metastable Deactivation Over Surfaces					
12. PERSONAL AUTHOR(S) W.T. Rawlins, W.J. Marinelli, A.M. Woodward, D. Kaufman, B.L. Upschulte, and B.D. Green					
13a. TYPE OF REPORT Final		13b. TIME COVERED FROM 11/15/85 to 12/15/88		14. DATE OF REPORT (Year, Month, Day) 1991 February	
15. PAGE COUNT 100					
16. SUPPLEMENTARY NOTATION					
17. COSATI CODES			18. SUBJECT TERMS (Continue on reverse if necessary and identify by block number)		
FIELD	GROUP	SUB-GROUP			
19. ABSTRACT (Continue on reverse if necessary and identify by block number)  The objective of this project was to investigate mechanisms of energy disposal in the quenching of rare-gas and molecular metastable species upon collisions with practical surfaces representative of plasma reactors. An apparatus was designed and constructed to generate a molecular beam of selected metastable species ( $\text{He}^*$ , $\text{Ar}^*$ , $\text{N}_2^*$ ) and impinge the beam on clean or gas-dosed surfaces in an ultra-high vacuum (UHV) chamber. The metastables were generated in a discharge-flow reactor, sampled and skimmed into a molecular beam, and directed into the UHV target chamber via two-stage differential pumping. The metastable intensity on target was in the range $10^8$ to $10^9$ metastables/s. A hemispherical, retarding potential electron energy analyzer was used to measure production rates and energy distributions of electrons ejected from the surface via the Penning ionization and Auger neutralization quenching mechanisms.					
20. DISTRIBUTION / AVAILABILITY OF ABSTRACT <input checked="" type="checkbox"/> UNCLASSIFIED/INLIMITED <input type="checkbox"/> SAME AS RPT <input type="checkbox"/> DTIC USERS			21. ABSTRACT SECURITY CLASSIFICATION Unclassified		
22a. NAME OF RESPONSIBLE INDIVIDUAL Dr. A. Garscadden			22b. TELEPHONE (Include Area Code) (513) 255-2923		22c. OFFICE SYMBOL WL/POOC

DD FORM 1473, 84 MAR

83 APR edition may be used until exhausted.  
All other editions are obsolete.

UNCLASSIFIED

SECURITY CLASSIFICATION OF THIS PAGE

In detailed experiments with a rough, polycrystalline, gas-covered Ni/NiO surface, the metastables  $\text{He}^*$ ,  $\text{Ar}^*$ , and  $\text{N}_2^*$  produced no detectable electron ejection, indicating electron ejection efficiencies  $< 10^{-8}$  for this surface. In contrast, impingement of UV photons on the same surface generated copious electron ejection.

The absence of significant electron ejection from metastable impingement is quite unexpected in light of previous investigations of this process for polished, high-purity, oriented single crystals. The present results suggest that, in practical systems, effects of adsorbates and surface roughness dominate the metastable-surface interaction, and surface electron ejection is not a significant energy disposal mechanism. These results also demonstrate that UV photon impingement can provide an efficient source of secondary electrons near reactor walls.

NTIS GRA&I	<input checked="" type="checkbox"/>
DTIC TAB	<input type="checkbox"/>
Unannounced	<input type="checkbox"/>
Justification	
By _____	
Distribution/	
Availability Codes	
Dist	Avail and/or Special
A-1	



## TABLE OF CONTENTS

<u>Section</u>	<u>Page</u>
1. INTRODUCTION . . . . .	1
1.1 Objectives and Program Summary . . . . .	1
1.2 Observations of Metastable-Surface Interactions . . . . .	4
1.3 General Technical Approach . . . . .	13
2. EXPERIMENTAL APPARATUS DESIGN AND OPERATION . . . . .	15
2.1 Metastable Production . . . . .	16
2.2 Vacuum Chamber Design . . . . .	23
2.3 Pumping Requirements . . . . .	27
2.4 Diagnostics in UHV Chamber . . . . .	32
3. MEASUREMENT RESULTS . . . . .	48
3.1 Metastable Generation and Flux Measurements . . . . .	48
3.2 Secondary Electron Flux Measurement . . . . .	57
4. DISCUSSION AND RECOMMENDATIONS . . . . .	68
5. REFERENCES . . . . .	71
APPENDIX A: RETARDING POTENTIAL RAMP GENERATOR FOR ELECTRON ANALYZING SYSTEM . . . . .	75
APPENDIX B: COLLISIONAL QUENCHING OF ATOMS AND MOLECULES ON SPACECRAFT THERMAL PROTECTION SURFACES . . . . .	83

## LIST OF ILLUSTRATIONS

<u>Figure</u>	<u>Page</u>
1    Some metastable quenching mechanisms on surfaces . . . . .	5
2    Machine drawing showing assembly of all three chambers . . . . .	15
3    Schematic of source chamber with flow reactor . . . . .	17
4    Design drawing of the discharge flow tube source, showing gas inlet ports and vacuum-to-air seals . . . . .	17
5    Beam intensity on target as a function of source-to-target distance and source aperture, $d_0$ , for a beam diameter on target of 5 mm . . . . .	23
6    Side viewing schematic drawing of the UHV chamber showing location of diagnostics . . . . .	24
7    Schematic drawing of the UHV chamber viewed along beam axis showing location of drag . . . . .	24
8    Diagram of vacuum system . . . . .	27
9    Logic diagram for vacuum system control and safety interlock circuitry . . . . .	28
10   Pressure in source chamber as a function of flow tube aperture, $d_0$ , for an 8-in. throat diffusion pump and 3 torr of He in the source . . . . .	29
11   Pressure in the intermediate chamber as a function of source to target distance and source aperture, $d_0$ , for the Edwards series 63 diffusion pump . . . . .	30
12   Pressure in the UHV chamber as a function of source-to-target distance, source aperture, $d_0$ , and pump speed . . . . .	31
13   Schematic drawing of the energy analyzer assembly . . . . .	35
14   Side views . . . . .	36
15   Optical detection system as originally implemented . . . . .	39

## LIST OF ILLUSTRATIONS (Continued)

<u>Figure</u>	<u>Page</u>
16 Improved optical detection system . . . . .	40
17 Schematic drawing of quadrupole assembly . . . . .	42
18 Helium flow velocity as a function of pressure in the flow tube . . . . .	50
19 Configuration for electron multiplier beam diagnostics tests . . . . .	50
20 Electron multiplier current versus flow rate of N <sub>2</sub> added downstream, Ar discharge . . . . .	52
21 Electron multiplier current versus multiplier supply voltage, Ar discharge . . . . .	53
22 Electron multiplier current versus discharge gas pressure, Ar discharge . . . . .	54
23 Electron multiplier current versus discharge voltage, Ar discharge . . . . .	54
24 N <sub>2</sub> (C→B) flame intensity versus discharge current, Ar discharge + downstream N <sub>2</sub> . . . . .	55
25 Mass spectrum of baked UHV chamber . . . . .	58
26 Mass spectrum of UHV chamber with helium beam coming into chamber . . . . .	59
27 Mass spectrum of UHV chamber with helium molecular beam coming into chamber . . . . .	60
28 Electrical circuit for metastable data collection . . . . .	61
29 Mercury lamp signal from energy analyzer . . . . .	62
30 Mercury lamp signal from energy analyzer . . . . .	63
31 Laser light focused onto Ni target, $\lambda = 245$ nm . . . . .	64

## PREFACE AND ACKNOWLEDGEMENTS

### Acknowledgements

The authors are grateful for the technical contributions of several individuals at Physical Sciences Inc. (PSI). H.C. Murphy and A. Urban contributed to the design and assembly of the apparatus. L.G. Piper provided invaluable assistance in the design and evaluation of the discharge source. G.E. Caledonia and A. Gelb contributed to many discussions of measurement concepts and interpretations of the results. We are especially grateful to Prof. John Yates of the University of Pittsburgh, who provided extensive consultation on all aspects of the program, and who provided the design concept and fabrication of the hemispherical electron energy analyzer.



## 1. INTRODUCTION

### 1.1 Objectives and Program Summary

The fate of metastable energy carriers has become of interest in a number of applications in recent years, ranging from transfer and electric discharge lasers, to upper atmospheric chemistry, to surface deexcitation, heat transfer, and erosion. Of current interest are the kinetics of the interactions of electron-laser cavities or plasma sprayers. This is the Final Report on an experimental program dedicated to investigations of the rates and mechanisms of metastable deactivation on practical surfaces.

Experiments involving ultraclean surfaces under ultrahigh vacuum (UHV) conditions provide insight into the classes of fundamental mechanisms which operate at surfaces. Several groups have been involved in the pioneering work in metastable quenching on surfaces. These include researchers at the University of Pittsburgh,<sup>1-3</sup> the University of California (Santa Barbara),<sup>1-3</sup> the University of Tokyo,<sup>4,5</sup> C.E.N.S. (France),<sup>6</sup> Bell Laboratories,<sup>7</sup> and the University München and Freiburg (Germany).<sup>8,9</sup> We will briefly summarize below some of the relevant conclusions from these studies. In strong contrast to the operating conditions in those studies, discharge laser or plasma systems operate under much higher pressure conditions and are constructed of materials such as stainless steel, quartz, pyrex, and teflon. Thus, a mixture of these fundamental processes and additional mechanisms, such as interactions with adsorbates, may dominate the macroscopic degradation or quenching processes during real device operation. Additionally, these practical systems involve complex molecular species and radicals. The interaction of these molecular metastables with surfaces has not been studied to date. Most studies have focused on the

interaction of rare gas metastables such as  $\text{He}^*$  with surfaces. Finally, for plasma processing reactions, both silicon surfaces and semiconductor processing species such as  $\text{NF}_3$ , or  $\text{Si}_2\text{H}_6$ , must be considered.

The basic objective of this research program was to examine the kinetics and mechanisms of metastable energy transfer to practical surfaces as might be encountered in plasma reactors (e.g., quartz, pyrex, stainless steel, teflon). The phenomena of interest include metastable quenching efficiencies, product energy partitioning, effects of metastable energetics and internal modes, and effects of the surface material, with and without adsorbate species. To this end, we designed and constructed an ultrahigh vacuum molecular beam apparatus to diagnose scattered metastables, electrons, and fluorescing species produced in the interaction of discharge-produced atomic and molecular metastables with a variety of clean and dosed surfaces. This apparatus was constructed specifically for this project. Although Physical Sciences Inc. (PSI) purchased a major portion of the capital equipment necessary to build the apparatus, much of the program's effort was devoted to apparatus development. In later stages of the program, this effort benefitted from a synergistic relationship with a NASA-funded investigation of atom recombination on a variety of surfaces.

Although the apparatus was constructed and operated to obtain data, the planned measurements were only partially successful for several reasons. Principally, the apparatus hardware components and construction labor required a much larger fraction of the planned cost than was originally anticipated. In addition, two principal diagnostics produced negative results which were unexpected. First, laser photoionization, the principal diagnostic for incoming and scattered metastable species, proved to be very difficult to implement with

adequate sensitivity, due to scattered light effects. Second, the electron collection and energy analysis system, which was the principal diagnostic for energetic products of the metastable-surface interaction, saw essentially no electron ejection from the interactions of  $\text{He}^*$ ,  $\text{Ar}^*$ , or  $\text{N}_2^*$  metastables with a Ni/NiO surface. This result was completely unexpected in view of previous work, and we continued with a series of tests to determine whether the problem was due to surface contamination, failure of the electron detection system, or inadequate delivery of metastables in the molecular beam. These tests showed that the electron detection and metastable generation/delivery systems were functioning as expected. In particular, we were able to establish that an adequate flux of metastables was generated by the discharge source and extracted into the molecular beam.

We therefore conclude that, although the surface was bombarded by a significant flux of energetic species, no electrons escaped the surface. The electron ejection efficiency was bounded as less than  $10^{-8}$ . This could have been due to a combination of effects, including surface contamination initially present following pumpdown, the presence of oxidized layers, and surface roughness induced by repeated cleaning procedures (argon-ion bombardment). Clearly, the best way to confirm these mechanisms would be to perform measurements reproducing the high-purity single-crystal work of previous investigations. Unfortunately, such measurements could not be carried out within the cost constraints of the subject contract.

The clear implication of these results is that the macroscopically roughened surfaces covered with adsorbates found in plasma processing systems will likely have negligible electron production at the walls due to metastable quenching. However, photon production of electrons appears to be quite efficient even for these rougher adsorbate covered surfaces.

The following subsections discuss the relevant background of the dynamics of metastable-surface interactions and energy disposal, and the technical approach adopted for this project. Subsequent sections describe the design and operation of the experimental apparatus, the results of the initial beam-surface measurements, and the diagnostic tests of the system performance.

## 1.2 Observations of Metastable-Surface Interactions

Several deexcitation processes of metastable states of atoms approaching surfaces are possible depending upon the relative energy levels involved. These processes have been thoroughly discussed in the literature and will only be summarized here. They are shown schematically in Figure 1. One of the most studied mechanisms to date involves a two-step process, resonance ionization of the metastable followed by Auger neutralization (RI + AN). The spectra of ejected electrons have proven to be a highly sensitive probe of surface electronic structure.

The RI + AN mechanism for deexcitation is anticipated when the metastable ionization potential,  $E_i$ , is less than the surface work function,  $\phi$ . This implies that the excited metastable electron may resonantly tunnel into vacant conduction levels in the surface. This process should be rapid ( $10^{-14}$ s) when the metastable is in the vicinity (within a few angstroms) of the surface. The AN step occurs by transferring an electron from the valence bands into the ground state level of the atom and simultaneously ejecting a valence electron from the surface (see Figure 1b). The ejected electron spectrum from the RI + AN process reflects both the excitation energies and the density of states in the substrate. Observed distributions are broad but peaked near  $E_{\text{max}}$ , the maximum allowed

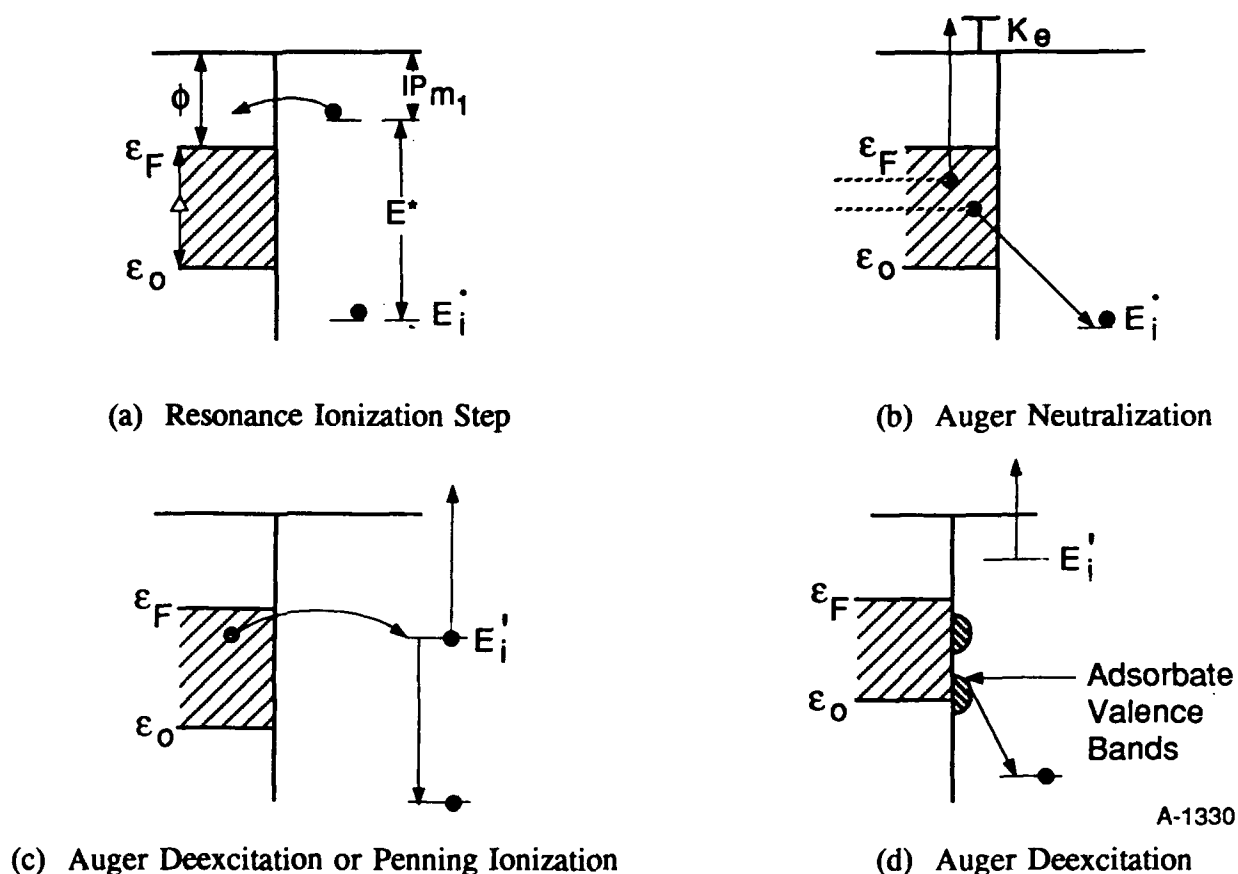


Fig. 1. Some metastable quenching mechanisms on surfaces

electron energy.<sup>1</sup> A number of experimental measurements have acquired electron energy spectra for He metastable quenching (or ion neutralization) over a variety of metal surfaces such as Ni(100),<sup>7</sup> Ni(111)<sup>1-3,6</sup> Pd(111),<sup>8</sup> Pd(110),<sup>9</sup> and Mo(110).<sup>10</sup> Very carefully designed experiments have determined that He metastables are very efficiently quenched (with near unit efficiency) on clean Ni surfaces.<sup>6</sup> Photons and fast atoms were also observed and the authors inferred that ~ 17 percent of metastables striking the surface led to secondary electron ejection.<sup>6</sup>

In the RI + AN process, the first step involves resonant tunneling of the excited metastable electron into vacant surface levels. In the second step, the Auger neutralization, a

surface electron fills the lowest ion level and an electron is ejected from the surface. The maximum kinetic energy of an ejected electron,  $K_{\text{emax}}$ , is given by

$$K_{\text{emax}} = E_i - \Delta E_i - 2\phi$$

where  $E_i$  is the lowest unoccupied metastable level,  $\Delta E_i$  is the shift of  $E_i$  due to the interaction of its ion with the surface, and  $\phi$  is the surface work function. For the present purpose it is sufficient to write this equation as

$$K_{\text{emax}} = \text{IP} - 2\phi \text{ (RI + AN)}$$

where IP is the ionization potential of the ground state atom. Values of  $K_{\text{emax}}$  for  $\text{He}^*$ ,  $\text{Ar}^*$ , and  $\text{Xe}^*$  are listed in Table 1 for Ni(111) surfaces ( $\phi = 5.3$  eV). It is clear that for atoms (or molecules) with lower ionization potentials or surfaces of high work function, this mechanism cannot be effective in producing ejected electrons.

The intriguing study of Harada et al.<sup>4</sup> provided an experimental verification that semiconductor materials (i.e., amorphous and trigonal selenium) also quench metastables via

TABLE 1. Energetics of atomic rare-gas metastables.

		Metastable Energy (eV)	Ground State IP	$K_{\text{emax}}$ (SiO <sub>2</sub> ) $\phi = 5$ eV	$K_{\text{emax}}$ (eV) (Ni(111)) $\phi = 5.3$ eV
He	$3P_0(1S)$	20.6	24.5	14.5	13.9 (RI + AN)
	$3P_2(3S)$	19.8			
Ar	$3P_0(1S)$	11.7	14.0	4.0	3.4 (RI + AN)
	$3P_2(3S)$	11.5			
Xe	$3P_0(1S)$	9.4	12.1	2.1	1.5 (RI + AN)
	$3P_0(3S)$	8.3			

a RI + AN process as long as the metastable ionization energy falls within the conduction band. A Se film (on stainless steel) was shown to deexcite  $\text{He}(^1\text{S}, ^3\text{S})$  and  $\text{Ne}(^3\text{P})$ , whose values of  $E_i'$  lie well above the work function for Se which is 6.0 eV. No experiments of this nature have been carried out using the materials of interest to this program.

Another two-step mechanism involves resonant ionization of the metastable into vacant surface states above the filled band states followed by resonant neutralization of the metastable ion by filled band states. This mechanism does not produce ejected electrons. It should contribute when the metastable ionization potential is less than the surface work function and the atom ground state level lies within the filled bands.

If the vacant surface conduction bands are not accessible to the metastable excited electron (either if  $E_i'$  falls below the Fermi level or if these are adsorbed species), then a single step Auger Deexcitation (AD) or Penning Ionization (PI) process can likely occur. In this process, as shown in Figure 1c, the hole in the ground state of the incoming species is filled by an Auger electron from an occupied surface state which overlaps the hole state. The metastable state electron is ejected with an energy determined by the Auger transition.

Several AD (or PI) deexcitation mechanisms similar to the ultraviolet photoelectron spectra (UPS) are also possible. In these interactions the metastable acts as an excitation source, transferring its energy to the surface. If this energy is sufficiently large, then electrons may be ejected. Note that if the excitation energy is less than the work function, electrons cannot be ejected. These mechanisms should be operative when the metastable ionization potential is greater than the surface work function. This would seem to be the case for most molecular metastables (in contrast to the rare-gas metastables).

It has been demonstrated experimentally that when species are chemisorbed on metal surfaces, the surface conduction bands are shielded from the incoming metastable so that PI is likely to occur rather than the RI + AN processes.<sup>1-3,6-9</sup> The adsorbate valence levels can then supply the electron to the incoming metastable (see Figure 1d). The energy of the Auger transition (and the resulting ejected electron kinetic energy) is specific to the adsorbate, its surface bonding and the metastable energy levels. Specifically there are resonance peaks in the ejected electron spectrum corresponding to electronic transitions in the adsorbate, in addition to a low energy inelastic scattering peak. This phenomenon has been shown experimentally for CO and NO adsorbed on metal surfaces. There is competition between the two processes as surface coverage is increased, but at less than a monolayer, PI resonance peaks are observable and at 1.6 monolayer coverage the RI + AN high energy peak is no longer observable. The degree of shielding depends on the nature of the CO (or NO) absorption. For strongly adsorbed molecules (such as CO bridge bonded between two Ni atoms) the RI + AN process is observed. The adsorbate valence shells do not protrude out into the gas phase far enough to prevent the RI electron jump.<sup>1</sup> When the adsorbate is bonded on top of a Ni atom, the valence shells extend just far enough to supply the electron to the incoming metastable hole before the metastable excited electron can jump to the conduction bands. Consequently the PI (Figure 1c) and not the RI + AN (Figures 1a and 1b) process occurs under these conditions.

These changes are sensitively reflected in the ejected electron kinetic energy spectrum as demonstrated by Bozso et al.,<sup>1-3</sup> Harada et al.,<sup>4</sup> and Conrad et al.<sup>8,9</sup> Thus metastable quenching is extremely sensitive to the outermost surface layer. This sensitivity vividly



demonstrates that extrapolation of these observations for single cleaved clean crystals or even clean amorphous Se to the surfaces of current interest is not advisable.

Metastable species which are active in plasma and discharge processes also include molecular metastables (such as  $N_2(A)$ ,  $CO(a)$ ,  $O_2^1\Delta$ ,  $NF^1\Delta$ , and atomic metastables (such as  $N(^2D)$ ,  $N(^2P)$ , and  $O(^1D)$ ,  $(^1S)$ ). These metastables still have several eV of energy but much less energy than the 20.6 eV available from  $He(2^1S)$ , the 19.8 eV from  $He(2^3S)$ , or the 16.7 eV available from  $Ne(^3P_0)$  which have been the metastables most studied to date. These less energetic metastables will of necessity undergo different deexcitation mechanisms depending on the surface electronic structure.

In all cases it should be noted that electron ejection can only occur when the excitation of the metastable exceeds the work function of the surface. For most surfaces of interest, e.g., Si, Ge,  $SiO_2$ , Ni, etc., work functions are typically near 5 eV.<sup>11</sup> Rare-gas metastable atoms are quite unusual in that they carry a large amount of excitation energy ( $He^*$ , 20.6 eV, and  $Ar^*$ , 11.7 eV) and also because their metastable levels lie within a few eV of the ionization limit ( $He^*$ , 3.9 eV, and  $Ar^*$ , 2.3 to 2.5 eV). Most molecular metastables do not carry nearly as much excitation energy as  $He^*$  ( $CO$  has 6 eV,  $N_2$  has 6 to 8 eV, and  $H_2$  has 11.9 eV) and their metastable ionization potentials,  $IP_m$ , are considerably larger ( $CO$ ,  $IP_m = 8$  eV and  $N_2$ ,  $IP_m = 7$  to 9 eV). Thus for most molecular metastables, the  $RI + AN$  seems less likely than for  $He^*$ .  $PI$  or  $AD$  mechanisms are more probable. Additionally, the lower energy content of most molecular metastables will shift the electron spectra to lower energies (assuming ejection is possible). The ionization potentials and metastable excitation energies for  $H_2$ ,  $N_2$ , and  $CO$  are given in Table 2.

TABLE 2. Energetics of some molecular metastables.

	Metastable Energy (eV)	Molecular IP (eV)	K <sub>emax</sub> (eV) (SiO <sub>2</sub> )	K <sub>emax</sub> (eV) (Ni(111))
H <sub>2</sub> C <sup>3</sup> Π <sub>u</sub>	11.9	15.4	5.4	4.8
N <sub>2</sub> A <sup>3</sup> Σ <sub>u</sub> <sup>-</sup>	6.2	15.6	1.2	(RI + AN)
a <sup>1</sup> Π <sub>g</sub>	8.6		3.6	0.9 (AD)
a' <sup>1</sup> Σ <sub>u</sub> <sup>-</sup>	8.4		3.4	3.3 (AD)
W <sup>3</sup> Δ <sub>u</sub>	8.4		2.4	3.1 (AD)
CO a <sup>3</sup> Π	6.0	14.0	1.0	2.1 (AD)
				0.7 (AD)

Molecules also have additional degrees of freedom available which can be excited in the quenching process, including vibration and rotation. Indeed, nonthermal energy partitioning has been observed in scattering of molecular metastables off surfaces.<sup>12</sup> Finally, the molecules could reactively quench in the interaction with adsorbed species if the metastable energy overcomes activation barriers for reaction with the surface. These additional reaction pathways and the lower molecular metastable energies both act necessarily to reduce the amount of and maximum energy for electron ejection, the primary diagnostic for atomic metastable quenching.

Thus by first studying He\* and then subsequently Ar\* (11.6 eV), and Xe\* (8.3 eV), it should be possible to determine trends for quenching paths as a function of metastable energy. Similar investigations for molecular metastables could observe the effects of additional internal degrees of freedom in molecules.

The excitation energy of  $H_2$  is approximately 3.5 eV below the ionization energy and  $RI + AN$  is a possible mechanism for deexcitation of the metastable  $H_2$  on many semiconductor surfaces (i.e.,  $\sim 5$  eV). For  $H_2$  we estimate the value of  $K_{\text{emax}}$  to be similar to that of  $Ar^*$ , i.e., for values of  $\phi \sim 5$  eV, characteristic of Si and Ge,  $K_{\text{emax}} \sim 5$  eV.

Thus  $H_2^*$  offers an excellent transition case from atomic metastables to molecular ones. However, several complications may occur. In particular, the Auger neutralization process may result in a highly vibrationally excited final state of the ground state of the molecule if the charge exchange occurs via a Franck-Condon type mechanism. This is because the equilibrium distances of  $H_2$  and  $H_2^+$  are quite different

$$\left( R_{eH_2} = 0.74 \text{ \AA} \text{ and } R_{eH_2^+} = 1.05 \text{ \AA} \right).$$

The partitioning of energy into vibration will reduce (perhaps substantially) the maximum kinetic energy of the ejected electrons.

For molecules such as CO and  $N_2$  the excitation levels lie below the Fermi level for most metals and semiconductors. For CO the ionization potential of the metastable is 8 eV and for  $N_2$  between 7.1 and 9.4 eV. Thus, an  $RI + AN$  mechanism is not anticipated. In this case, the work function is less than the ionization potential of the metastable, and AD may be the operational mechanism.

Such a process could produce ejected electrons if the excitation energies are sufficient. For CO and  $N_2$ , the excitation energies are only 1 to 3 eV above typical values of work functions ( $\phi \sim 5$  eV). Additionally, as for  $H_2$ , the available energy may be substantially reduced by molecular excitation. The situation is further complicated for CO and  $H_2$  by the strong chemisorption energies of the molecules on many surfaces ( $\sim 2$  to 3 eV). It seems reasonable to expect that these molecules are unlikely to yield as many or as energetic ejected electrons as the metastable He, and molecular internal excitation may become a significant portion of the quenched metastable energy.

An important factor in excited state-surface interactions in practical systems is the effect of adsorbate coverage of the surface of interest. Adsorbate valence states would act to interfere with the Penning and Auger processes, as illustrated in Figure 1d. Adsorbate species can arise from intrinsic system impurities, as well as from operating gases within the system. Thus it is important to be able to study the metastable-surface interactions both in the absence of adsorbed species and in the presence of selected adsorbates with systematically controlled surface coverage.

We have limited our discussion here to the more energetic molecular metastables. In discharges involving  $\text{NF}_3$ ,  $\text{NF}^1\Delta$  (1.1 eV) is undoubtedly formed. Other low energy metastables may be formed in large enough concentrations in laser and plasma reactors that they may contribute to surface erosion or heating.

The erosion or surface changes produced by these metastables is hard to predict. Ions traveling at large kinetic energies produce light (impact flash) and eject surface material (sputtering). Neutrals traveling at high velocities have also been shown to produce photon emission.<sup>13-15</sup> The deexcitation of the more energetic rare-gas atoms ( $\text{He}^*$ ) on teflon surfaces could result in surface bond rearrangement or surface atom or free radical ejection. Teflon coatings have been used to coat the walls of flow reactors containing active nitrogen-argon mixtures. Slow macroscopic changes are observed near the discharge excitation source. The teflon coating material seems to be removed after long exposure. The observations have not been quantified. The erosion source may be ions, electrons, or metastables. For example, many radiative species have been observed during the interaction between microwave excited gases and solids, for example, Ref. 16 and references therein. Many of these radiating species have been identified as produced via the reaction of

discharge produced atoms, such as O and H, and the surface. No analysis of species produced through metastable interaction appears available.

With these concepts as a basis, we have developed a conceptual design for an experimental apparatus which would permit accurate rates and reaction pathways to be determined. The overall technical approach is described in the next subsection.

### 1.3 General Technical Approach

Our overall technical approach to the study of metastable-surface energy transfer was to perform the experimental measurements in an environment where the characteristics of the surfaces could be well controlled. This requires the use of ultrahigh vacuum to control surface cleanliness, and the use of molecular beam techniques to deliver controlled fluxes of selected metastable species to the target surface. Hence, we designed and constructed an apparatus consisting of three basic sections: a differentially pumped metastable source and molecular beam production chamber; a differentially pumped intermediate chamber to reduce the gas load; and an ultrahigh vacuum (UHV) target chamber containing the sample of interest, means for surface manipulation and preparation, and diagnostics.

To generate the metastable species of interest, we selected a DC discharge-flow technique which is capable of cleanly producing metastable electronic states of He, Ar, and H<sub>2</sub> without complications from impurities, ions, ultraviolet scattered light, or molecular dissociation. Metastable species, prepared in the discharge-flow reactor, pass into the target chamber through a series of small orifices which create a collimated flux of metastables (and bath gas) on the surface.

The principal diagnostic was a hemispherical electron energy analyzer to detect electrons ejected from the surface. In addition, a quadrupole mass spectrometer detected background gas purity, and we attempted to use multi-photon ionization by a pulsed tunable dye laser to detect the incoming and reflected metastable species.

Target surfaces were mounted on a UHV sample manipulator, and were cleaned in the UHV environment by ion bombardment and thermal desorption. An Auger electron spectrometer monitored surface composition following each cleaning.

The primary surfaces of interest were nickel and quartz; other surfaces considered were pyrex, silicon, stainless steel, and teflon. The primary metastables of interest were  $\text{He}(2^3\text{S}, 2^1\text{S})$ ,  $\text{Ar}(^3\text{P}_{2,0})$ ,  $\text{N}_2(\text{A}^3\Sigma_u^+)$ , and  $\text{CO}(\text{a}^3\Pi)$ . These species can be generated cleanly and selectively by well-established discharge-flow/energy transfer methods as described later.

In the next section, we describe in detail the design and operation of the experimental apparatus.

## 2. EXPERIMENTAL APPARATUS DESIGN AND OPERATION

The overall apparatus consists of three interconnected vacuum chambers as shown in Figure 2. The metastable beam is generated by supersonic expansion from a discharge-flow reactor into a series of differentially pumped chambers. The beam impinges on the target surface in a high-cleanliness, ultrahigh vacuum chamber equipped with extensive diagnostic capability. In the following subsections, we describe in detail the design of each component of the apparatus, and the design rationale for production and propagation of the metastable beam.

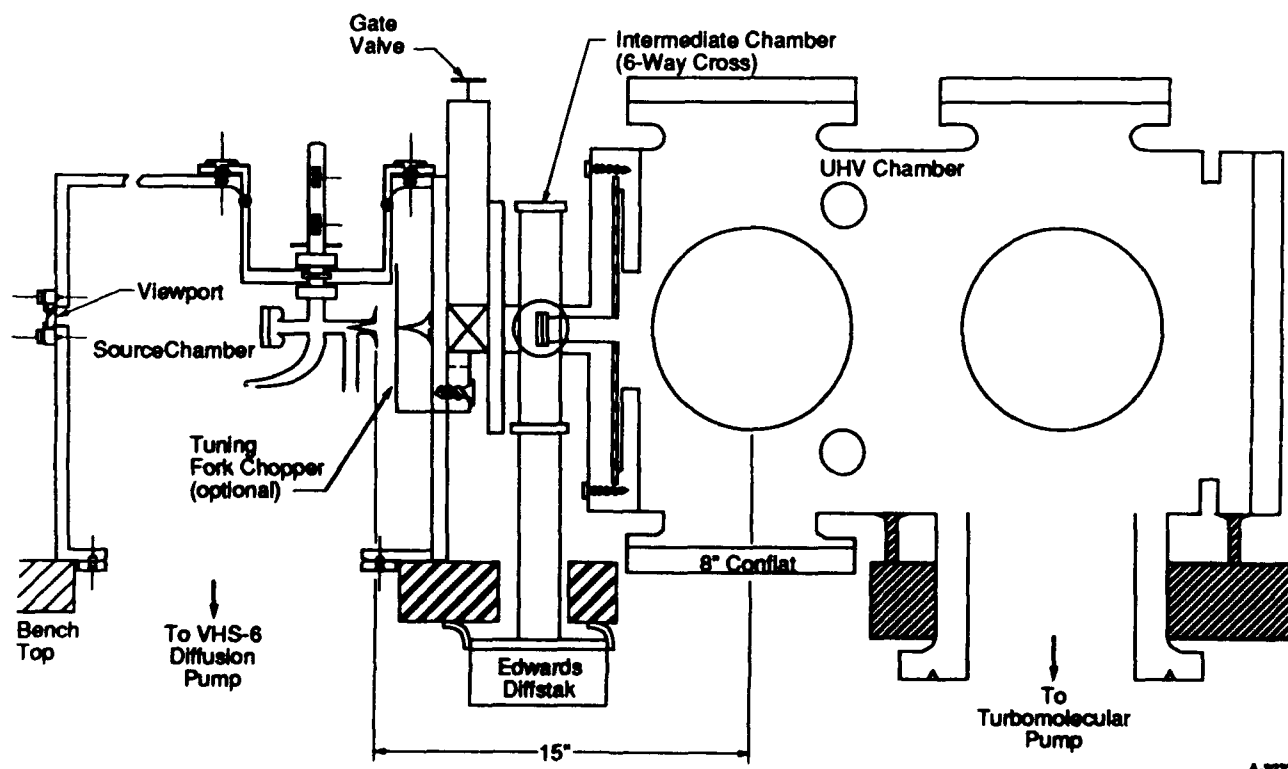


Fig. 2. Machine drawing showing assembly for all three chambers

## 2.1 Metastable Production

Metastables are formed in a discharge-flow tube source. Techniques for forming the different metastables to be used in this study (He, Ar, O<sub>2</sub>, N<sub>2</sub>) are well established.<sup>9,17,18</sup> The rare-gas metastables are generated in low power, hollow cathode discharges, and the molecular metastables such as N<sub>2</sub>(A<sup>3</sup>Σ<sub>u</sub><sup>+</sup>) are formed by energy transfer from Ar<sup>\*</sup>. To verify metastable production in the flow tube, the metastables can be detected rather sensitively using a tracer species which emits brightly as a result of energy transfer reactions with the metastables. Molecular nitrogen makes an excellent tracer for both of the rare-gas metastables, giving rise to the nitrogen second-positive bands when excited by Ar<sup>\*</sup> (<sup>3</sup>P<sub>2,0</sub>)<sup>19,20</sup> and the first-negative bands when ionized and excited by metastable helium.<sup>21</sup> Tracers are added only when assessing metastable concentrations and not during surface quenching experiments.

In order to minimize the distance from the flow reactor source to the target, the flow reactor is located inside the first vacuum chamber as shown in Figure 3. Gas flows pass through a DC discharge, located immediately before the entrance to the chamber, through a vacuum feedthrough (basically a bored-out O-ring connector) and into the flow reactor, shown in Figure 4. The main flow is exhausted through another vacuum feedthrough into a 27 cfm mechanical pump. Metastables and bath gas near the flow tube axis expand through the orifice, forming a supersonic molecular beam. A third vacuum feedthrough permits addition of a titrant species and windows permit observations of tracer fluorescence. The Wood's horn and right angle bend between the discharge and the main flow tube prevent UV



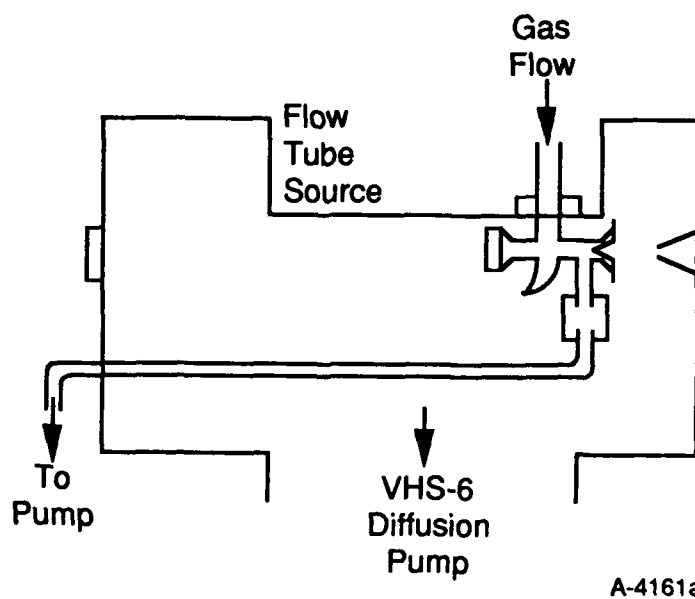


Fig. 3. Schematic of source chamber with flow reactor

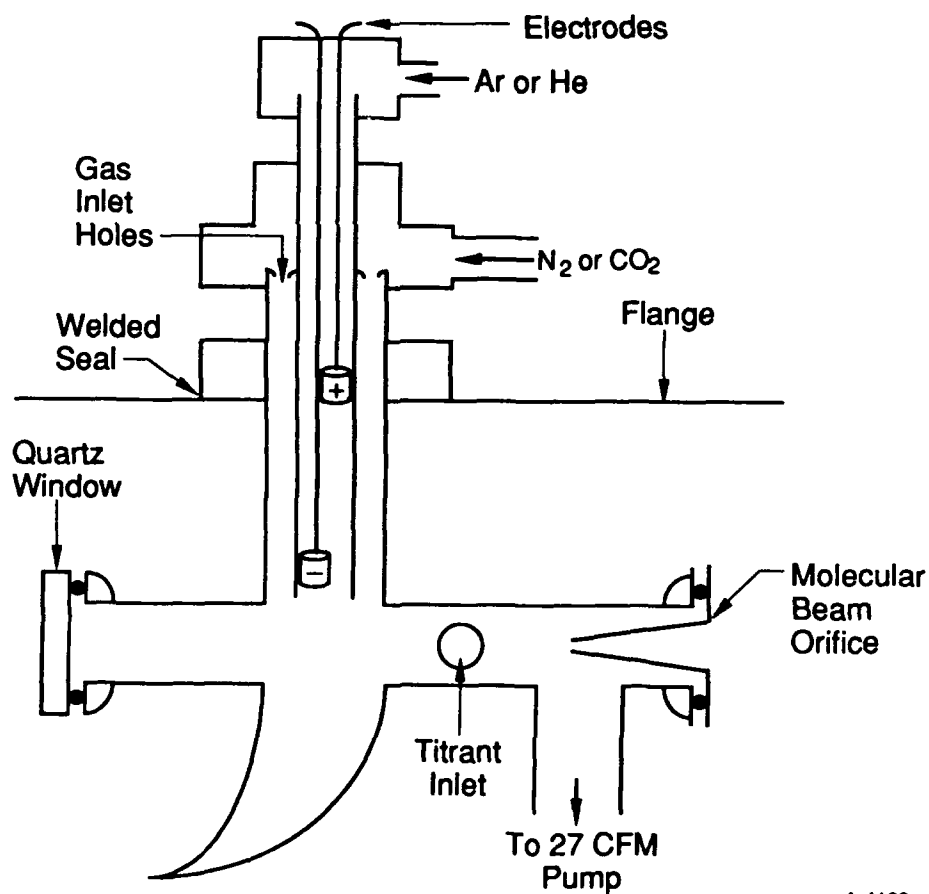


Fig. 4. Design drawing of the discharge flow tube source showing gas inlet ports and vacuum-to-air seals

radiation from the discharge from propagating to the target. The nominal diameter of the flow tube is  $\sim 0.5$  in.

Typical operating conditions are at pressures of 1 to 10 torr and linear flow velocities of  $(5 \text{ to } 7) \times 10^3 \text{ cm s}^{-1}$ . Thus the metastable residence time between the discharge and the molecular beam sampling aperture str controllable and the 1 to 3 ms range is easily attained. By comparison, the e-folding lifetime of  $\text{He}^*$  against diffusion to and quenching on the wall of the reactor is about 1 ms at 3 torr. Thus some loss of metastables will occur by surface quenching in the flow tube; however, we attain sufficiently short residence time that this loss is not too severe. Increasing the flow tube diameter would decrease the loss rate but would also decrease the linear flow velocity by the same factor, so no net gain would be achieved. However, increasing the pressure also retards wall quenching (by reducing the diffusion rate), and in addition drives a larger beam intensity as discussed below. We adjusted the operating conditions of the discharge-flow reactor to optimize metastable production in the tube and beam intensity on target. As we have designed the apparatus, the flow reactor source can be optimized independently from operation of the rest of the apparatus.

The gas beam, containing metastables at a mole fraction of the order  $10^{-6}$ , is formed, skimmed, and delivered to the target using standard supersonic molecular beam techniques. Design considerations for the vacuum system proceed as follows. The discharge-flow reactor in which the metastables are produced operates at room temperature and a nominal pressure of  $\sim 3$  torr. For these conditions in He, the mean free path is  $\sim 4.7 \times 10^{-3} \text{ cm}$ . As a "rule of thumb" guideline for supersonic expansion through a pinhole, the ratio of the mean free path to the orifice diameter (the "Knudsen number") should be of order  $10^{-1}$  or less. Thus, for orifice diameters of 0.1 to 1 mm we have the condition of choked flow through the

orifice of the flow reactor; we can then follow the treatments outlined by Fenn,<sup>22</sup> Shapiro,<sup>23</sup> and Simons<sup>24</sup> (G.A. Simons is a member of the PSI staff and has provided valuable consultation on this problem).

In the case of choked flow through a nozzle, the Mach number  $M$  is unity (Mach 1) at the throat, and the gas conditions are given by

$$\frac{T^*}{T_0} = \frac{2}{\gamma+1}$$

$$\frac{P^*}{P_0} = \left( \frac{2}{\gamma+1} \right)^{\gamma/\gamma-1}$$

$$\frac{N^*}{N_0} = \left( \frac{2}{\gamma+1} \right)^{1/\gamma-1}$$

where  $T$  is temperature,  $P$  is pressure,  $N$  is number density,  $\gamma$  is the ratio of heat capacities at constant pressure and constant volume ( $\gamma = 5/3$  for He and Ar), and the subscript 0 denotes the condition in the flow reactor (the "stagnation" condition). For  $T_0 = 300$  K,  $N_0 = 1 \times 10^{17} \text{ cm}^{-3}$ , we compute  $T^* = 225$  K,  $N^* = 6.5 \times 10^{16} \text{ cm}^{-3}$ . The velocity of the beam at  $M=1$  is the sonic velocity

$$v^* = \left( \frac{\gamma k T^*}{m} \right)^{1/2}$$

and is  $8.85 \times 10^4 \text{ cm s}^{-1}$  for He. If the expanding beam is not confined to a nozzle, there is a significant divergence at the exit of the orifice, as approximated by  $\theta_\infty$ , the Prandtl-Meyer turning angle. For  $M=1$ ,  $\gamma = 5/3$ , this angle is slightly more than 1.5 rad. This provides a condition of minimum achievable beam flux, which is employed throughout the following calculations. However, a fairly simple conical nozzle having an expansion area ratio of 10 to 100 will collimate the beam significantly: the exit Mach number would be increased to  $\sim 5$

to 7, giving a divergence angle of  $\sim 0.5$  rad, and increasing the number density on the beam centerline by a factor of four or five over the values estimated below. The actual beam flux for this condition is extremely difficult to quantify without a rigorous fluid dynamic computation.

For  $M=1$ , the beam intensity on target,  $I_T$  in molecules  $s^{-1}$ , is given by

$$I_T = N_T v^* A_T$$

where  $A_T$  is the exposed target area and  $N_T$  is the centerline number density.

$$N_T = N^* \frac{A_0}{\pi x_T^2}$$

where  $A_0$  is the area of the source orifice and  $x_T$  is the distance from the source orifice to the target. Combining these equations gives

$$I_T = \frac{N^* v^*}{\pi} A_0 \frac{A_T}{x_T^2}$$

If we set the orifice diameters for all intermediate chambers to accept the same steradiancy  $A_T/x_T^2$  as that of the target, then the beam intensity passing through each orifice is  $\sim I_T$ .

The pumping speed  $S$  required for each chamber may then be determined from the relationship

$$SP = \frac{I_T}{3.24 \times 10^{16}}$$

where  $P$  is the desired chamber pressure in torr.

During the expansion, collisions occur for an axial distance of approximately 10 nozzle diameters. The flow is then said to have reached terminal Mach number,  $M_T$ , where

$M_T = U_s/V^*$  and  $U_s$  is the flow velocity. The gas continues to expand until the pressure becomes equal to the ambient pressure,  $P_2$ , where it is reflected as a compression wave.

The merger of successive pressure waves culminates in a nearly discontinuous pressure jump or "shock" wave that forms what is often called a "shock barrel." The point at which this occurs can be calculated using

$$L_M/D = 0.667(P_0/P_2)^{1/2}$$

where  $D$  is the diameter of the nozzle and  $L_M$  is the distance to the shock wave plane. For a 1-mm nozzle and a background pressure  $P_2 = 10^{-4}$  torr,  $L_M$  equals 5 cm. For best beam quality, skimming of the beam should occur after collisions are over but before the shock wave. This region is often referred to as the "zone of silence."

The major criterion of the system is to maximize beam intensity on the target surface. The beam intensity on axis can be found in terms of Mach number:

$$I_0 = A_s n_s V_s (\pi \ell^2)^{-1} \left( \frac{1}{2} \gamma M_s^2 + \frac{3}{2} \right)$$

where  $A_s$  is the skimmer entrance area,  $n_s$  is the number density of molecules at the skimmer entrance, and  $\ell$  is the distance downstream of the skimmer entrance. The intensity on an area normal to the axis at a distance  $r$  from the axis is

$$I_r = A_s n_s V_s \frac{1}{\ell^2} \left[ \frac{1}{2} \gamma M_s^2 + \frac{3}{2} \right] \exp \left[ - \frac{1}{2} \gamma M_s^2 r^2 / \ell^2 \right]$$

The radial loss of intensity is then equal to  $I_r/I_0$  or  $\exp \left[ - \frac{1}{2} \gamma M_s^2 r^2 / \ell^2 \right]$ . For helium, in our system,  $M = 4.4$ ,  $r = 0.25$  cm, and  $\ell = 38$  cm. Therefore,  $I_r/I_0 = 0.999$ , or 99.9 percent of the intensity reaches the target.

Ashkenas and Sherman<sup>25</sup> give a different method for determining the radial loss of intensity

$$\frac{\rho(R,\theta)}{\rho(R,0)} = \cos^2 \left[ \frac{\pi\theta}{2\phi} \right]$$

where  $R$  is the length of a radius vector between a point in the jet and the exit of the nozzle,  $\theta$  is the angle between the radius vector and the jet axis, and  $\phi$  is a constant depending on  $\gamma$  ( $\phi = 1.365$  for  $\gamma = 5/3$ ). For our conditions, one calculates a ratio of 0.9999. The two methods are therefore in agreement and we can expect 99.9 percent of the on-axis intensity to reach our target surface.

Calculations of beam intensity as a function of source-to-target distance,  $x_T$ , and source orifice,  $A_O$ , for a free-jet expansion are plotted in Figure 5. Our goal, based on detectivity considerations, is to achieve a flux of  $\sim 10^9$  molecules/s of metastables on target. The mole fraction of metastables in the discharge-flow reactor is typically  $10^{-6}$  to  $10^{-7}$ . Therefore a total gas flux of  $10^{15}$  molecules/s is required to reach our goal. For our source-to-target distance of 38 cm, Figure 5 shows that a source aperture between 0.5 and 1.0 mm is needed.

These calculations have been done for the free-jet (Mach 1) condition; however, the effect of the conical nozzle on the beam sampling orifice is to constrain the divergence angle of the beam and enhance the Mach number significantly, as described above. The actual value is hard to predict without detailed fluid dynamic simulations, but we expect the nozzle to increase the center-line beam intensity by a factor of three to five. Parameters for best metastable production such as pressure and aperture size can be varied but are constrained to some extent by pumping speed considerations. However, based on our calculations, we expect to produce a flux of  $10^8$  to  $10^9$  molecules/s of metastables on the target surface.

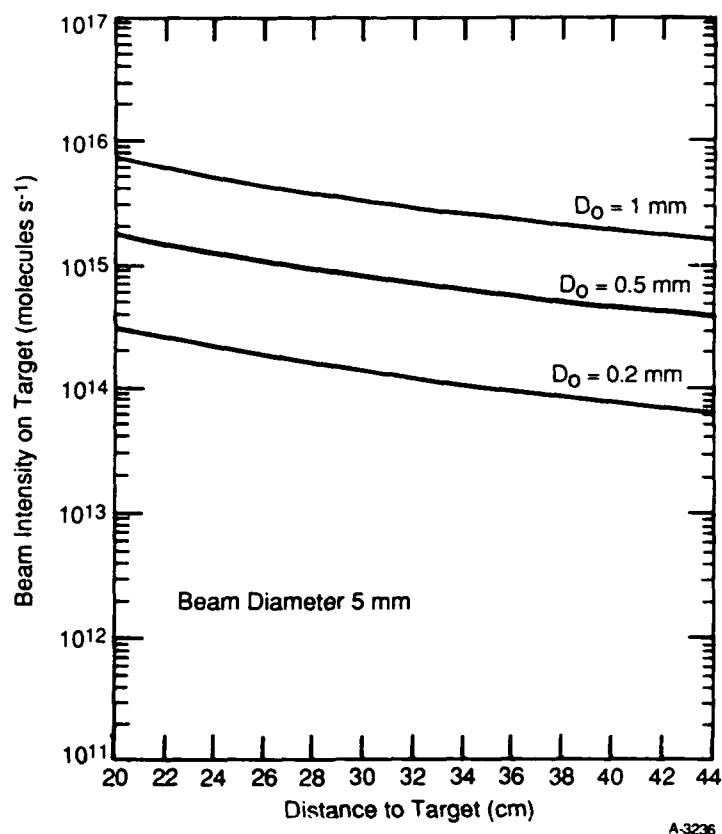


Fig. 5. Beam intensity on target as a function of source-to-target distance and source aperture,  $D_0$ , for a beam diameter on target of 5 mm

## 2.2 Vacuum Chamber Design

The apparatus, shown schematically in Figures 6 and 7, is comprised of three vacuum chambers: the source chamber, the intermediate chamber, and the UHV chamber. The source chamber has been made rectangular to accommodate placing the flow tube inside the chamber. The flow tube is on an adjustable feedthrough to allow alignment under vacuum. A window is placed on the end wall of the source chamber for alignment of the source, skimmer, downstream aperture, and the target. A He-Ne laser is used for alignment. The skimmer position is adjustable from inside the chamber. The skimmer was purchased from Beam Dynamics, who have developed skimmers expressly for supersonic expansion beams.

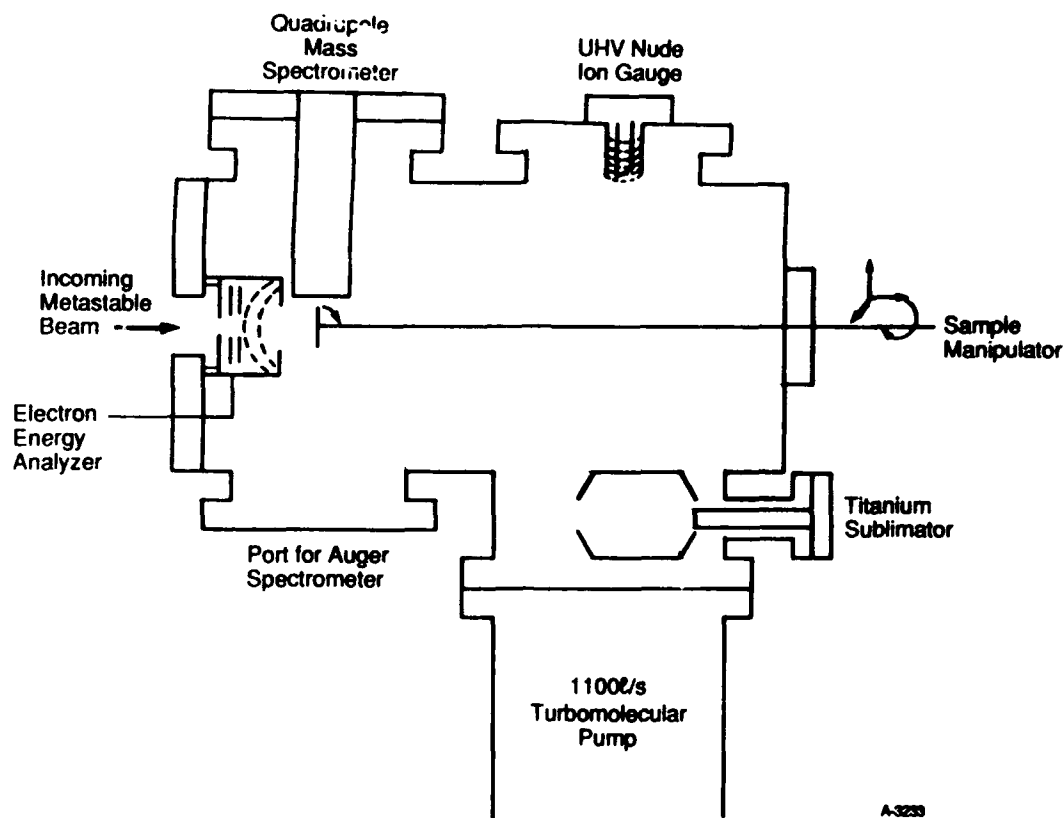


Fig. 6. Side viewing schematic drawing of the UHV chamber showing location of diagnostics.

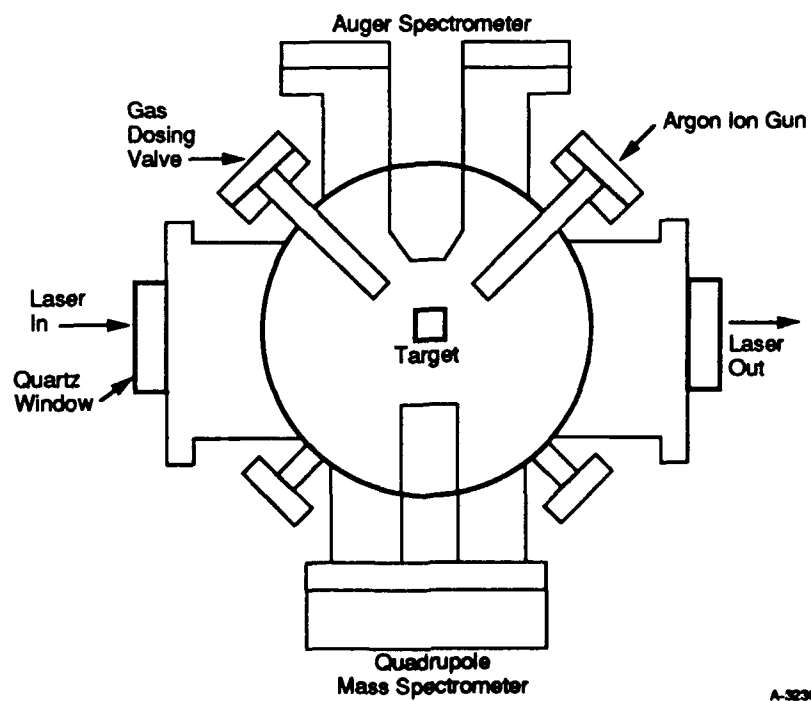


Fig. 7. Schematic drawing of the UHV chamber viewed along beam axis showing location of drag.



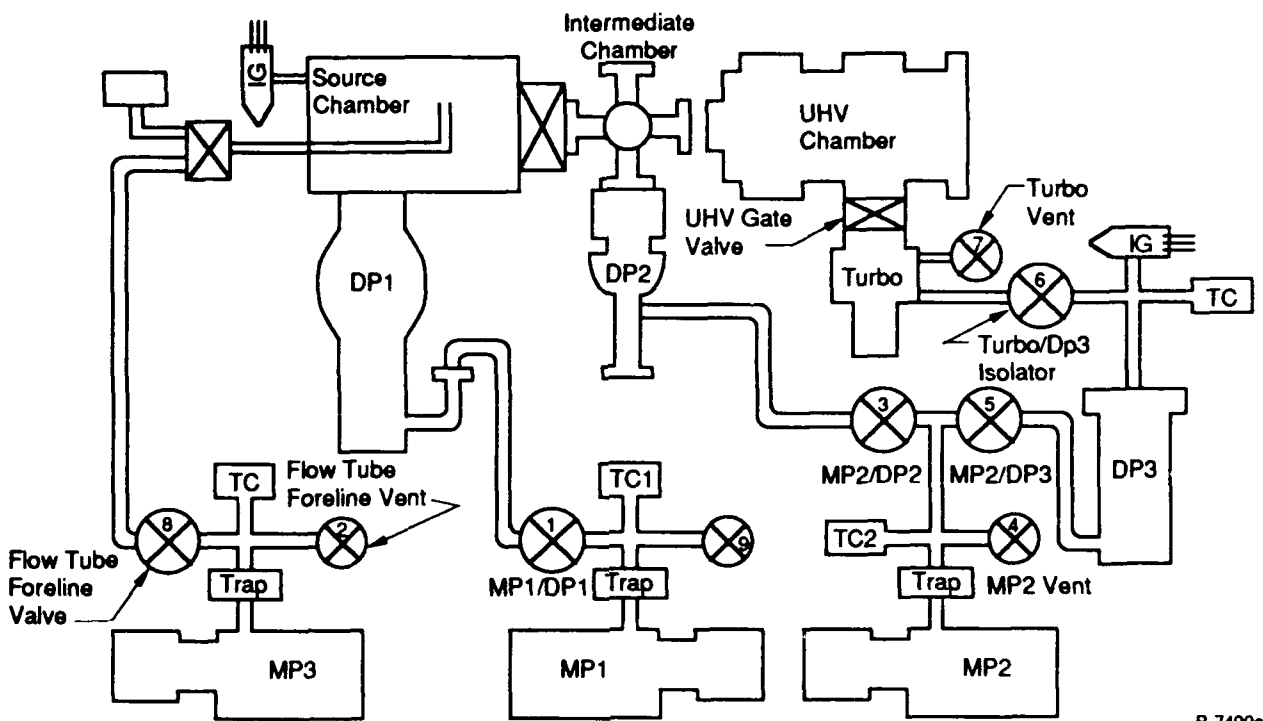
This insures a quality knife-edge that will not perturb the metastable beam. One side panel of the source chamber is made of plexiglass so visual monitoring is possible at all times. Both plexiglass and O-rings are usable materials for this chamber since an ultimate vacuum of  $10^{-6}$  torr is all that is needed.

A gate valve is located between the source and intermediate chambers. This allows for venting the source chamber while maintaining high vacuum conditions in the other chambers. The gate valve is only 1 in. thick to help minimize the source-to-target distance. It has a 2-in.-diameter opening which is the same as the tube diameter of the second chamber. Therefore, it will not interfere with metastable propagation to the surface. The main function of the intermediate chamber is to increase pumping capabilities. Located in the chamber is an aperture that helps define the beam size. The aperture itself is a miniconflat flange with a hole drilled through it. Around the hole the metal is milled down so the thickness of the plate is less than the aperture diameter. Therefore, no channeling effect on the beam will occur. The miniconflat is easily changed and makes a good UHV seal.

The UHV chamber is a 21-in.-long, 10-in.-diameter cylinder, shown in Figure 6. This design was chosen as the best way to accommodate the various diagnostics that must coexist in the chamber. Flange size and placement have been carefully designed to maximize access to the target surface. The flange that attaches the UHV chamber to the intermediate chamber has an outer diameter the same as the inner diameter of the chamber cylinder. Therefore the flange adds nothing to the source-to-target distance. A reducing flange is used to attach the two chambers. Mounted on this flange are an aperture, to separate the two chambers, and the electron energy analyzer. This scheme allows one to work on the energy

analyzer on the bench top, then insert it into the chamber. Moving in from this end of the UHV chamber, next there are four 8-in. conflat flanges equidistantly spaced around the cylinder. These four ports all offer access to the sample and accommodate the quadrupole mass spectrometer, the Auger electron spectrometer, and optical diagnostics. Located at 45 deg to each of these ports are four 2-3/4-in. conflat flanges. These flanges are used for surface cleaning and gas dosing. The sample can be translated back to these ports and forward to the diagnostics. A second set of three 8-in. and one 10-in. conflats is located several inches from the first set. These ports do not provide access to the target surface but are used for the turbomolecular pump, electrical feedthroughs, vacuum diagnostics, and a titanium sublimation pump. The end flange has an inner diameter matched to the inner diameter of the cylinder. The sample manipulator is mounted on this end flange.

Ultrahigh vacuum conditions place certain constraints on the system. The chamber is constructed from high quality stainless steel, and the interior is electropolished to reduce the interior surface area and the outgassing rate. All flanges have copper gasket seals. To reach our typical ultimate vacuum of  $10^{-10}$  to  $10^{-11}$  torr, the chamber must be baked to  $\sim 150^{\circ}\text{C}$  under vacuum following any exposure of chamber surfaces to room air. We have developed a set of strict operating procedures for maintaining UHV conditions and have interfaced the vacuum system to a fail-safe interlock control network designed to maintain chamber cleanliness in the event of a power failure. Schematics of the vacuum system and interlock logic are shown in Figures 8 and 9.

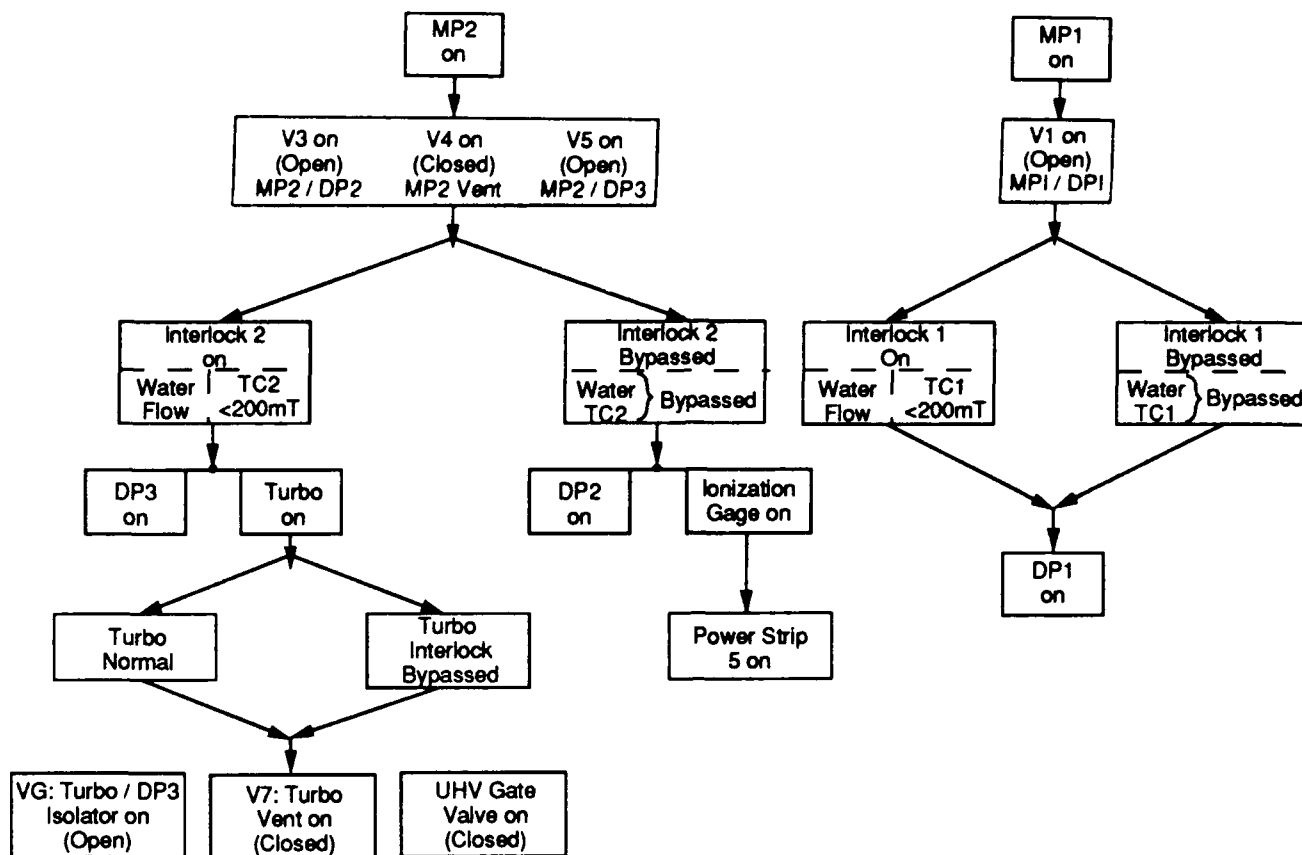


B-7499a

Fig. 8. Diagram of vacuum system

### 2.3 Pumping Requirements

In the source chamber, the pressure is a function of the exit aperture size,  $D_o$ , from the flow tube source. The pressure in the chamber, with the metastable beam on, must remain below  $10^{-3}$  torr to prevent collisional scattering of the beam by background gas in the chamber. A diffusion pump with an 8-in. throat and a pumping speed of 3000  $\ell/s$  was chosen to evacuate this chamber. A plot of the pressure in the source chamber as a function of flow tube aperture,  $D_o$ , calculated using the maximum pump speed of the chosen diffusion pump, is shown in Figure 10. Using an inlet pressure limit of  $5 \times 10^{-4}$  torr, a maximum flow tube aperture of 1 mm is established. Thus the diffusion pump is able to operate at its maximum pumping speed for the range of aperture diameters we wish to use. Under these conditions there is some oil contamination in the source chamber from the diffusion pump;



B-4870a

Fig. 9. Logic diagram for vacuum system control and safety interlock circuitry

however, this does not affect the performance of the source. The source chamber is well isolated from the UHV chamber by an intermediate chamber so no oil contamination of the UHV chamber occurs. In actual operation, source chamber pressures of  $(1-4) \times 10^{-5}$  torr are achieved for flow tube pressures of 1 to 3 torr and a 1-mm aperture.

The middle chamber serves as a pressure buffer between the high pressure of the source and the low pressure desired in the UHV chamber. There are two contributions to the pressure in this chamber: the directed flow of the beam and the effusive flow from the background pressure in the source chamber. The Edwards Diffstak Series 63 diffusion pump with a pumping speed of 173  $\ell/s$  was chosen for this chamber. It has a high pumping speed for its small size and an extremely low backstreaming rate,  $< 10^{-10} \text{ g cm}^{-2} \text{ min}^{-1}$ , which is

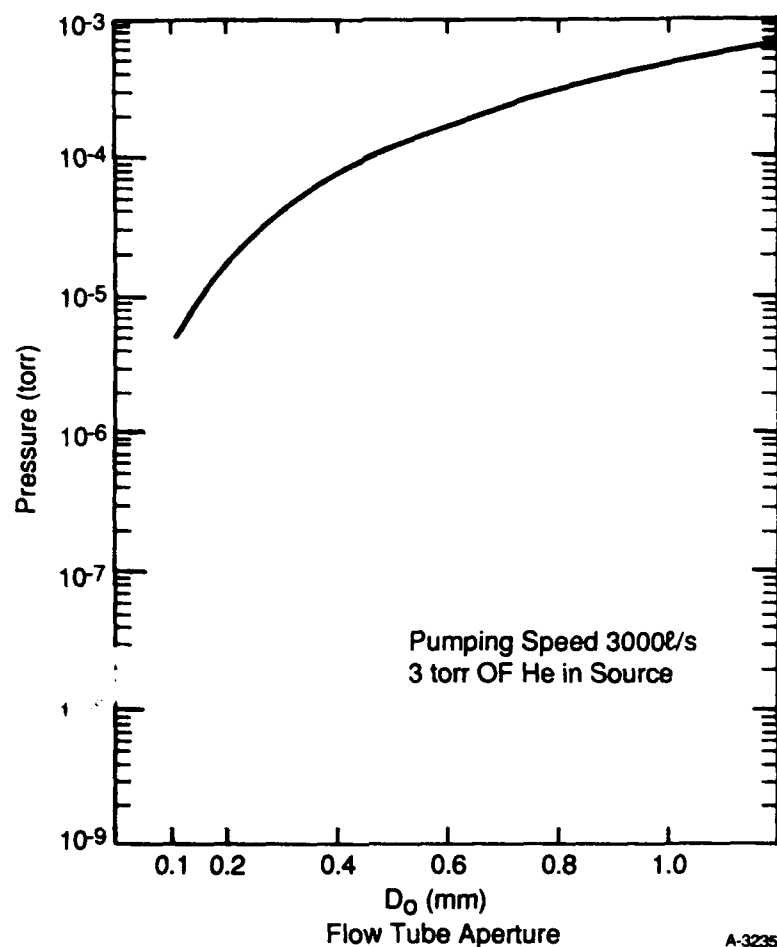


Fig. 10. Pressure in source chamber as a function of flow tube aperture,  $D_0$ , for an 8-in. throat diffusion pump and 3 torr of He in the source

comparable to that obtained with cryogenically trapped 6-in. diffusion pumps. This will prevent any oil contamination in the UHV chamber without the requirements for liquid  $N_2$  trapping. Shown in Figure 11 is a plot of pressure in the middle chamber versus distance from source to target for the chosen pump. Note that except for the smallest flow tube aperture the directed flux dominates the effusive flux. Our typical distance to target is around 38 cm. Therefore, with the chosen pump, pressures below  $10^{-6}$  torr can be

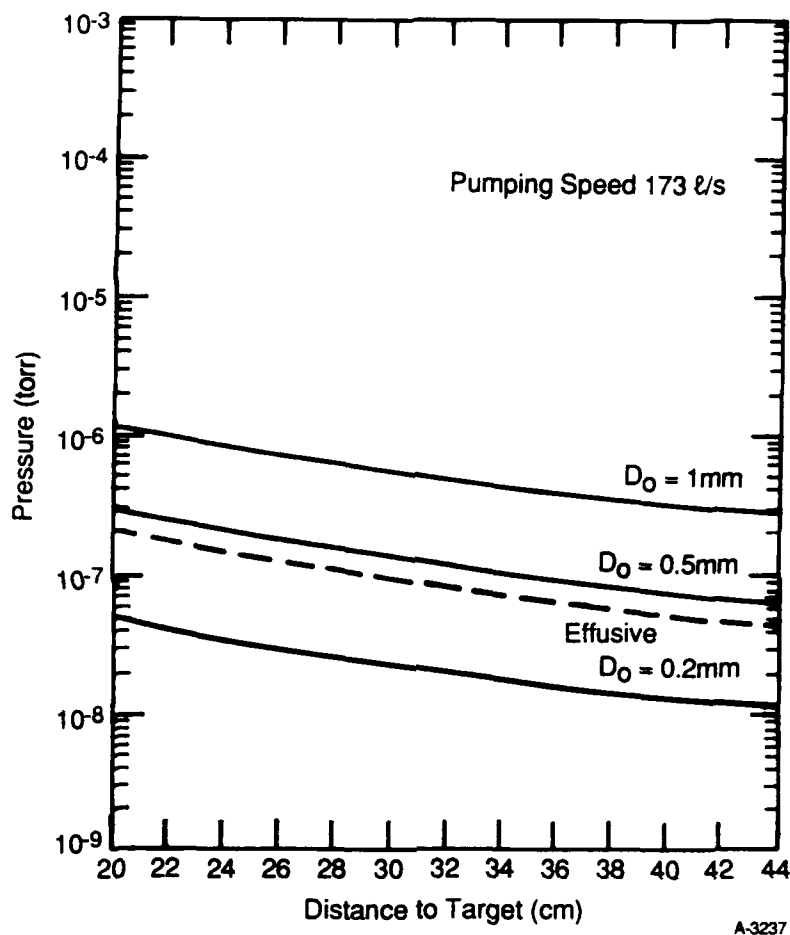


Fig. 11. Pressure in the intermediate chamber as a function of source-to-target distance and source aperture,  $D_0$ , for the Edwards Series 63 diffusion pump.

maintained for flow tube apertures up to 10 mm in size. For typical operating conditions, we observe pressures in the intermediate chamber of a few times  $10^{-7}$  torr with the beam on.

Pressure in the UHV chamber is dominated by the directed flux of the metastable beam and therefore is a function of flow tube aperture, distance to target, and pumping speed. Figure 12 shows plots for these parameters. A maximum operating pressure of  $1 \times 10^{-7}$  torr for the UHV chamber has been established by the various diagnostics that will operate in this chamber. Based on the plots, a turbomolecular pump with a pumping speed

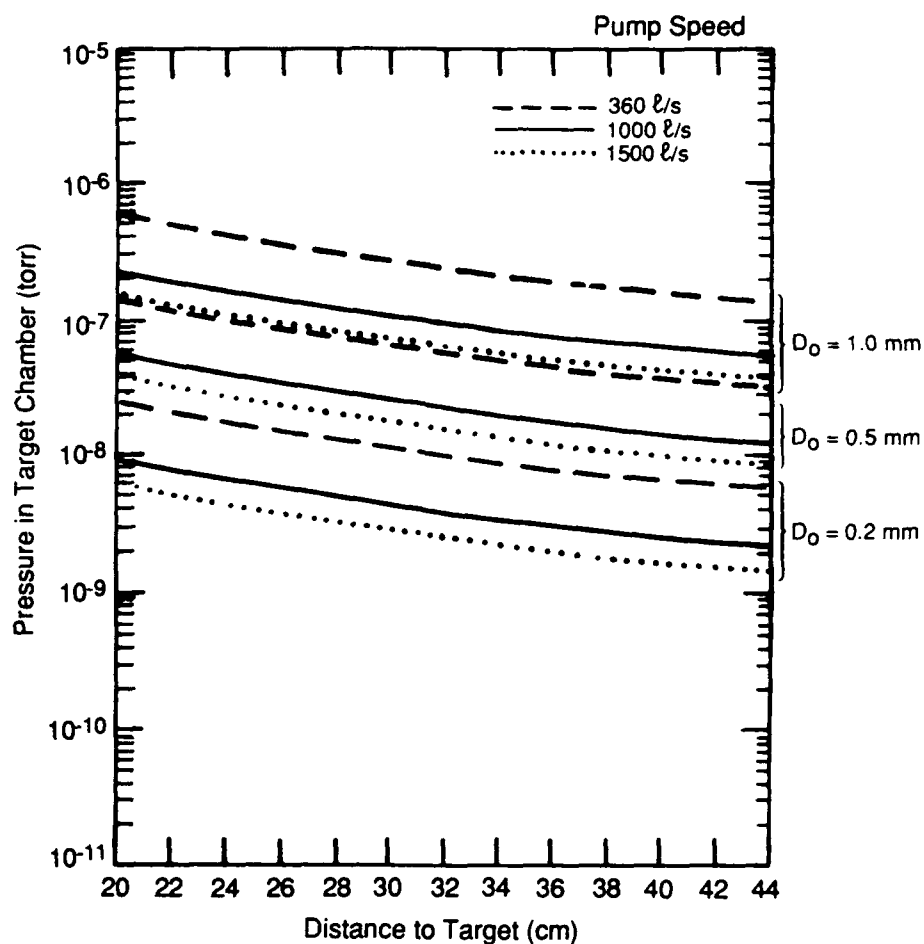


Fig. 12. Pressure in the UHV chamber as a function of source-to-target distance, source aperture,  $D_0$ , and pump speed

of 1400  $\ell/s$  (for helium) was chosen. Differences in the pumping speed for different gases in a turbomolecular pump are caused by differences in conductance (for gases of different molecular weights) up to the inlet blade row and by the transmission probability of the early blade rows.<sup>26,27</sup> Conductance is inversely proportional to the square root of the molecular weight while the transmission probability is directly proportional to the square root of the molecular weight. These two factors tend to counter one another so that the pumping speed of all gases except hydrogen is about the same. A result of the nearly

uniform pumping speed for all gases is that the molecular composition of the gas in the vacuum chamber is not drastically altered.

Use of a diffusion pump was considered, but for the ultimate pressure needed elaborate liquid nitrogen cooled baffling of the pump would have been required. Even with a carefully trapped diffusion pump system, the potential for accidental oil contamination of the UHV chamber could not have been totally eliminated. Since such contamination could lead to weeks of down-time while the chamber is being cleaned out, we concluded that a turbomolecular pump offers a more failsafe means of obtaining clean UHV conditions. To improve the ultimate vacuum of the turbomolecular pump, it is backed by a small diffusion pump and a mechanical pump.

A titanium sublimator is used to trap any traces of condensible vapors outgassing within the chamber, thus lowering the ultimate pressure somewhat. Ultimate vacuum of  $10^{-11}$  torr is typical of such systems; we typically observe pressures of  $10^{-11}$  to  $10^{-10}$  torr with the beam off and  $10^{-9}$  to  $10^{-8}$  torr with the beam on.

## 2.4 Diagnostics in UHV Chamber

The following sections detail the use and detection sensitivity for each diagnostic in the UHV chamber. Mounting locations for each diagnostic were shown in Figures 6 and 7.

### 2.4.1 Sample Manipulator

The target surface is mounted on a bakable UHV manipulator. The manipulator has  $\pm 0.5$  in. travel in the x,y directions and 6 in. of travel in the z direction. To position the target in front of the various diagnostics, the manipulator can rotate the target 360 deg



(around the z axis) and tilt the target from normal to  $\pm 45$  deg. Resistive heating of the target is also supplied.

This manipulator offers the ability to position the target with respect to any diagnostic without breaking vacuum. With a less sophisticated manipulator, the sample would have to be repositioned manually and then the system pumped back down. An air-to-vacuum pump down and bake-out cycle takes approximately 5 days to complete owing to the need to thoroughly outgas the walls of the chamber. This must be followed by an elaborate, iterative sequence for cleaning the sample surface through a combination of ion bombardment and thermal desorption/annealing. Therefore, constantly having to adjust the sample in air would severely limit the number of samples and different diagnostics that could be studied.

#### 2.4.2 Electron Energy Analyzer

The electron energy analyzer was built on a design provided by our consultant, Prof. John Yates. It consists of four hemispherical grids with a microchannel plate (Chevron configuration) detector. The detector was supplied by Galileo Electro-Optics with a 6-mm hole in the center to pass the metastable beam. The sample manipulator translates the target directly in front of and flips it normal to the analyzer. It is important that the analyzer be located directly in front of the surface to maximize collection efficiency.

The energy distribution of the electrons emitted from the sample is determined as a function of the negative potential applied to the repeller grids, which is varied continuously between  $U_{\max}$  and 0. The collector current  $I(U_t)$  as a function of the retarding potential  $U_t$  is then given by

$$I(U_t) \propto \int_{eU_t}^{\infty} N(E) dE$$

where  $N(E)$  is the energy distribution of electrons emitted from the sample.<sup>28</sup> The retarding field analyzer separates those electrons with energies less than  $eU_t$  from the rest which are collected. Thus, peaks in the  $N(E)$  distribution appear as small steps on a slowly varying background curve in the  $I(U_t)$  curve. The energy distribution  $N(E)$  can be obtained by differentiation:

$$\frac{dI(U_t)}{dU_t} \propto N(E)$$

This differentiation is performed electronically by superimposing an AC voltage with a small amplitude on the retarding voltage. The differential signal is recovered using a lock-in amplifier.

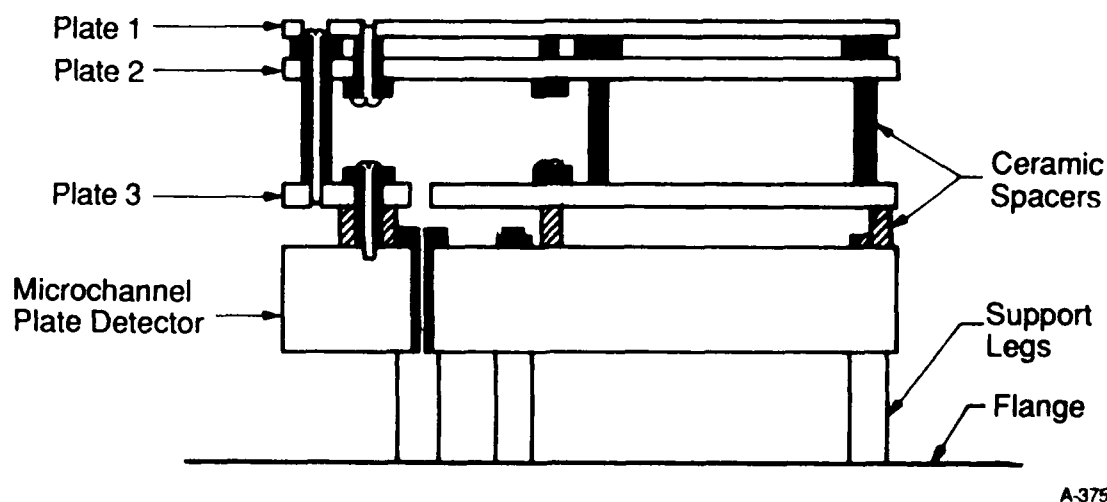
Signal sensitivity is limited primarily by the dark count rate of the detector which is 1 count/s. Since microchannel plate detectors can detect metastables,<sup>29</sup> any reflected metastables from the surface can also contribute to the background signal. There will be two parts to this background signal. Metastables directly hitting the detector have no energy dependence, and therefore show up as a continuous background. If a metastable hits a grid, then an electron will be ejected. This background signal will have some energy dependence which will be determined by the work function of the grid material (tungsten) and the voltage applied to the grid. In all applications to date, however, the percentage of reflected metastables observed from a surface has always been very small. However, if need be, the electron signal produced by metastables hitting the grid can be determined by placing an

additional grid directly in front of the surface, biased to pass no electrons. The metastables will still pass, strike the grid of the analyzer to produce electrons, and be detected.

The analyzer is very compact, 2 in. diameter by 1.25 in. high, so it fits easily into the UHV chamber. The analyzer consists of three plates of high transmission tungsten grid and a microchannel plate detector (see Figure 13). The plates are assembled using ceramic spacers made of a machineable ceramic that is UHV compatible.

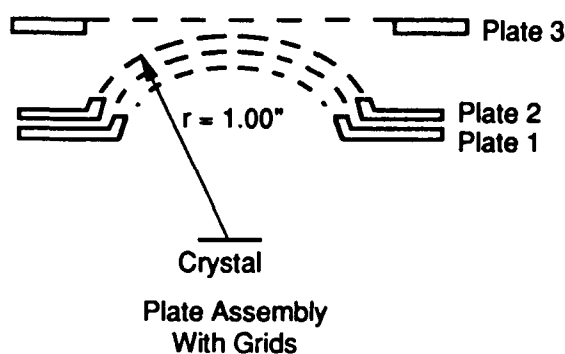
The plates are made of stainless steel to which the tungsten mesh is spot welded. The first two plates have an angled inner edge to which the grids are attached (see Figure 14). The plate is placed over a lap made of brass and then the grid is formed on the lap. Each wire of the mesh is then spot welded to the plate to prevent any charge potentials forming on stray wire tips. The middle plate actually has two grids attached to it separated by the plate thickness. The purpose of this double grid is explained below.

The microchannel plate detector is in the Chevron configuration, in which two microchannel plates are placed in tandem with a small gap in between. This increases the

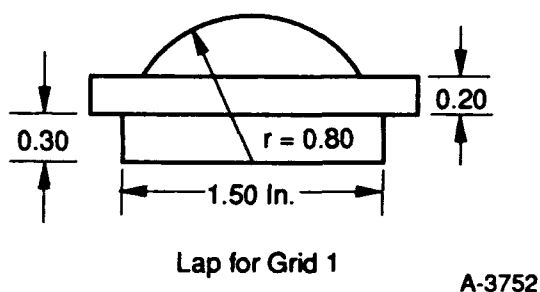


A-3751

Fig. 13. Schematic drawing of the energy analyzer assembly



(a) Single plate



(b) The lap used to form the grid mesh

Fig. 14. Side views

electron gain to over  $10^4$ . The detector is 5 cm in diameter with an active area of  $12.5 \text{ cm}^2$ . The active area is reduced slightly by a 6-mm hole placed in the center of the detector to pass the metastable beam. The detector is protected from stray electromagnetic fields by a mu-metal shield. Mu-metal foil can be purchased in rolls and is easily formed.

The energy distribution of the electrons emitted from the sample is determined as a function of the negative potential applied to the repeller grids on Plate 2. Plates 1 and 3 are grounded. The advantage of two grids on the repeller plate can be seen when one considers the local variation in the potential in the vicinity of the retarding grid. For single retarding 100 mesh 0.025 mm wire grid at potential  $V$ , placed midway between two grounded grids 6.35 mm apart, the potential difference  $\Delta V$  between the center of a grid aperture and the grid wires is such that  $\Delta V/V \approx 2$  percent.<sup>30</sup> Improvements could be achieved by increasing the grid spacing, using finer mesh or increasing the depth of the mesh with a honeycomb structure. A more practical solution, and one that is now commonly employed, is to use two retarding grids separated by a short distance.

The retarding grid acts to separate those electrons with energies less than the retarding potential from the rest which are collected. Therefore, as the retarding potential is ramped, peaks in the energy distribution appear as small steps on a slowly varying background curve. The energy distribution can be obtained by differentiation. This can be performed electronically by superimposing an AC-voltage with a small amplitude on the retarding voltage. The differential signal is then recovered using a lock-in amplifier.

For our samples the retarding voltage is ramped from 0 to 15V. No electrons of higher energy are expected, though larger initial survey scans were also performed. Scan times are on the order of 5 min. The signal can be recorded either on a chart recorder or a computer. The analyzer is run by a specially constructed ramp generator circuit described in detail in Appendix A.

#### 2.4.3 Multiphoton Ionization

A laser multiphoton ionization (MPI) diagnostic was developed to probe both the incoming metastable beam and the metastables reflected from the target. Quartz windows are mounted on both sides of the chamber to allow laser light to pass through the chamber in front of the target. A Quantel Nd:YAG-pumped tunable dye laser system was used for these studies. The pulse width of this laser is 7 ns with a 10-Hz repetition rate. The electron energy analyzer was used to detect the ions formed by reversing the polarity on the grids and microchannel plate detector. The detector has the same efficiency for both electrons and ions. A UHV BNC electrical feedthrough was used for the signal from the detector. Since signal is only generated during the 15-ns laser pulse, a gated boxcar integrator was used to

collect the signal. In this configuration, the gated signal can be averaged over many laser pulses to achieve good S/N.

Through laser wavelength selection, metastables can be ionized without any accompanying ionization of neutral molecules. To ionize the rare-gas metastables only one laser photon is needed. It is therefore possible to saturate the transition and ionize all metastables in the laser volume (collimated to 3 mm in diameter). With our detector arrangement, an ion collection efficiency of nearly 100 percent was expected.

The percent of rare-gas metastables reflected from the surface should be small. Conrad et al.<sup>31</sup> report a range of survival probabilities for He metastables from clean and adsorbate-covered single crystal surfaces of  $3 \times 10^{-3}$  to  $4 \times 10^{-6}$ . In general, adsorbate-covered surfaces had larger survival probabilities.

In principle, MPI is a very sensitive technique and a detection limit of one ion per laser pulse is easily attained.<sup>32</sup> This gives a reflected metastable detection limit of a survival probability greater than  $7 \times 10^{-5}$ . However, a serious unforeseen problem in the use of photoionization (PI) to detect metastables scattered from the sample is the apparent sensitivity of the particle detector to scattered laser light. The detection of He\* metastables requires single-photon absorption at wavelengths below 264 nm. The detection efficiency for the microchannel plate (MCP) detector at this photon energy was not originally believed to be sufficiently high to warrant the extensive use of light baffling within the UHV chamber. Actual use of the detector without baffling resulted in the observation of scattered light signals which would not permit the detection of ions produced by the PI process. Consultation with the manufacturer of the MCP detector confirmed that the quantum efficiency of the detector was indeed quite small,  $\sim 10^{-5}$  at 200 nm. We are forced to

conclude that the scattered light was sufficiently large in the original configuration to produce appreciable signals even with this low quantum efficiency.

We have taken several measures to reduce scattered light levels in the chamber in a manner consistent with maintaining UHV conditions. The original laser/detector configuration used in the UHV chamber is shown in Figure 15. It consisted of the MCP detector and beam focusing optics with little shielding of the detector from sources of scattered light. Two of the sources are immediately obvious: the entrance and exit windows and the turning prisms and focusing lens. A lesser source is secondary scatter from the

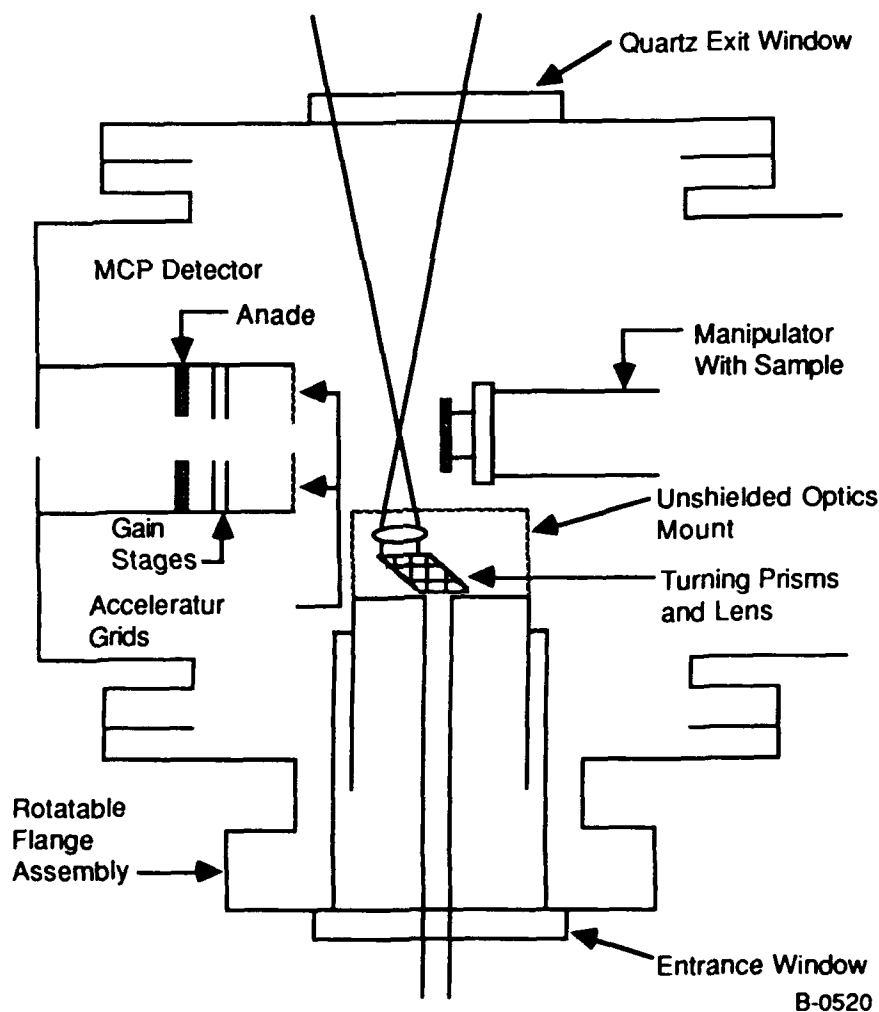
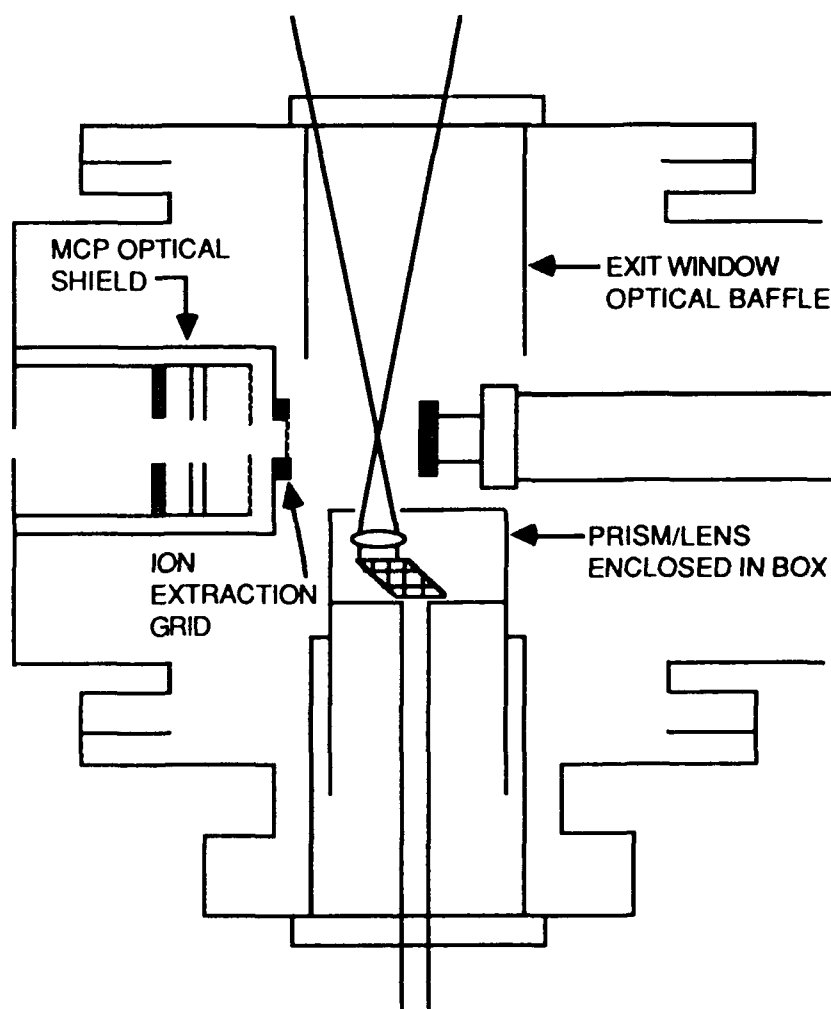


Fig. 15. Optical detection system as originally implemented

polished surfaces of the UHV chamber, i.e., scatter from a prism or window reflected from the cell walls into the detector. These polished surfaces are routinely used in UHV systems to reduce the surface area of the chamber. At UHV pressures the primary source of background gas is desorption of adsorbed gas from these surface sites.

Several baffling methods were used to reduce the level of scattered light incident on the detector. These are shown schematically in Figure 16. To reduce scatter from the exit window a long tube was included, extending from the window to a point near the entrance aperture of the detector. The tube severely limits the angle at which light can reflect from



B-0521

Fig. 16. Improved optical detection system



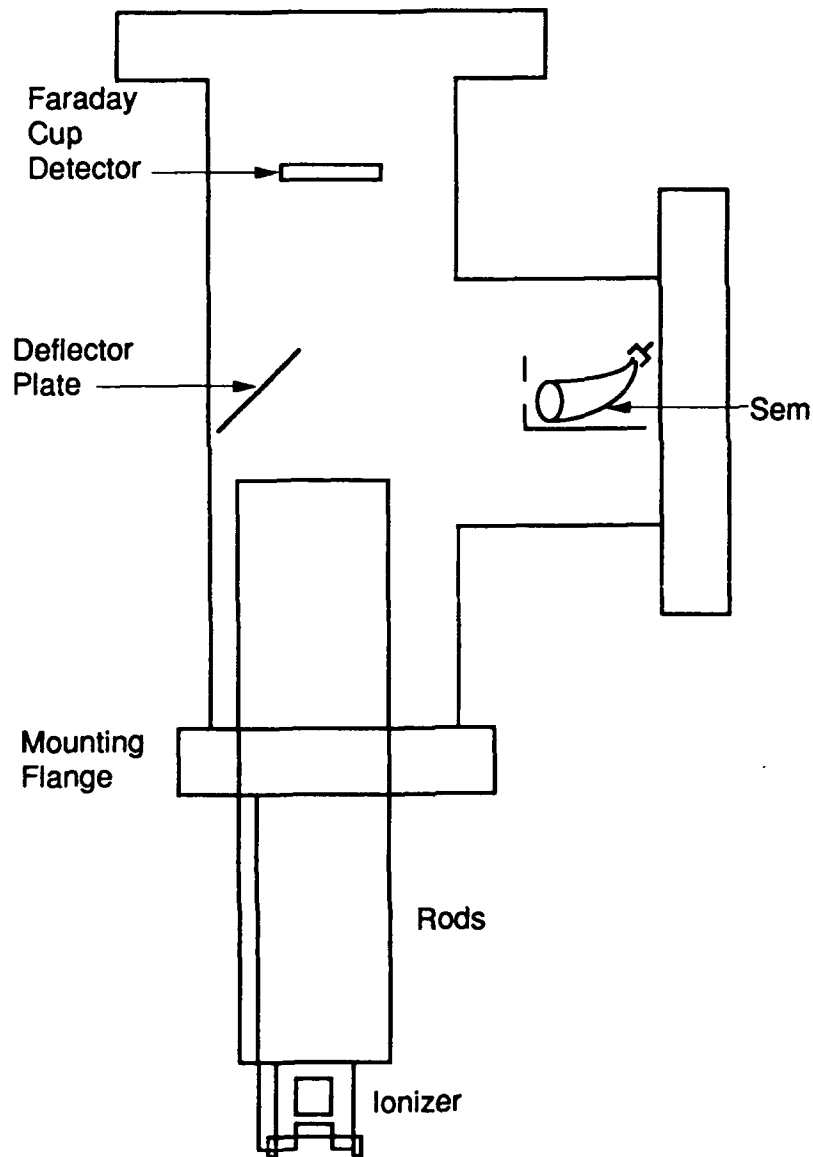
the exit window and enter the detector directly. Scattered light from the turning and focusing optics was confined to a box shielding the optics from the chamber. The dual tube configuration used to mount the optics prevents scattered light from the entrance window from reaching the detector. Finally, the detector assembly was shielded from the UHV chamber with a narrow entrance slit provided for ions produced by the laser to enter the detector. An additional ion collection grid was placed at the entrance slit to improve ion collection efficiency. The net effect of including these baffles was the reduction in scattered light levels by over a factor of 100.

These scattered light levels are still larger than the signal levels expected from the metastables. A second measure was adopted to further reduce the scattered light levels. This measure involves the coating of many of the reflective surfaces in the chamber with a spray-on graphitic coating which is an efficient absorber of UV light. The coating is called Aerodag-G (Acheson Colloids) and consists of a suspension of graphite in methyl chloroform, isopropyl alcohol, isobutane, and propane. All of these components are quite volatile and are nearly completely desorbed from the graphite by heating with a heat gun at atmospheric pressure. Additional heating under vacuum produces a UHV compatible, but higher surface area, nonreflecting coating.

Application of this coating to the inner surfaces of the chamber walls and optical baffles gave a substantial further reduction in the scattered light signal, as evidenced by successful MPI detection of seeded NO in diagnostic tests.

#### 2.4.4 Quadrupole Mass Spectrometer

The quadrupole mass spectrometer provides a variety of capabilities in the UHV chamber. These include monitoring pressure, leak rates, beam contamination levels, and desorption product levels. The Balzers QMG-311 system incorporates a 90-deg, off-axis secondary electron multiplier (SEM) with a gain of  $10^8$ . The 90-deg, off-axis geometry shown in Figure 17 reduces the stray or spurious signal due to photons, fast ions, or



A-3234

Fig. 17. Schematic drawing of quadrupole assembly

metastable species traversing the length of the quadrupole rods. The inherent count rate due to the dark current of such an SEM when coupled to an ion/pulse counting electronics system is less than 1 count/s. A stray/spurious count rate of 10 counts/s due to photons, fast ions, etc., is reasonable, but is heavily dependent on geometry, and on the specifics of each experimental setup. These arguments set a constant lower noise level at 10 counts/s. To this constant lower noise level, one must add the mass dependent count rate arising from the base pressure or imperfect vacuum. This can make the detection limit of any reaction process synonymous with the partial pressure of background gas at the relevant mass. The worst detection limit would thus correspond to the total experimental pressure. The best detection limit corresponds to the constant lower noise level of 10 counts/s.

The pressure monitoring capability of a quadrupole is the most common means of comparing instrument to instrument sensitivity and detection limits. The QMG-311 system quotes a sensitivity for argon of  $> 10^{14}$  pulses/s per mbar and a detection limit  $< 10^{-15}$  mbar. The products of these values provide a detection limit count rate on the order of 1 count/s, implying the expected constant lower noise level will be smaller than 1 count/s. Our more conservative estimate of this constant lower noise level of 10 counts/s would suggest a pressure detection limit on the order of  $10^{-14}$  mbar or  $7.6 \times 10^{-15}$  torr.

The quadrupole mass spectrometer is also utilized as a helium leak detector to assure UHV performance. Since the empty electropolished UHV chamber does not outgas much helium, we can realize the constant lower noise level detection limit of 10 counts/s, which corresponds to a pressure of  $10^{-14}$  mbar. Given the turbomolecular pump speed of 1400 l/s for helium, an approximate leak rate detection limit is  $1.1 \times 10^{-11}$  torr-l/s or  $1.4 \times 10^{-11}$  atm-cc/s, which is comparable to or better than that for commercially available

leak detectors. The largest detectable total leak rate of helium would be that producing an unsafe pressure for operation of the quadrupole. This pressure, using the integral Faraday cup detector instead of the SEM, is  $10^{-5}$  torr, corresponding to a largest measurable leak rate of  $1.4 \times 10^{-2}$  torr-ℓ/s ( $1.8 \times 10^{-2}$  atm-cc/s).

The quadrupole mass spectrometer also allows us to determine approximate molecular beam contamination levels. In the absence of a target surface, the difference between beam-on and beam-off mass spectra provides a relative measure of molecular beam species. Given the calibration sensitivities, approximate contaminant concentrations may be calculated. Given a 10-MHz SEM/pulse counting system and assuming our 10 count/s noise level limit, contaminant levels down to the 1-ppm level may be detected.

The quadrupole mass spectrometer may also be utilized to detect desorption processes. The most important question is our detection limit. We anticipate an incident metastable current of  $10^9$  metastables/s impacting the surface. If we assume 100 percent reaction efficiency, we would observe  $10^9$  molecules/s desorbing from the surface into  $2\pi$  steradians. Given the quadrupole-to-surface distance of 2.54 cm, the flux of desorbing species at the entrance of the quadrupole would be

$$\text{flux desorption at Quad} = \frac{10^9 \text{ molecules/s}}{2\pi R^2} = 2.4 \times 10^7 \text{ molecules cm}^{-2}\text{s}^{-1}.$$

The flux of background gas at the quadrupole will be on the order of  $n_B \bar{v}$  where  $n_B$  is the background gas number density and  $\bar{v}$  is the thermal velocity. The  $n_B$  corresponding to our detection limit partial pressure of  $7.6 \times 10^{-15}$  torr is  $2.43 \times 10^2$  molecules/cm<sup>3</sup>. The thermal velocity is in the range of  $4 \times 10^4$  cm/s. Thus the detection limit background flux corresponds to  $9.7 \times 10^6$  molecules cm<sup>-2</sup> s<sup>-1</sup>. Thus according to this rough calculation, the

maximum signal due to metastable induced desorption is expected to only be comparable to the background level. Note that the detectable reaction efficiency scales inversely with incident flux. A factor of five increase in incident flux, which could occur due to beam focusing in the source nozzle as described above, will result in our ability to detect desorption efficiencies of 20 percent. In addition, using the largest nozzle aperture and raising the flow tube pressure may result in significantly increased metastable flux, making the detection of desorbed neutrals more feasible. However, any hope for detection of desorbed neutrals may be relinquished if a background gas of the same mass is present.

In the present effort, we observed no mass spectral features related to beam-induced desorption, as expected. To pursue this type of measurement further, it would be necessary to employ differential pumping on the mass spectrometer, together with tuning-fork modulation of the beam, to give significant improvements in detection efficiency.

#### 2.4.5 Pressure Measurement

Measuring the pressure in the UHV chamber cannot be done with a conventional glass-envelope Bayard-Alpert gauge. The detection limit is determined by the x-ray limit of the ionizer which in this case is  $10^{-9}$  torr. For UHV applications an electron-bombardment-degas nude ionization gauge is used. This gauge is exposed directly to the vacuum. The x-ray limit of this gauge is  $2 \times 10^{-11}$  torr. The quadrupole is available to use as a residual gas analyzer to measure pressure.

#### 2.4.6 Sample Cleaning

Until very late in the program, no diagnostic (such as Auger Spectroscopy) was available to test for surface cleanliness. Under these circumstances, the best way to assure cleanliness is to use a standard technique demonstrated by others to work. Target surfaces were cleaned in vacuum using cycles of argon ion sputtering and heating as recommended by Prof. Yates. However, the resistive heating capability installed in the present program could only reach sample temperatures of  $\sim 600$  K, which is insufficient to anneal surface roughness brought about by ion bombardment. An argon ion gun is located several inches back of the quadrupole. The location of the gun is such that no damage can occur to other diagnostics. A gas dosing valve is also available for placing adsorbates on the surface.

#### 2.4.7 Additional Capabilities

With the additional support of NASA and PSI internal funds, we have significantly upgraded the diagnostic and surface treatment capabilities of the UHV chamber beyond those described above. These upgrades include the addition of an Auger electron spectrometer for surface cleanliness analysis, a high-temperature sample thermal control system for use in surface annealing (following cleaning by ion bombardment) and in high-temperature gas-surface interaction studies, and differential pumping of the mass spectrometer. These capabilities were utilized in a NASA-supported investigation of the recombination of atomic oxygen on refractory surfaces,<sup>33,34</sup> as described in Appendix B. Because the initial stage of the NASA program overlapped with the latter portion of the experimental phase of the metastable-surface interaction measurements, we originally planned to complete these UHV upgrades in time to use them in the current project. Unfortunately, the timing of the Auger

and surface heating upgrades did not proceed as planned, and these capabilities came on-line at a stage too late in the metastable program for them to be implemented.

In summary, the present capabilities of the beam-surface apparatus include surface heating and control to  $\sim 1400$  K; surface cleaning and monitoring by argon-ion bombardment and Auger electron spectroscopy; differentially pumped, modulated-beam mass spectrometry, for detection of scattered species as well as residual gas analysis and leak detection; electron/ion collection and energy analysis; and tunable laser photoionization to detect incoming and scattered species. For the measurements reported here, many of these capabilities simply could not be made available within the planned project cost. Specifically, the surface annealing and Auger analysis capabilities were not available for these measurements, seriously compromising our knowledge of the surface characteristics. In addition, the laser photoionization diagnostic, which we had expected to be far more sensitive for scattered species detection than mass spectrometry (hence our initial decision not to pursue modulated-beam mass spectrometry), was rendered essentially useless by scattered light effects as described above. Although subsequent efforts to minimize the scattered light problem eventually succeeded, this occurred after the metastable quenching measurements described in this report, and we did not use the laser diagnostic to detect metastables in the beam. Thus the only UHV-chamber diagnostics available for the measurements reported here consisted of the electron energy analyzer and the quadrupole mass spectrometer as a residual gas analyzer.

### 3. MEASUREMENT RESULTS

The experimental measurements employed two configurations of the apparatus. To test for production of metastables in the beam, we used the source and intermediate vacuum chambers together with an electron multiplier to diagnose the metastable flux. To investigate secondary electron emission from metastable-surface interactions, we connected the source and intermediate chambers to the UHV target chamber.

#### 3.1 Metastable Generation and Flux Measurements

The flow characteristics for the discharge-flow reactor were determined by measuring the pressure as a function of the flow rate for helium. Pressure in the flow tube was measured using a Baratron 0 to 10 torr capacitance manometer. The pressure in the flow tube was varied by adjusting the flow rate with a needle valve. The gas flow rate was measured with an electronic mass flow meter. For this test the molecular beam orifice was removed and the end of the tube was sealed. Therefore, all of the gas was pumped by the 27-cfm mechanical pump.

The flow velocity was determined using the mass flow equation:

$$v = \frac{f}{aN} \quad (1)$$

where:

$f$   $\equiv$  gas flow in number of molecules/s

$N$   $\equiv$  total number density in the flow tube

$a$   $\equiv$  flow tube cross-sectional area

$v$   $\equiv$  bulk gas flow velocity.



The term  $f$  is measured with the mass flow meter and  $N$  is calculated from the capacitance manometer pressure reading using Eq. (2).

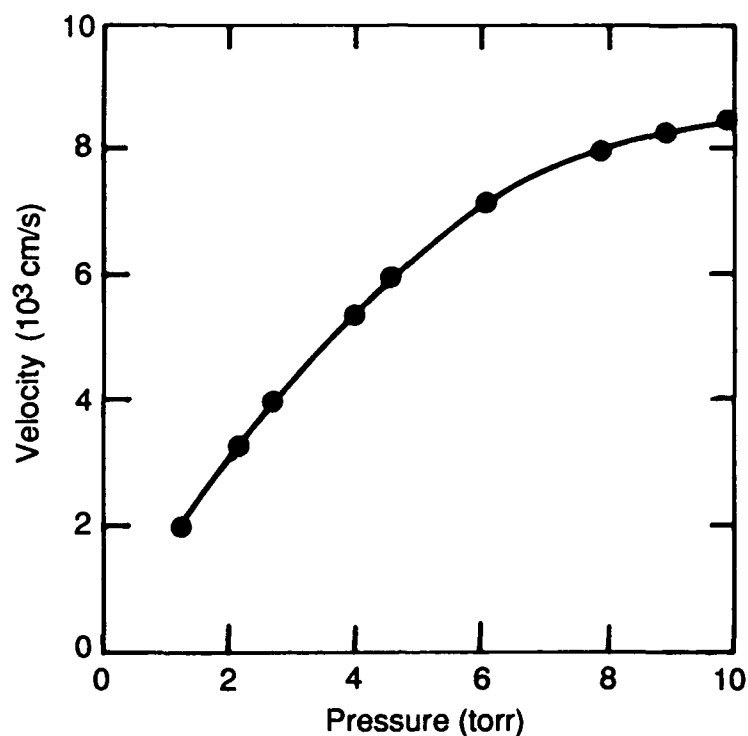
If the total pressure in the flow tube is  $P_T$  (torr) at temperature  $T(K)$ , then the number density of reactant  $i$  is given by:

$$N_i = \frac{f_i}{\sum_i f_i} \left[ \frac{P_T N_0}{RT} \right] \quad (2)$$

where  $f_i$  = flow rate of reactant  $i$ ,  $\sum_i f_i$  total flow rate of all reactants in flow tube,  $N_0$  is Avogadro's number, and  $R$  is the gas constant.

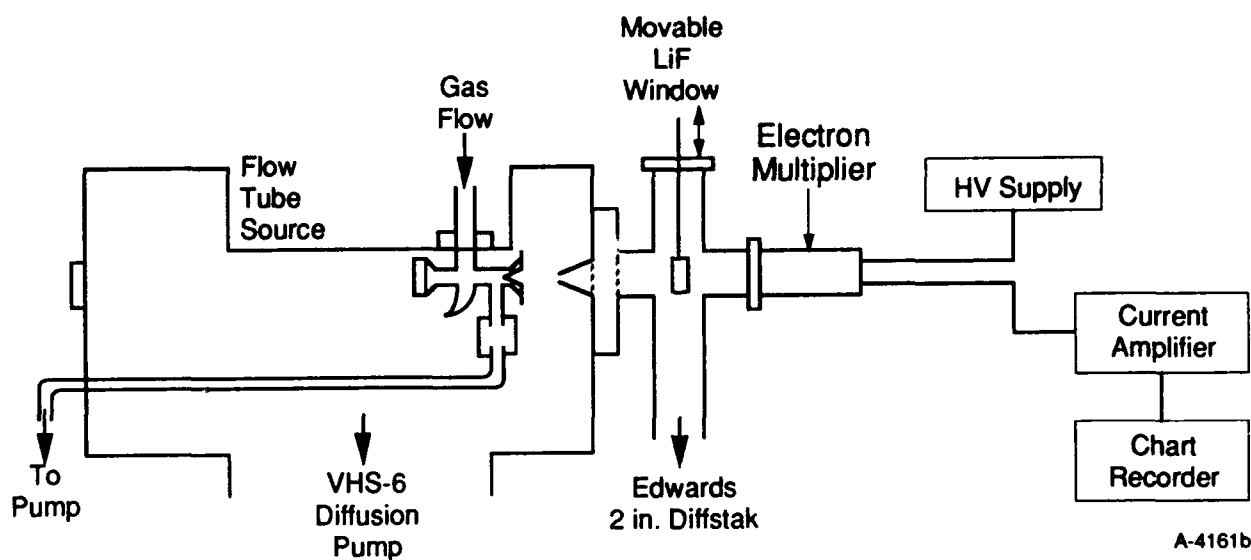
Using these equations we calculated flow velocities of 2000 to 8500 cm/s for pressures up to 10 torr. The results of our measurements are shown in Figure 18. At lower pressures the velocity increases linearly with pressure. As the pressure approaches 10 torr the velocity tends to approach a plateau. Therefore, for our system the maximum achievable flow velocity is 8500 cm/s. Typical conditions for metastable generation are around 3 torr or a flow velocity of 5000 cm/s.

The source and intermediate chambers were set up to characterize the performance of the metastable source and to determine the approximate metastable flux extracted into the molecular beam. This was done using the configuration diagrammed in Figure 19, where the UHV chamber was disconnected and a nude channel electron multiplier (Galileo Channeltron 4732) was placed in the intermediate chamber, directly in line with the molecular beam axis. Alignment was verified using a HeNe laser beam directed through the discharge tube, the beam sampling aperture, and the skimmer onto the collecting surface. A LiF window, mounted on a vertically sliding probe, was used to block the beam and isolate the



A-5779

Fig. 18. Helium flow velocity as a function of pressure in the flow tube. Measurements were made with molecular beam orifice replaced by a blank-off flange.



A-4161b

Fig. 19. Configuration for electron multiplier beam diagnostics tests

contributions of scattered VUV radiation on the electron multiplier signal. The discharge was operated on Ar, whose 106.6 nm resonance transition is transmitted by LiF. Typical discharge operating conditions were pressures of 2 to 3 torr and voltages of 200 to 300V. Electron multiplier supply voltages were typically near 1.5 kV, and were varied up to 2.5 kV. (The manufacturer's specification quotes a gain of  $1 \times 10^6$  at 2.5 kV.) Upon initiation of the discharge, a strong signal was observed from the electron multiplier. Disappearance of this signal when the beam was shuttered by the gate valve verified that the signal was due to a combination of VUV photons and energetic discharge effluents. Insertion of the LiF window into the beam reduced the signal by a factor of three, showing that most of the beam-induced signal is due to impingement of energetic species on the electron multiplier. This is most likely due to Auger quenching of  $\text{Ar}^*$  metastables, whose  $\sim 11$  eV electronic energy will overcome the work function of the electron multiplier to produce current.<sup>35</sup>

Addition of  $\text{N}_2$  to the discharge effluents in the flow reactor gave a characteristic blue flame, resulting from the energy transfer from  $\text{Ar}^*$  to  $\text{N}_2$  to excite the  $\text{N}_2(\text{C}^3\Pi_u)$  state. The appearance of this flame indicates the copious presence of  $\text{Ar}^*$  in the discharge effluent. Systematic addition of  $\text{N}_2$  reduced the electron multiplier signal, as shown in Figure 20, through quenching of  $\text{Ar}^*$  and probably also of the resonance radiation.

$\text{N}_2(\text{A}^3\Sigma_u^+)$  metastables, produced from the  $\text{Ar}^* + \text{N}_2$  interaction, may also produce signal from the electron multiplier; however, from the data of Borst<sup>35</sup> for impact of metastables on a Cu-Be-O electron multiplier, we expect the secondary electron yield for  $\text{N}_2(\text{A})$  to be a factor of  $\sim 30$  or more smaller than for  $\text{Ar}^*$ .

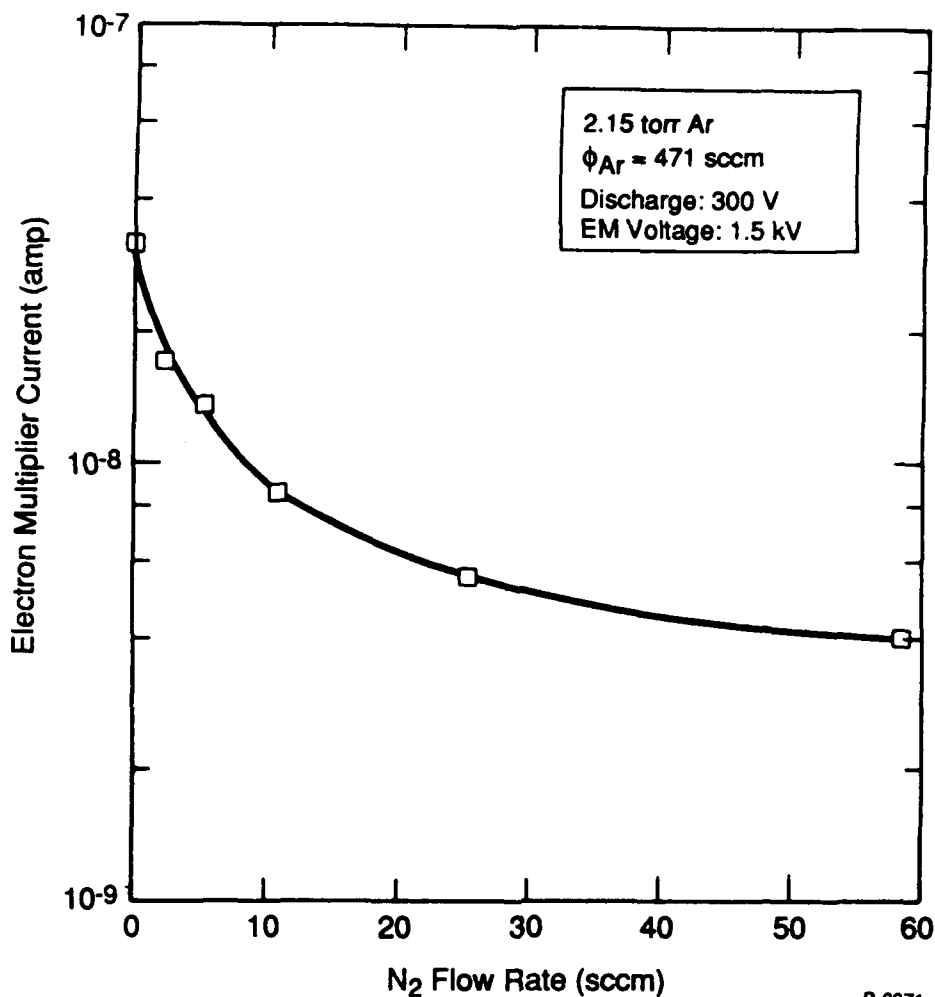


Fig. 20. Electron multiplier current versus flow rate of N<sub>2</sub> added downstream, Ar discharge

We performed a series of systematic measurements of electron multiplier current as a function of supply voltage (Figure 21), discharge pressure (Figure 22), and discharge voltage (Figure 23). The roughly  $P^2$  scaling observed for the discharge pressure variation results from a combination of increased beam flux and reduced Ar<sup>\*</sup> residence time in the flow reactor (faster linear flow velocities) at the higher operating pressures. For these experiments, discharge operating pressures were limited to  $\leq 4$  torr in order to keep the pressure in the intermediate chamber at a safe level for operating the electron multiplier.

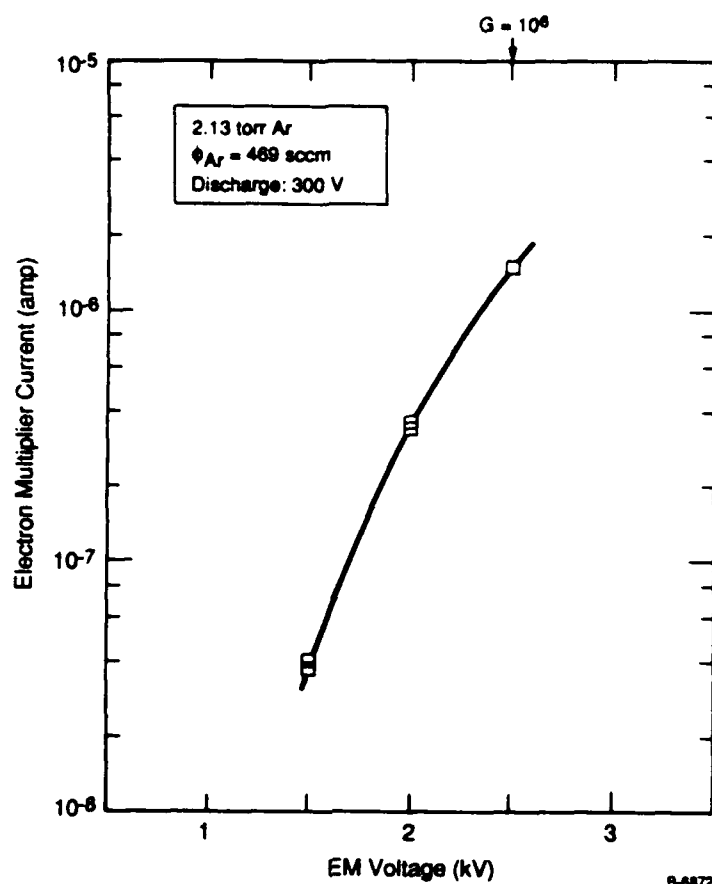
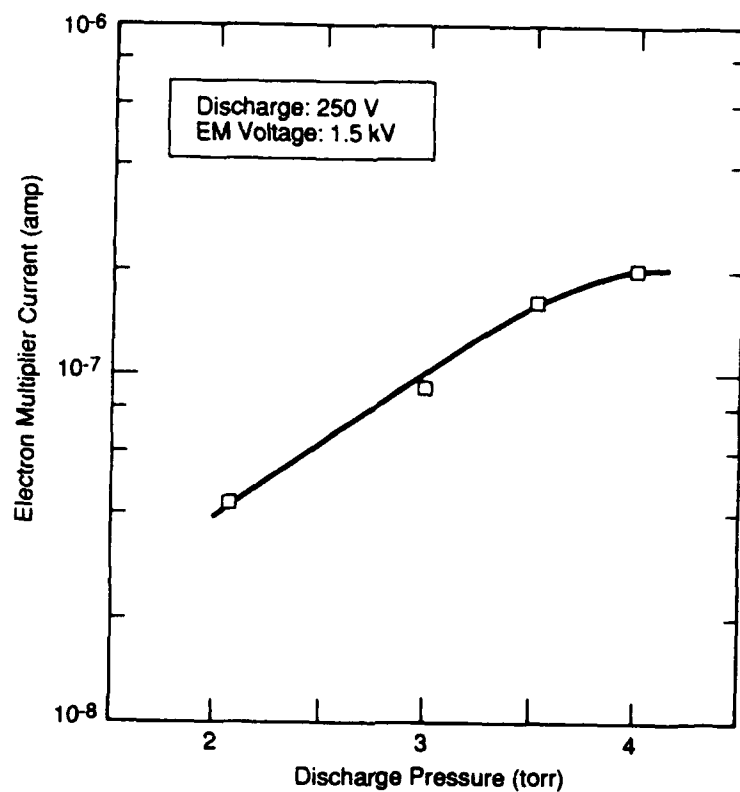


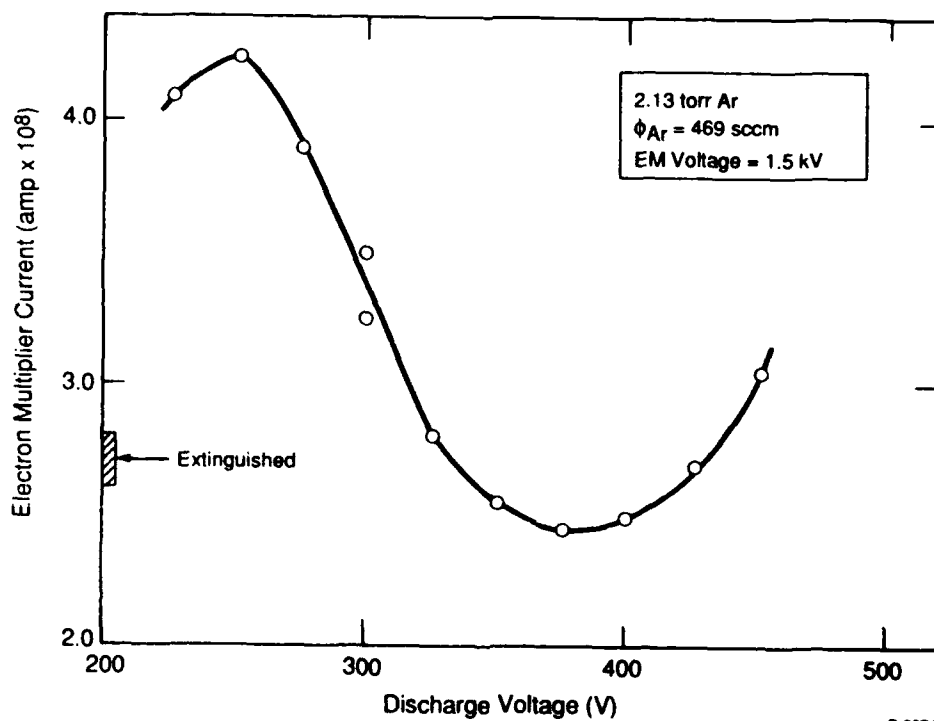
Fig. 21. Electron multiplier current versus multiplier supply voltage, Ar discharge

The observed variation of electron multiplier current with discharge voltage is characteristic of the production of metastables in a DC discharge of flowing argon. A similar curve, shown in Figure 24, was reported by Prince et al.,<sup>36</sup> who monitored the flame intensity from the  $\text{Ar}^* + \text{N}_2$  interaction as a function of discharge current. Prince et al. interpreted their results in terms of trade-offs between low current and high current discharge phenomena. At low currents, the low electron number density reduces the destruction rate of  $\text{Ar}^*$  through electron impact excitation and superelastic quenching. As the DC field increases, the increasing number density of energetic electrons destroys  $\text{Ar}^*$  via electron impact ionization. As the current (or voltage) continues to increase, ionization becomes



B-6873

Fig. 22. Electron multiplier current versus discharge gas pressure, Ar discharge



B-6874

Fig. 23. Electron multiplier current versus discharge voltage, Ar discharge

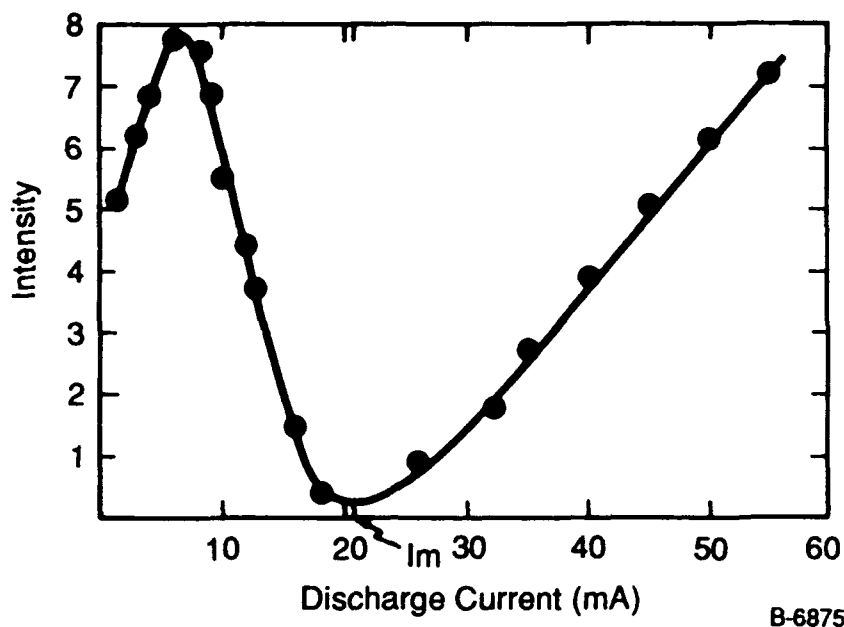


Fig. 24.  $N_2(C \rightarrow B)$  flame intensity versus discharge current, Ar discharge + downstream  $N_2$  (Ref. 36)

significant and the flame intensity (or electron multiplier signal) begins to increase again.

Prince et al.<sup>36</sup> argue that, for low current operation, the ion yield from a DC discharge is minimal, and the flame intensities are due almost entirely to metastable  $Ar^*$ . By analogy, we conclude that, for discharge voltages of 200 to 300V, the observed electron multiplier currents are due primarily to Auger quenching of metastable  $Ar(^3P_0, ^3P_2)$  on the collecting surface, with small contributions from VUV radiation and negligible contributions from charged species.

The data reported here provide an estimate of the  $Ar^*$  flux produced in the atomic beam, given that the electron multiplier gain is  $1 \times 10^6$  at a voltage of 2.5 kV. For a discharge pressure of 3 torr and operating voltage of 300V, we observe an apparent count rate of  $\sim 2 \times 10^7 \text{ s}^{-1}$ . However, the effective quantum efficiency (secondary electron yield) for  $Ar^*$  is probably 0.01 to 0.1; indeed, Borst<sup>35</sup> reports a value of 0.035 for thermal  $Ar^*$  on

a gas-covered Cu-Be-O electron multiplier, as inferred from extrapolations of Hagstrum's<sup>37</sup> results for  $\text{Ar}^+$  on  $\text{N}_2$ -covered tungsten surfaces. Using the Borst value for quantum efficiency, we estimate a metastable  $\text{Ar}^*$  flux of  $\sim 6 \times 10^8$  metastables/s at the detector (the beam area is smaller than the detector area).

The electron multiplier was about 10 cm closer to the beam source than typical target locations ( $\sim 38$  cm from the source), so the corresponding flux at the target would be  $\sim 3 \times 10^8$  metastables/s. It is clear that increasing the discharge operating pressure will increase this flux by at least a factor of two. This range of values compares reasonably well with our original design goal of  $\sim 10^9$  metastables/s at the target.

Based on our calculations of the total beam intensity ( $\sim 2 \times 10^{15}$  atoms/s at the target for a 1-mm aperture and 3 torr), the mole fraction of  $\text{Ar}^*$  in the beam is  $\sim 10^{-7}$ . This is consistent with our prior experience with metastable production by DC discharges in discharge flow reactors, where mole fractions of  $10^{-7}$  to  $10^{-6}$  are typically obtained. This result implies that there is relatively little metastable loss in the atomic beam sampling nozzle. Similarly, based on our prior experience with  $\text{N}_2(\text{A})$  and  $\text{He}^*$  generation in DC discharge-flow, we expect beam fluxes of  $\text{He}(2^3\text{S}, 2^1\text{S})$ , and  $\text{N}_2(\text{A}^3\Sigma)$  to be comparable in magnitude (to within a factor of  $\sim 3$ ) to those obtained for  $\text{Ar}^*$ .

We conclude from this exercise that the DC discharge-flow technique generated metastables as we expected, and that the metastables were efficiently extracted into a molecular beam to give reasonable fluxes on the target surface. In the next section, we discuss measurements of electron yields from interactions of metastable species and UV photons with surfaces.



### 3.2 Secondary Electron Flux Measurements

To measure electrons ejected from the target surface, the full beam-surface facility was operated for a clean Ni/NiO surface in UHV. The sample consisted of a piece of polished nickel (polycrystalline) mounted on the heating element at the end of the sample manipulator. Care was taken to ensure that the sample was electronically grounded. Prior experience with nickel surfaces indicates that the surface is covered with a coating of nickel oxide as a result of atmospheric exposure. Following evacuation of the UHV chamber, the sample and the chamber were baked until UHV conditions were achieved ( $\sim 1 \times 10^{-10}$  torr). The sample was bombarded by argon ions in an attempt to remove the oxide layer; this resulted in macroscopic roughening of the surface. This roughening creates a surface more relevant to practical systems (as opposed to a single crystal surface).

The quadrupole mass spectrometer was used to examine the helium beam in the UHV chamber. This was done to determine if the molecular beam might be contaminating the surface. The mass spectrometer cannot be positioned directly in the beam and must sample the beam after it has bounced off the sample. Figure 25 shows a mass spectrum of the UHV chamber after it has undergone a bakeout. The mass peaks that are seen are common to a clean, baked UHV chamber. Figure 26 is a mass spectrum with the discharge-excited molecular (helium) beam coming into the chamber. No new peaks other than helium are present and the previous peaks are reduced, probably due to the beam pushing some of the residual gas away from the mass spectrometer. Figure 27 is the same as Figure 26 but with the DC discharge in the flow tube turned off. No significant difference is seen. These figures show that the molecular beam is not a source of contamination in the UHV chamber and that the discharge in the flow tube is a remarkably clean process.

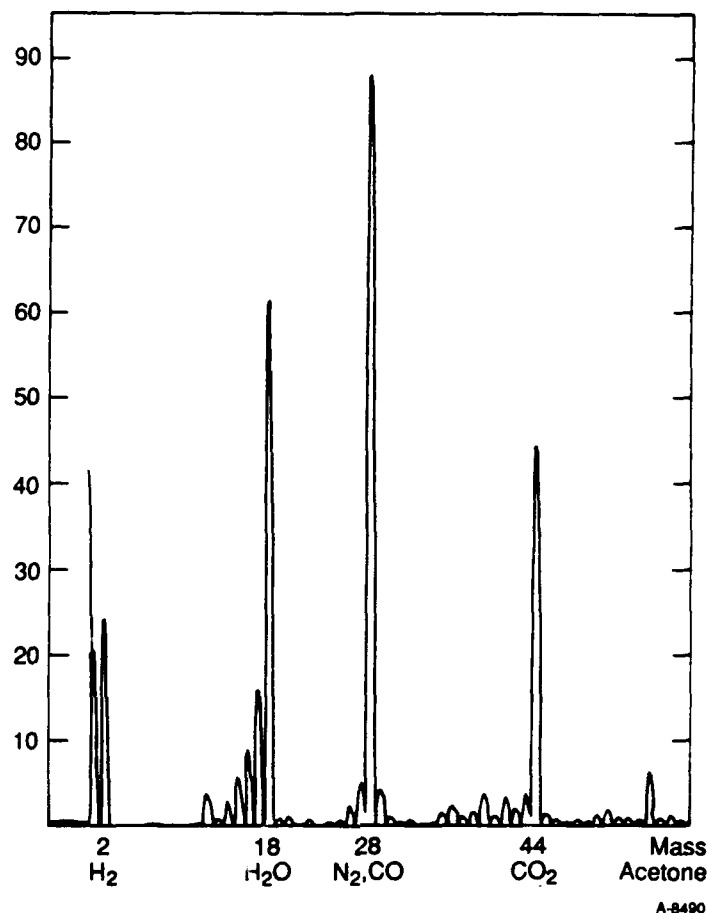


Fig. 25. Mass spectrum of baked UHV chamber.  $P_{\text{UHV}} = 1.4 \times 10^{-10}$  torr. No molecular beam into chamber. Intensity scale is arbitrary but the same for Figs. 25 through 27. Emission: 1 milliamp; electron multiplier: 1600V; range of scan: 0 to 100 amu, with mass values  $> 60$  not shown as no peaks were present. First peak in spectrum represents start of scan and is not a mass peak.

Figure 28 shows the electrical circuit that is used for metastable detection.

Metastables hitting the surface should cause emission of an electron whose kinetic energy is modulated by an AC voltage on the center grids of the retarding potential analyzer. A ramping voltage and/or a bias voltage is placed on the center grids to map out the energy distribution of the electrons that leave the target surface. A set of biased microchannel plates amplifies the signal from those electrons that are energetic enough to pass the ramping voltage on the grids.

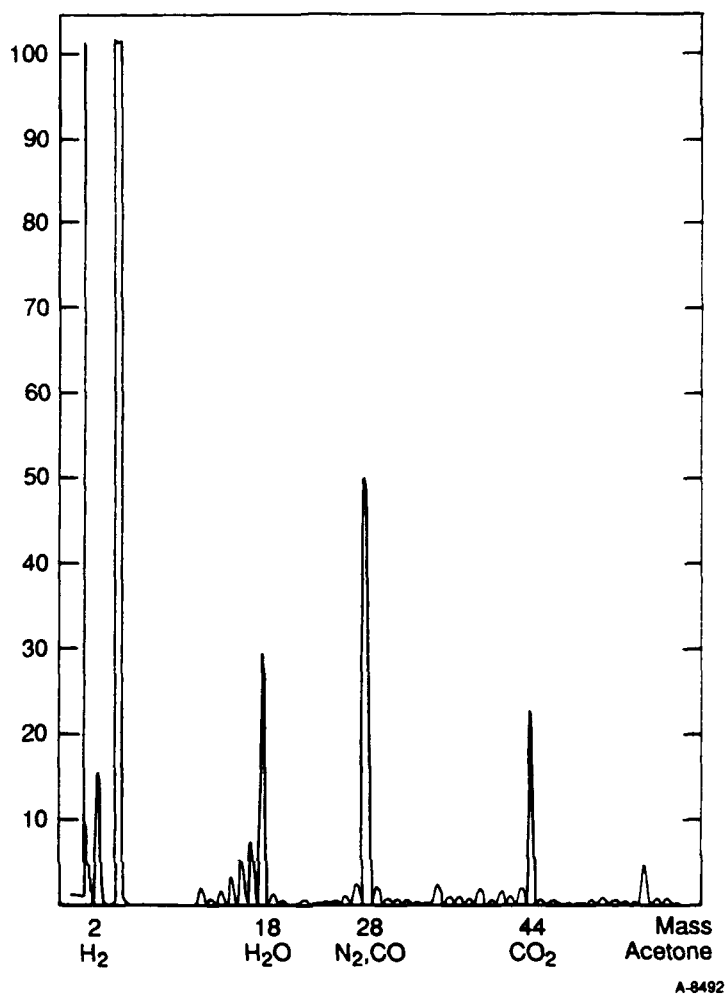


Fig. 26. Mass spectrum of UHV chamber with helium beam coming into chamber. DC discharge on.  $P_{\text{UHV}} = 9.2 \times 10^{-10}$  torr uncorrected for helium. Nozzle = 3 torr. See note in Figure 25 caption.

The RC box contains an RC circuit that acts as a high pass filter. This box will only pass the modulated AC signal and serves to remove the high anode voltage from the signal of interest. A current preamp then amplifies and converts the signal to a voltage, and a lock-in amplifier tuned to the grid modulation frequency is used to recover the signal which is the electron energy distribution. The circuitry and signal processing utilized here were copied directly from schematics employed and kindly provided by Prof. R.M. Martin's surface science laboratory at the University of California at Santa Barbara. All the electronics

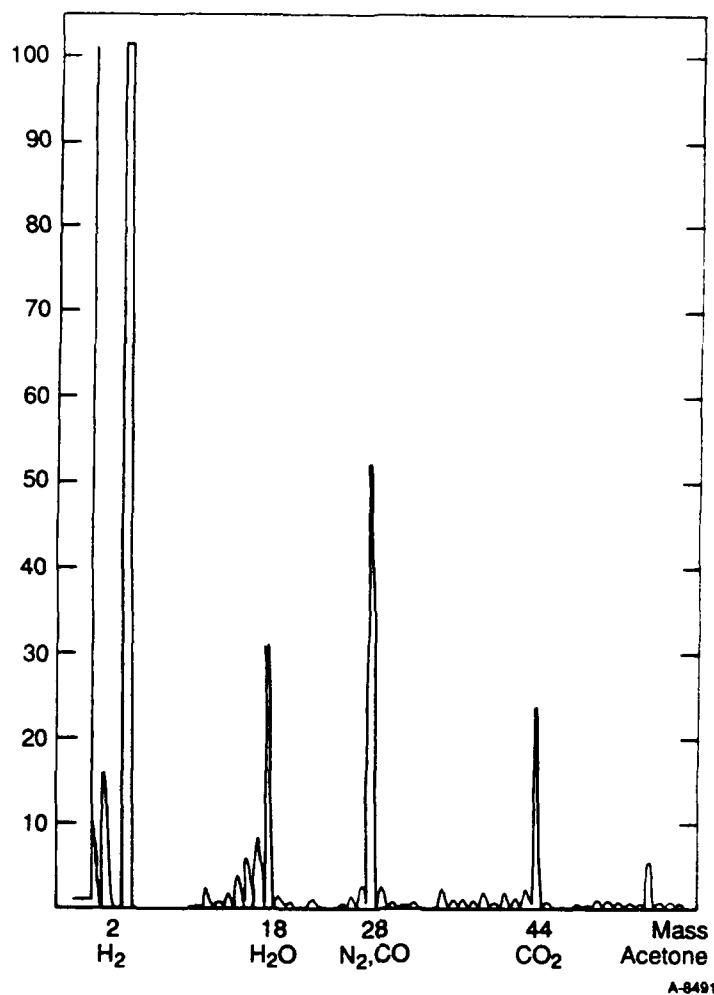


Fig. 27. Mass spectrum of UHV chamber with helium molecular beam coming into chamber. DC discharge off.  $P_{\text{UHV}} = 9.2 \times 10^{-10}$  torr uncorrected for helium.  $P_{\text{nozzle}} = 3$  torr. See note in Figure 25 caption.

outside the UHV chamber were bench tested with a function generator to be sure that the electronics could recover the desired signal.

### 3.2.1 Photoelectron Measurements

In order to test the performance of the electron energy analyzer, we used ultraviolet light to generate electron fluxes from the sample and from surrounding chamber surfaces. Two light sources were employed: a mercury pen lamp and a tunable dye laser, both directed at the sample surface through the adjacent window.

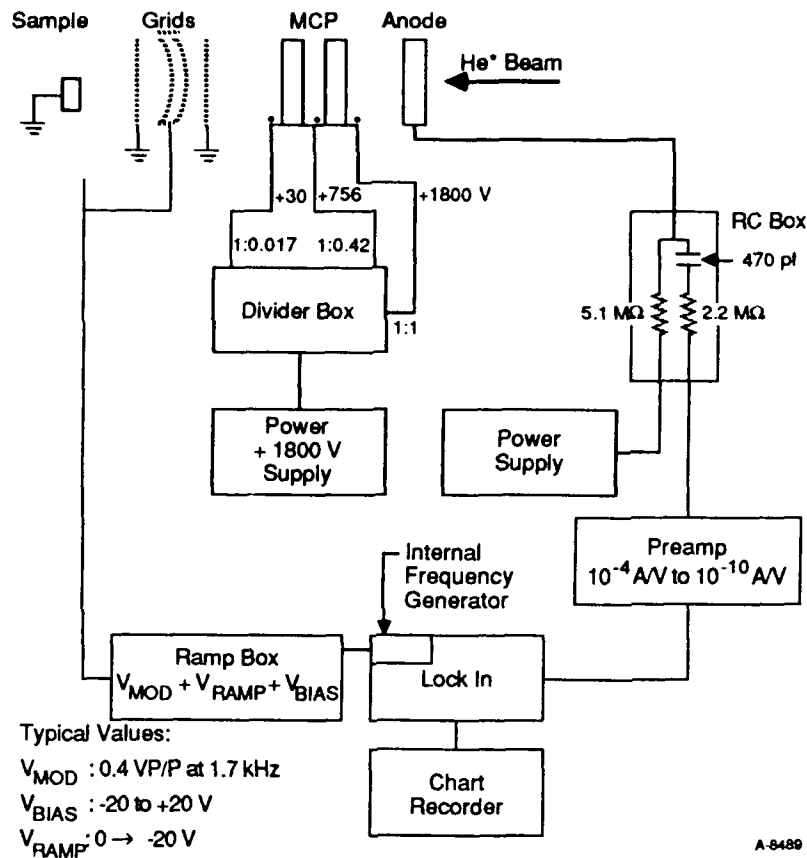


Fig. 28. Electrical circuit for metastable data collection

A mercury lamp was used to illuminate the chamber such that the mercury light would ionize chamber surfaces to produce a signal that could be seen with the energy analyzer. Figure 29 shows that a signal dependent upon the ramping voltage was observed. This indicates that the signal was from electrons generated at or outside the grids. The same spectrum was observed regardless of whether the metastable beam was in the chamber or not. This indicates that this signal was not from metastables but was a photoelectric effect from the chamber. Tests with optical filters showed that it was the 1849Å line from the mercury lamp that was causing the signal. The mercury light was then focused so that it just skimmed the face of the target with the results shown in Figure 30. A different spectrum

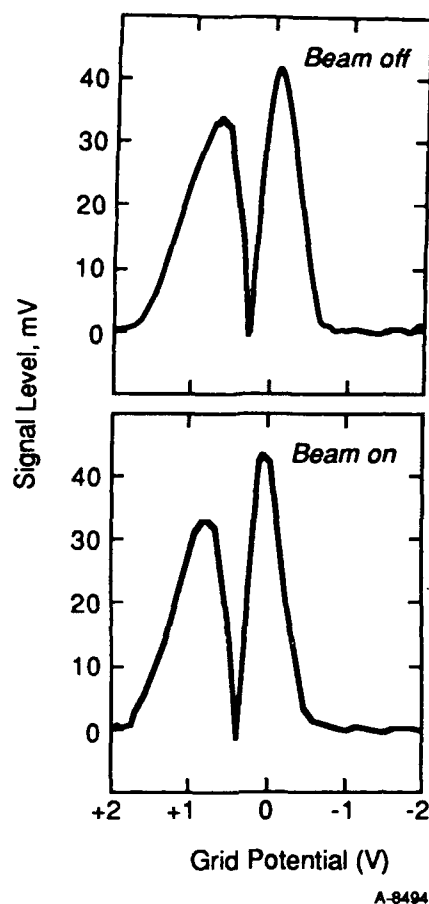
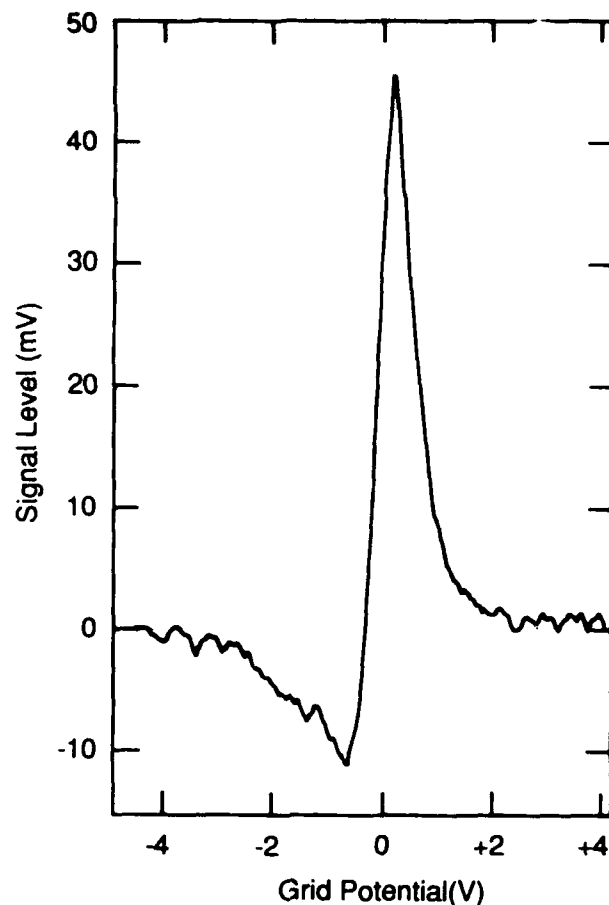


Fig. 29. Mercury lamp signal from energy analyzer. Light flooding into chamber.  $P_{\text{nozzle}} = 3$  torr He. Voltage observed on lock-in amplifier for pre-amp gain of  $10^{-9}$  A/V.

was observed indicating that the light must have illuminated a different surface, either on the target or on the manipulator. The shapes of the signal distributions in Figures 29 and 30 are difficult to interpret, particularly for the secondary (positive ion?) peak at positive grid voltages. In addition, it is intriguing to note that portions of the anode signal in Figure 30 are out of phase with each other. However, as these signals are not from metastables they were not investigated further. That an electron spectrum of any sort was observed indicates that the grids were working and that the microchannel plates were providing significant gain.

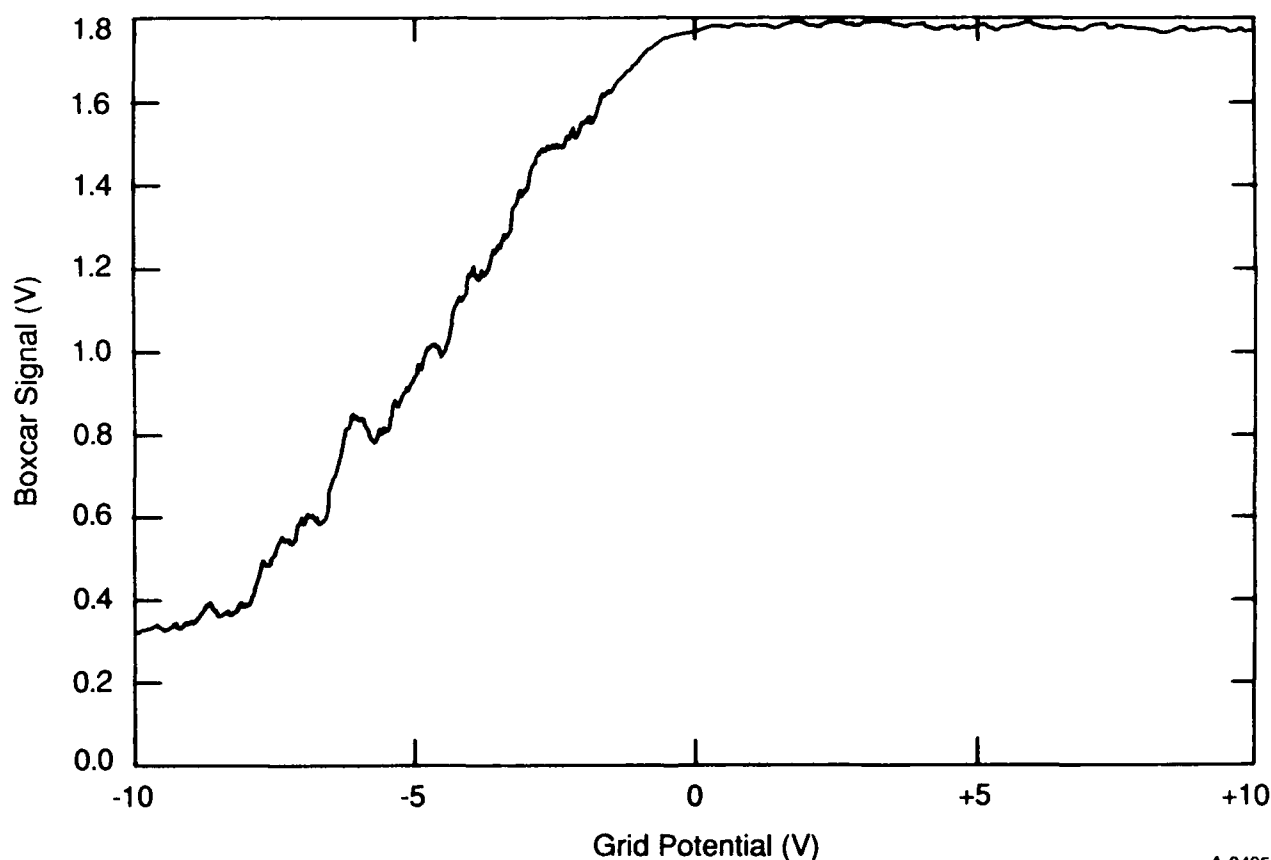


A-8493

Fig. 30. Mercury lamp signal from energy analyzer. Light focussed across face of Ni target.  $P_{\text{nozzle}} = 3$  torr He. Voltages observed on lock-in amplifier for pre-amp gain of  $10^{-7}$  A/V.

A Quantel YAG-pumped pulsed dye laser was used to try to detect helium metastables by laser photoionization. The dye laser wavelength was set to 245 nm (5.1 eV). The electronics were reconfigured to detect ions by biasing the grids from a large negative value to ground. The RC box was taken out of the circuit. Unfortunately, this attempt to detect metastables in the molecular beam was not successful as scattered light from the laser produced a large background signal from the microchannel plates. In order to perform the laser photoionization experiment, the microchannel plates and the incoming and outgoing laser light must be optically baffled, as discussed in Subsection 2.4.3.

In another experiment, this laser light was focused on the sample to see if an electron spectrum could be produced. Figure 31 shows integrated intensity versus ramping voltage as obtained with a gated boxcar signal averager (the differentiating AC voltage was not employed). This figure shows that electrons were being detected at the microchannel plates. The energy spectrum is obtained from the derivative of the curve in Figure 31. However, it is clear from Figure 31 that very little fine structure is evident in the differentiated spectrum. In contrast to the results for Hg lamp illumination, there is no derivative signal at positive grid potentials, and the observed electron energies extend to at least 7 to 8V.



A-8495

Fig. 31. Laser light focused onto Ni Target,  $\lambda = 245$  nm. Integrated intensity versus ramping voltage, signal voltage observed with boxcar integrator at  $15 \mu\text{s}$  gate width, pre-amp gain  $10^{-4}$  A/V. Laser at 10 Hz, boxcar averaging 30 shots/sample.



In summary, the observations of photoelectrons provide a qualitative indication of the performance of the electron energy analyzer. In particular, the detection of readily measurable signal even for unfocused illumination from the relatively weak mercury lamp at 6.7 eV suggests that the measurement sensitivity is substantial.

### 3.2.2 Metastable-Surface Quenching Measurements

The interaction of metastables with the sample surface was investigated by irradiating the surface with the discharge-generated molecular beam. Alignment of the beam and surface was routinely performed and verified by passing a HeNe laser beam through a window in the back of the discharge tube, through the nozzle, skimmer, and collimating orifices, and onto the sample surface.

In the absence of any direct observation of metastable species, the primary diagnostic for metastable quenching on the surface was the electron energy analyzer. Given the observed metastable flux of 3 to 6 x 10<sup>8</sup> metastables/s for discharge pressure of 3 to 4 torr, and a gain of 1 x 10<sup>7</sup> for the microchannel plates, the observed electron current should be ~ (5 to 10) x 10<sup>-4</sup>  $\gamma$ Q amp, where  $\gamma$  is the single-collision efficiency for quenching of the metastable on the surface and Q is fraction of quenching events that lead to electron ejection. From the data presented by Borst<sup>35</sup> for a gas-covered Cu-Be-O surface, we might expect  $\gamma$ Q values in the range 10<sup>-3</sup> to 10<sup>-1</sup>, giving electron currents well in excess of 10<sup>-7</sup> amp. This is readily detectable above our signal limit of 10<sup>-11</sup> amp.

Measurements were made with the discharge generated He(<sup>3</sup>S, <sup>1</sup>S), Ar(<sup>3</sup>P), and N<sub>2</sub>(<sup>3</sup> $\Sigma_u^+). In each case the copious production of metastables was confirmed by the intense blue flame observed upon addition of N<sub>2</sub> to the rare gas metastable flow. In the case of$

$\text{He}^*$ , this flame arises from Penning ionization of  $\text{N}_2$  to  $\text{N}_2^+(\text{B}^2\Sigma_u^+)$ , which promptly radiates near 391.4 nm.  $\text{Ar}^*$  produces a flame by exciting  $\text{N}_2(\text{C}^3\Pi_u)$ , which radiates promptly near 337.1 nm. This radiation initiates a rapid radiative cascade sequence through  $\text{N}_2(\text{B}^3\Pi_g)$  terminating in the formation of  $\text{N}_2(\text{A}^3\Sigma_u^+)$ .

Discharge pressures and voltages were varied from 1 to 10 torr and 200 to 500V. The sample was moved from directly in front of the electron collection grids to several inches away, and was rotated in and out of the beam. Measurements were made with the sample grounded and electrically floating. Under none of these conditions could any discernable electron ejection be observed.

For a nozzle pressure of 3 torr and a modulation voltage of 0.4V peak to peak at 1.7 kHz, the background level is  $1 \times 10^{-11}$  amp. Looking at the signal after the preamp but before the lock-in, there is a component with the same frequency as the modulation. This signal is present whether or not the beam is coming into the chamber and appears to represent pickup of the modulation waveform by the anode. When the beam is coming into the chamber there are additional spikes of  $1$  to  $3 \times 10^{-9}$  amp with no set frequency. These appear to be caused by particles with a negative charge as their numbers decrease slightly when a negative bias is applied to the center grids. The random nature of these spikes indicates that they are photoelectrons caused by stray photons from the discharge in the flow tube. These noise levels are very small and indicate that we should not have any trouble seeing the signal that we expect from metastable impact. Nevertheless, no increase in modulated signal above the background could be observed for any of the several discharge and sample configurations attempted. This included a discharge configuration in which the

discharge was extended to the nozzle orifice by using the nozzle as one of the electrodes: the "photon noise" increased as expected, but no increase in modulated signal occurred.

The absence of ramp-modulated signal means that no electrons entered the analyzer from the UHV chamber. Given that we have independently verified the metastable fluxes and the performance of the electron detection system, we conclude that essentially no electrons were ejected from the surface. Consideration of our detection limit gives the upper bound  $\gamma Q \leq 1 \times 10^{-8}$  for  $\text{He}^*$ ,  $\text{Ar}^*$ , and  $\text{N}_2(\text{A})$ . Since we expect  $\gamma$  to be near unity, we conclude that the electron ejection efficiency,  $Q$ , is less than  $10^{-8}$  for a rough, polycrystalline Ni/NiO surface. The presence of adsorbed monolayers of argon and other species ( $\text{CO}_2$ ,  $\text{H}_2\text{O}$ ) may be contributing to this small electron yield.

#### 4. DISCUSSION AND RECOMMENDATIONS

Our observation of vanishingly small electron ejection probabilities is surprising, especially in view of previous results for UHV/single crystal metals<sup>1-9</sup> and for gas-covered laboratory metals.<sup>35,38</sup> Borst<sup>35</sup> measured secondary electron currents for He( $2^3S$ ), N<sub>2</sub>( $a^1\Pi$ ), N<sub>2</sub>( $A^3\Sigma$ ), and CO( $a^3\Pi$ ) quenching on the Cu-Be-O dynode of a nude electron multiplier in a conventional high vacuum chamber, and determined secondary electron yields which essentially followed the response curve of the material. Moreover, he found that these results fell on the same curve as extrapolated yields for Ne\*, Ar\*, Kr\*, and Xe\* based on Hagstrum's<sup>37</sup> data for rare gas ions on nitrogen-covered tungsten surfaces. Rundel et al.<sup>38</sup> also report secondary electron current measurements, for He( $2^1S, 2^3S$ ) on gas-covered stainless steel, and argue that the secondary electron ejection coefficient for a given metastable species depends strongly on the nature of the surface and its state of contamination.

Given that Borst<sup>35</sup> reported secondary electron yields of 0.15, 0.0085, and 0.0012 for He( $2^3S$ ), N<sub>2</sub>( $a^1\Pi$ ), and N<sub>2</sub>( $A^3\Sigma$ ), respectively, while Rundel et al.<sup>38</sup> reported values of 0.74 for He( $2^3S$ ) and 0.49 for He( $2^1S$ ), we would expect to observe a substantial flux of electrons ejected from the surface in our experiments. The fact that we do not observe this suggests that, while metastable quenching on rough gas-covered metal surfaces undoubtedly produces current in the bulk metal, it does not result in ejection of electrons from the surface into the gas phase. This is in marked contrast to photon impact, for which we observe copious surface electron ejection.

The original objective of this work was to evaluate mechanisms for energetic couplings between a discharge plasma and surrounding surfaces, specifically via metastable quenching. The primary pathways by which metastable-surface quenching can couple back to the plasma are expected to be secondary electron ejection, partial deactivation of molecular metastables (e.g.,  $N_2(A)$  to  $N_2(X,v)$ ), and scattering/excitation of gas adsorbates. Our conclusions are as follows. First, secondary electron ejection from rough contaminated metal surfaces appears to be remarkably inefficient. This effect needs to be studied much more comprehensively for metals and insulators, beginning with clean single crystal measurements in UHV and progressing systematically toward well-characterized rough/contaminated materials. Additional electron current measurements, of the type described by Rundel et al.,<sup>38</sup> should also be performed to compare surface and in-depth behavior.

Second, since metastable quenching on gas-covered surfaces results in so little electron ejection, it is possible that substantial energy transfer to adsorbed species may occur. This could be examined by doping surfaces with species such as NO or NO<sub>2</sub>, and detecting the energy distributions of molecules scattered from the surface by metastable impact, using laser-induced fluorescence or time-of-flight mass spectrometry.

Third, the possibility of partial deactivation to an intermediate excited state species, which is then scattered back into the plasma, is a significant issue for molecular metastables. Good examples of such a process are the surface quenching of  $N_2(A^3\Sigma)$  to form vibrationally excited  $N_2(v)$ , or quenching of  $CO(a^3\Sigma)$  to  $CO(v)$ . Unfortunately, due to limitations in detection sensitivities, it seems unlikely that such processes can be studied in UHV beam-surface scattering conditions. However, these processes could be investigated for contaminated laboratory surfaces in a flow reactor configuration, where secondary metastable

number densities can be made in detectable quantities, e.g.,  $N_2(v)$  by gas-phase Penning ionization.<sup>39</sup>

In general, it appears that the scattered energetic products of the metastable-surface interaction are extremely sensitive to surface characteristics which are difficult to control in both the experimental apparatus and the plasma device, such as surface atomic composition, microscopic and macroscopic roughness, and gaseous adsorbate coverage. Comprehensive investigation of these effects will require detailed, systematic measurements at high detection sensitivity over a broad range of surface types and conditions. Alternatively, spatially resolved species diagnostics over practical surfaces in discharge plasmas might provide phenomenological data with which to test models of plasma-surface interactions. A clear implication of these results is that the macroscopically roughened surfaces covered with adsorbates such as those present in plasma processing systems will have negligible electron production at the walls due to metastable quenching. In contrast, production of electrons by energetic UV photons appears to be quite efficient for these surfaces. Experiments to quantify photoelectron dependencies may be highly relevant to process understanding.

## 5. REFERENCES

1. Bozso, F., Yates, J.T., Jr., Arias, J., Metiu, H., and Martin, R.M., "A Surface Penning Ionization Study of the CO/Ni(111) System," *J. Chem. Phys.* **78**, 4256 (1982).
2. Bozso, F., Arias, J., Hanrahan, G., Martin, R.M., Yates, J.T., Jr., and Metiu, H., "Effect of Surface Electronic Structure on the Deexcitation of He2<sup>1</sup>S Metastable Atoms," *Surf. Sci.* **136**, 257 (1984).
3. Bozso, F., Arias, J., Yates, J.T., Jr., Martin, R.M., and Metiu, H., "The Detection of the 2Π\* Orbital of CO and NO Chemisorbed on Ni(111) by Surface Penning Ionization Electron Spectroscopy," *Chem. Phys. Lett.* **94**, 243 (1983).
4. Harada, Y., Ozaki, H., and Ohno, K., "Electron Spectroscopy of Semiconductor Surface by Impact of Metastable Rare-Gas Atoms: Selenium," *Solid State Comm.* **49**, 71 (1984).
5. Munakata, T., Ohno, K., and Harada, Y., "Application of Penning Ionization Electron Spectroscopy to the Study of the Outermost Layers of the Solid Surface," *J. Chem. Phys.* **72**, 2880 (1980).
6. Roussel, J., Boiziau, C., Nuvolone, R., and Reynaud, C., "Electron Ejection Mechanism in the He 2<sup>3</sup>S Interaction with a Clean and a Molecularly Covered Ni(111) Surface," *Surf. Sci. Lett.* **110**, L634 (1981).
7. Hagstrum, H.D., "Excited-Atom Deexcitation Spectroscopy Using Incident Ions," *Phys. Rev. Lett.* **43**, 1050 (1979).
8. Conrad, H., Ertl, G., Küppers, J., Wang, S.W., Gérard, K., and Haberland, H., "Penning-Ionization Electron Spectroscopy of Chemisorbed CO," *Phys. Rev. Lett.* **42**, 1082 (1979).
9. Conrad, H., Ertl, G., Küppers, J., Sesselmann, W., and Haberland, H., "Electron Spectroscopy of Surfaces by Impact of Metastable He Atoms: CO on Pd(11)," *Surf. Sci.* **121**, 161 (1982).
10. Boiziau, C., Garot, C., Nuvolone, R., and Roussel, J., *Surf. Sci.* **91**, 313 (1980).
11. Fomenko, V.S., "Handbook of Thermionic Properties," Samsonov, G.V., ed. (translated from Russian) Plenum Press Data Division (New York, 1966).
- 12a. Brown, L.S., and Bernasek, S.L., "Vibrational Excitation in the CO<sub>2</sub> Product of the Oxidation of CO on Platinum: Coverage Dependence and Implications on Reaction Dynamics," *J. Chem. Phys.* **82**, 2610 (1985).

- 12b. Kubiak, G.D., Sitz, G.O., and Zare, R.N., "Recombination Desorption of  $H_2$  and  $D_2$  from Cu(110) and Cu(111): Determination of Non-Equilibrium Non-Vibrational Distributions," J. Chem. Phys. 81, 6397 (1984).
13. Caledonia, G.E., Krech, R.H., Green, B.D., and Rosen, D.I., "Novel O-Atom Source for Material Degradation Studies," Physical Sciences Inc. Technical Report TR-517, June 1985.
14. Swenson, G.R., Mende, S.B., and Clifton, K.S., "Ram Vehicle Glow Spectrum," Geophys. Res. Lett. 12, 97 (1985).
15. Green, B.D., "Atomic Recombination into Excited Molecular States - A Possible Mechanism for Shuttle Glow," Geophys. Res. Lett. 11, 576 (1984).
16. deJaepere, S., Willemsih, and Vinckler, C., "The Interactions Between Afterglow Products of Microwave-Induced Plasmas and Solids," J. Phys. Chem. 86, 3569 (1982).
17. Predictions from computer model described in: Jackmann, C.H., Garvey, R.H., and Green, A.E.S., "Electron Impact on Atmospheric Gases. I. Updated Cross Sections," J. Geophys. Res. 82, 5081 (1977).
18. Piper, L.G., Richardson, W.C., Taylor, G.W., and Setser, D.W., "Quenching Processes and Rate Constants for Interaction of Metastable Argon Atoms with Diatomic and Triatomic Molecules," Disc. Faraday Soc., 53, 100 (1972).
19. Piper, L.G., Velazco, J.E., and Setser, D.W., "Quenching Cross Sections for Electronic Energy Transfer Reactions Between Metastable Argon Atoms and Noble Gases and Small Molecules," J. Chem. Phys. 59, 3323 (1973).
20. Setser, D.W., Piper, L.G., and Velazco, J.E., "Quenching Rate Constants for the  $Ar(^3P_0)$ ,  $Ar(^3P_2)$ , and  $Xe(^3P_2)$  States," Rad. Res. 59, 441 (1974).
21. Piper, L.G., "Electronic Energy Transfer Between Metastable Argon Atoms and Ground-State Oxygen Atoms," Chem. Phys. Letts. 28, 276 (1974).
22. Anderson, J.B. and Fenn, J.B., "Velocity Distributions in Molecular Beams from Nozzle Sources," Phys. of Fluids 8, 780 (1965).
23. Shapiro, A.H., The Dynamics and Thermodynamics of Compressible Fluid Flow (Ronald Press Co,m New York, 1953).
24. Simons, G.A., "Effects of Nozzle Boundary Layers on Rocket Exhaust Plumes," AIAA J. 10, 1534 (1972).



25. Ashkenas, H. and Sherman, F.S., 4th Symposia on Rarefied Gas Dynamics (Toronto, 1964), J.H. DeLeeuw, Ed. (Academia Press, New York, 1963), p. 2.
26. Osterstrom, G., Methods of Experimental Physics, Vol. 14 (Academic Press, New York, 1979), p. 247.
27. Kruger, C.H., and Shapiro, A.H., "Vacuum Pumping with a Bladed Axial-Flow Turbomachine," Trans. Natl. Symp. Vac. Technol, 7th (Pergamon Press, New York, 1961), p. 6.
28. Ertl, G. and Küppers, J., Low Energy Electrons and Surface Chemistry (VHC, Florida, 1985), p. 11.
29. Alvery, M.D., Dresser M.J., and Yates, J.T., "Metastable Angular Distributions from Electron-Stimulated Desorption," Phys. Rev. Lett. 56, 367 (1986).
30. Taylor, N.J., "Resolution and Sensitivity Considerations of an Auger Electron Spectrometer Based on Display LEED Optics," Rev. Sci. Instr. 40, 792 (1969).
31. Conrad, H., Doyen, G., Ertl, G., Küppers, J., Sesselmann, W., and Haberland, H., "Reflection of Metastable He Atoms from Solid Surfaces," Chem. Phys. Lett. 88, 281 (1982).
32. Johnson, P.M. and Otis, C.E., "Molecular Multiphoton Spectroscopy with Ionization Detection," Ann. Rev. Phys. Chem. 32, 139 (1981).
33. Marinelli, W.J., Carleton, K.L., Kaufman, D., and Gittins, C., Spacecraft Thermal Energy Accommodation from Atomic Recombination, PSI-TR-1017, Final Report, Contract No. NAS-9-17815, Physical Sciences Inc., April 1990.
34. Marinelli, W.J. and Green, B.D., "Collisional Quenching of Atoms and Molecules on Spacecraft Thermal Protection Surfaces," AIAA Paper No. 88-2667, 1988 (reproduced in Appendix A).
35. Borst, W.L., "Secondary Electron Yields from CuBeO Surface by Thermal CO, N<sub>2</sub>, and Noble Gas Metastables," Rev. Sci. Instrum. 42, 1543 (1971).
36. Prince, J.F., Collins, C.B., and Robertson, W.W., "Spectra Excited in an Argon Afterglow," J. Chem. Phys. 40, 2619 (1964).
37. Hagstrum, H.D., Phys. Rev. 104, 1516 (1956).
38. Rundel, R.D., Dunning, F.B., Howard, J.S., Riola, J.P., and Stebbings, R.F., "A Gas Cell Method for the Measurement of Secondary Electron Ejection Coefficients for Metastable Atoms on Metal Surfaces," Rev. Sci. Instrum. 44, 60 (1973).

39. Piper, L.G. and Marinelli, W.J., "Determination of Non-Boltzmann Vibrational Distributions of  $N_2(X,v)$  in He/ $N_2$  Microwave-Discharge Afterglows," J. Chem. Phys. 89, 2918 (1988).

APPENDIX A

RETARDING POTENTIAL RAMP GENERATOR

FOR ELECTRON ANALYZING SYSTEM

USER MANUAL AND THEORY OF OPERATION

## I. INTRODUCTION

The ramp generator circuit is divided into six sections:

- 1) Clock
- 2) Counter
- 3) D/A converter
- 4) Summing amplifier
- 5) Sample bias supply
- 6) Power supplies.

The clock circuit generates the time base for the ramp, and is based on a RM4152T Voltage-to-Frequency converter.

The counter generates a count from 0 to 4095, causing the 12-bit D.A converter to output its entire range of voltages.

The D/A (Digital-to-Analog) converter converts the digital count to the ramp voltage, and is based on a AD7541A monolithic converter and an 0P07E precision operational amplifier.

The summary amplifier adds the ramp voltage, the bias voltage and the modulation voltage, and amplifies them to the full scale output range.

The sample bias supply is simply an adjustable voltage divider between the +48V and -48V supplies.

The power supplies provide power at +5V, +15V, -15V, +48V, and -48V for the circuitry.

## II. INPUTS

### A. Modulation Voltage - Vmod (P1)

This input has a range of -10V to +10V, and an input impedance of 1000 ohms. It is AC-coupled to remove any DC component of the modulation voltage, and has a frequency range of approximately 1 KHz to 25 KHz. It is scaled by the Modulation Gain control by any factor from 0 to 2, and is added (non-inverted) to the retarding potential output.

### B. Optional External Clock Input (P2)

When the Clock Select Switch is set to "external," an externally generated clock signal can be input for use as the ramp generator's clock. The frequency should be 4096 times the inverse of the required ramp period.

This input requires a TTL-compatible (0 to 5V) signal, and the input impedance is approximately 5K ohms.

### C. AC Power (P11)

This connector is the source of AC power for the ramp generator. The connector is integrated within a fused, filtered power module to minimize conducted EMI from the ramp generator.

## III. OUTPUTS

### A. Retarding Potential -Vrp (P3 and P4)

This output is the sum of the ramp voltage, the ramp bias voltage, and the modulation voltage, as expressed by the following equation (within the output range noted below):

$$\begin{aligned} V_{rp} = & 3 * V_{ramp}(t) \\ & + G_m * V_{mod} \\ & + 2 * V_{rb} \end{aligned}$$

$V_{ramp}(t)$  is the output of the D/A converter ramp generator and is equal to:

$$V_{ramp}(t) = M * t / 4096$$

where  $t$  sweeps from 0 to 4095 (for the upward sweep) or from 4095 to 0 (for the downward sweep) and  $M$  is adjustable from +10V to -10V (ramp slope control).

$G_m$  is adjustable from 0 to 2 (modulation gain control), and  $V_{rb}$  is adjustable from +15V to -15V (ramp bias control).

The output impedance is approximately 10K ohms.

The output range is limited to within approximately  $\pm 45V$ , and externally applied voltages in excess of this may damage the summing amplifier.

There are two connectors for this output so that the exact output voltage can be monitored directly.

### B. Ramp Voltage Monitor - $V_{ramp}$ (Pr)

This output is  $V_{ramp}(t)$  as described above. The output impedance is approximately 10K ohms.

### C. Ramp Bias Voltage Monitor - $V_{rb}$ (P6)

This output is  $V_{rb}$  as described above. The output impedance varies from 10K ohms (at the extremes) to 20K ohms (at 0V).

#### D. Sample Bias Voltage - Vbias (P7 and P8)

This output is adjustable from + 45V to -45V, and is simply an adjustable voltage divider connected across the  $\pm 1$  45V supply. The output impedance varies from 10K ohms (at the extremes) to 20K ohms (at 0V).

There are two connectors for this output so that the exact output voltage can be monitored directly.

#### E. Ramp Start (P9)

Ramp Start is a TTL-compatible signal which goes high for one clock period when the ramp counter changes from 4095 to 0 (or from 0 to 4095 (when counting down). It also goes high whenever the ramp is manually reset with the Ramp Reset switch. The training edge transition occurs when the ramp changes from 0 to 1 (counting up) or from 4095 to 4094 (counting down).

#### F. Clock Output (10)

When the Clock Select switch is set to "internal," the TTL-compatible clock signal is available for monitoring at this output.

### IV. CONTROLS

#### A. Ramp Hold (SW1)

When the ramp hold switch is on (off-center), the ramp stops at the current value. The upper position is stationary, the lower is momentary.

#### B. Ramp Free-Run (SW2)

When the free-run switch is on (up), the ramp generator sweeps through its range continuously. When the switch is off, the ramp stops at its final value until reset.

#### C. Ramp Reset (SW3)

When the ramp reset switch is on (off-center), the ramp is reset to its initial value. The upper position is stationary, the lower is momentary.

#### D. Ramp Up/Down (SW4)

When the up/down switch is in the "up" position, the ramp generator counter starts at 0 and ends at 4095, which causes  $V_{ramp}(t)$  to vary from 0V to  $M * 4095/4096$ .

When this switch is in the "down" position, the ramp generator counter starts at 4095 and ends at 0, which causes  $V_{ramp}(t)$  to vary from  $M * 4095/4096$  to 0.

#### E. Ramp Period (VR1)

The ramp period control varies the frequency of the clock generator from approximately 11 Hz to approximately 4096 Hz. This varies the ramp period from approximately 370s to 1s.

#### F. Ramp Slope (VR2)

The ramp slope control adjusts the slope of  $V_{ramp}(t)$ . the slope can be positive or negative, and the ramp can sweep from 0V to  $\pm 10V$  (or vice-versa).

#### G. Ramp Bias (VR3)

The ramp bias control adjusts the bias voltage  $V_{rb}$  added to the ramp voltage. The range is from +15V to -15V.

#### H. Modulation Gain (VR4)

The modulation gain control adjusts the percentage ( $G_m$ ) of the modulation voltage  $V_{mod}$  which is added to the retarding potential output  $V_{rp}$ .

#### I. Sample Bias (VR5)

The sample bias control adjusts the sample bias voltage  $V_{bias}$ . The range is from +45V to -45V.

#### J. Modulation Off (SW5)

When this switch is in the "up" position, the modulation voltage is eliminated from the  $V_{rp}$  output, as if  $G_m$  was set to 0.

#### K. Ramp Bias Off (SW6)

When this switch is in the "up" position, the ramp bias voltage is eliminated from the  $V_{rp}$  output, as if  $V_{rb}$  was set to 0V.

#### L. Ramp Off (SW7)

When this switch is in the "up" position, the ramp voltage  $V_{ramp}(t)$  is eliminated from the output, as if the ramp slope  $M$  was set to 0V.

#### **M. Clock Select (SW8)**

When the clock select switch is in the "internal" position, the internal clock generator circuit supplies the time base for the ramp generator, and the clock can be monitored at the clock output (P6).

When the clock select switch is in the "external" position, the internal clock generator is disconnected, and an external clock can be used to supply the ramp generator time base.

#### **N. Power (SW9)**

The power switch controls the application of AC power to the ramp generator.



**APPENDIX B**  
**COLLISIONAL QUENCHING OF ATOMS AND MOLECULES ON**  
**SPACECRAFT THERMAL PROTECTION SURFACES**

[AIAA Paper No. 88-2667, 1988 (PSI-SR-369) reproduced in its entirety]

# AIAA'88

AIAA Paper No. 88-2667

## **COLLISIONAL QUENCHING OF ATOMS AND MOLECULES ON SPACECRAFT THERMAL PROTECTION SURFACES**

**W.J. Marinelli  
Physical Sciences Inc.  
Research Park, P.O. Box 3100  
Andover, MA 01810**

**For permission to copy or republish, contact the American Institute of Aeronautics and Astronautics  
370 L'Enfant Promenade, S.W., Washington, D.C. 20024**

# COLLISIONAL QUENCHING OF ATOMS AND MOLECULES ON SPACECRAFT THERMAL PROTECTION SURFACES

W.J. Marinelli and B.D. Green  
Physical Sciences Inc.  
Research Park, P.O. Box 3100  
Andover, MA 01810

## Abstract

We present the preliminary results of an on-going research program to determine energy partitioning to spacecraft thermal protection materials due to atom recombination at the gas-surface interface. The primary focus of the research is to understand the catalytic processes which determine heat loading on Shuttle, AOTV, and NASP thermal protection surfaces in non-equilibrium flight regimes. In our experiments we employ highly sensitive laser diagnostics based on laser-induced fluorescence (LIF) and resonantly enhanced multiphoton ionization spectroscopy (REMPI) to detect atoms and metastable molecules. At low temperatures a discharge flow reactor is employed to measure deactivation/recombination coefficients for O-atoms, N-atoms, and  $O_2(^1\Delta)$ . We present detection methods for measuring O-atoms,  $O_2(^1\Delta)$ , and  $N_2(X,v=19)$  and results for deactivation of  $O_2(^1\Delta)$ , and O-atoms on reaction-cured glass and Ni surfaces. Experiments now underway employ gas-surface scattering to measure deactivation efficiencies at temperatures up to 2000 K. Both atom recombination and metastable product formation are examined. Radio-frequency discharges are used to produce highly dissociated beams of atomic species at energies characteristic of the surface temperature. Auger electron spectroscopy is employed as a diagnostic of surface composition in order to accurately define and control measurement conditions.

## Introduction

The motivation for the measurements described in this paper is to improve our understanding of the aerothermodynamic problems associated with hypervelocity flight at high altitudes. These problems have received renewed attention due to the proposed development of two advanced space transportation systems: the aero-assisted orbital transfer vehicle (AOTV), and a small, rapid-response, manned, and maneuverable vehicle, which takes off from earth as a conventional aircraft, enters near-earth orbit, and reenters the atmosphere to land at a conventional airstrip (NASP). These concepts are in the design phases and the aerothermodynamic problems associated with reentry have been recently reviewed.<sup>1</sup>

The primary heating pulse for these vehicles on reentry will occur at altitudes above 80 km where non-equilibrium radiative and chemical processes will provide a substantial heat load to the thermal protection surfaces. Ablative surfaces are not desirable for these repeat usage systems. Various forms of thermal protection systems have been proposed for these vehicles including metallic structures,<sup>2</sup> and a hybrid carbon-carbon/reusable surface insulation/standoff metallic surface.<sup>3</sup>

Both of these systems suffer problems from the temperature restrictions on the non-ablative metallic skin. A critical issue in the design of these surfaces is the catalytic nature of the materials with respect to recombination of N- and O-atoms formed from shock-heated air. At issue is the degree to which energy released in recombination is partitioned to the surface (energy accommodation) and what states of the resulting molecule are formed. A second issue concerns the fate of energetic species formed in the recombination process. These species may undergo collisions with the thermal protection surfaces and deposit additional energy. The primary goal of our research is to understand the total energy accommodation process.

Much of our existing knowledge concerning thermal energy accommodation to spacecraft surfaces during hypersonic reentry comes from the laboratory and Shuttle orbiter flight data of Scott and coworkers<sup>4-7</sup> at NASA/JSC and Rakich and coworkers<sup>8-11</sup> at NASA/Ames. A review of the effects of non-equilibrium and wall catalysis on Shuttle heat transfer has recently been published by Scott.<sup>7</sup> Flight data recorded during reentry have not explicitly verified non-equilibrium conditions; however, these conditions are inferred from heat transfer measurements when compared with reacting flowfield model calculations. Flight data on heat transfer were obtained from several instrumented high-temperature reusable surface insulation (HRSI) tiles coated with either RCG (non-catalytic) or a highly catalytic iron-cobalt-chromia spinel (C74C). Data were obtained on missions STS-2, -3, and -5. Differences in skin temperatures between the RCG and spinel coated tiles is taken as evidence of incomplete thermal accommodation during recombination (non-equilibrium behavior).

Calculations<sup>7</sup> show that, in most of the flight regime associated with high heat flux, oxygen near the surface is fully dissociated. However, the more stable  $N_2$  molecule is substantially less than fully dissociated at all points along the reentry path and thus non-equilibrium  $N_2$  exists throughout the regime where  $N_2$  dissociation is important. Hence, the bulk of the non-equilibrium chemistry to be studied involves  $N_2$ . Curiously, it has been found that normalized heat fluxes measured on the windward centerline of the Orbiter increased by nearly 20 percent from STS-2 to -5. This is potentially due to changes in the surface properties such as emittance or catalytic efficiency and raises the issue of surface contamination and durability.

Laboratory measurements of accommodation coefficients for reentry surfaces come largely from the work of Scott.<sup>4,7</sup> Surface energy transfer accommodation coefficients for N- and O-atoms were inferred from stagnation point heat flux measurements in a high-temperature dissociated arc jet flow. Measurements were made in reference to accommodation to a standard Ni surface of known

catalytic efficiency. Accommodation coefficients are defined in these studies as:

$$\gamma = \gamma' \beta \quad (1)$$

where  $\gamma'$  is the atom loss probability per wall collision and  $\beta$  is the fraction of the dissociation energy released to the surface per collision. The coefficient,  $\gamma$ , was determined as a function of temperature on RCG and C742-coated HRSI. These coefficients could be described by an Arrhenius-type expression for  $\gamma_0$  and  $\gamma_N$  on RCG and are given by:

$$\gamma_0 = 16 e^{-10271/T_v} \quad 1400 < T_v < 1650 \text{ K} \quad (2)$$

$$\gamma_N = 0.0714 e^{-2219/T_v} \quad 950 < T_v < 1670 \text{ K} \quad (3)$$

where  $T_v$  is the wall temperature. Similar measurements on C742-coated HRSI yielded Arrhenius-type expressions of:

$$\gamma_0 = 1.39 e^{-4457/T_v} \quad (4)$$

$$\gamma_N = 49.21 e^{-6571/T_v} \quad (5)$$

In each of these measurements  $\gamma_N$  and  $\gamma_0$  values for the Ni reference were assumed to be 0.1 and 0.0085 for a wall temperature of 311 K. The value of  $\gamma_N$  is the average of many determinations from several research groups, which differ by more than three orders of magnitude for comparable temperatures.<sup>12-17</sup> Variations in the values reported for  $\gamma_0$  are less extreme. Both sets of measurements incorporate values of  $\gamma$  determined from heat transfer experiments. These measurements are quite difficult to interpret because experiments in which these atoms are created also have energetic species carried along in the flow, such as  $O_2(^1\Delta)$  and  $O_2(X,v \gg 0)$  in O-atom experiments and  $N_2(A^3\Sigma_g^+)$ ,  $N_2(a'^1\Sigma_u^-)$ , and  $N_2(X,v \gg 0)$  in N-atom experiments. These species may contribute significantly to the heat transfer to the surface and produce erroneously high results. Other experiments utilizing flow reactors have reported values of  $\gamma$  which are compromised by the necessity of making complicated diffusion corrections to the measured values.

The purpose in conducting these measurements was to obtain a detailed energy balance for the recombination/deactivation process. The measurements above assumed that energy accommodation and molecular deactivation were both identical functions of temperature, when it is quite possible that the extent of atomic recombination and thermal accommodation are only marginally related. To date, only Halpern and Rosner<sup>18</sup> have measured values of  $\gamma'$  and  $\beta$  independently as a function of temperature. Their study of N-atom recombination on metallic surfaces (other than Ni) demonstrated that  $\gamma$  and  $\beta$  may have completely different dependences with temperature. This may come into play in model calculations where temperature profiles and atom concentrations are calculated for flow along a body. The cumulative errors resulting from a flawed coupling of these two phenomena could be large. Our approach has been to measure the direct chemical loss of species under controlled or single collisions conditions and to couple these measurements with efficiencies for excited product formation and direct energy deposition whenever

possible. Subsequent deactivation of excited products is also important when these products have a high probability of contact with the surface and when quenching efficiencies are high.

#### Measurement Methods

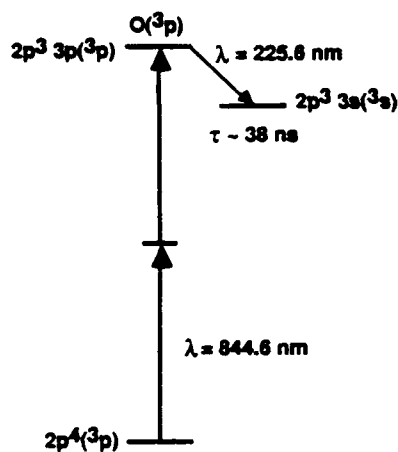
One of the unique features of our measurement program is the application of advanced laser-based diagnostics to probe species concentrations and properties in reacting flows over surfaces. These techniques are now in use in many small scale laboratory experiments, such as ours, and may be directly transferable to large scale systems for non-intrusive measurements of flow properties. Our current measurements have focused on the measurement of O- and N-atoms, as well as the metastable species  $O_2(a'^1\Delta)$  and  $N_2(X,v \gg 0)$ . We will describe measurement techniques for the detection of O-atoms,  $O_2(a'^1\Delta_g)$  and  $N_2(X,v \gg 0)$  in this paper. Catalytic properties of O-atoms and  $O_2(a'^1\Delta_g)$  determined using these techniques will be presented.

The detection techniques employ either laser-induced fluorescence (LIF) or resonantly enhanced multiphoton ionization spectroscopy (REMPI) to detect these species. In LIF a laser is employed to excite an atom or molecule from either the ground state or an excited state of interest to a higher lying excited state. Fluorescence from this excited state is then observed and may be quantitatively related to the density of the state excited by the laser.

In REMPI spectroscopy a high power pulsed tunable laser is used to provide high photon fluxes such that a molecule absorbs a sufficient number of photons to ionize. The ions are detected by measuring the current flow in the gas using a set of biased electrodes or other suitable ion detection device. The MPI process can usually be described as occurring in two steps: 1) the absorption of  $m$  photons to a real intermediate electronic state of the molecule, and 2) the absorption of  $n$  more photons, perhaps proceeding through several intermediate electronic states of the molecule, until ionization is achieved. In practice, the  $m$  photon step is almost always rate limiting and by scanning the frequency of the probe laser one observes a spectrum characteristic of this transition. The entire process is commonly referred to as an  $m+n$  process.

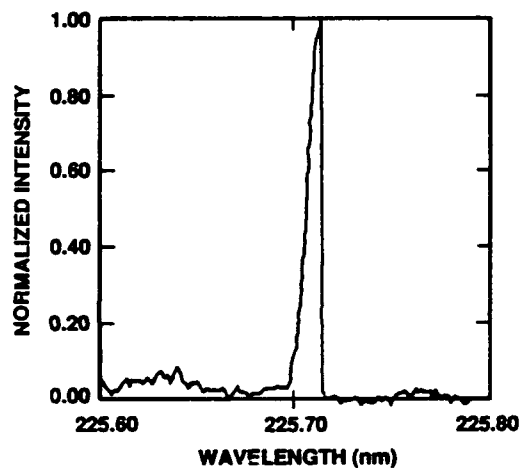
Oxygen atoms were detected using a recently developed<sup>19-22</sup> two-photon laser-induced fluorescence method. In this detection scheme O-atoms are excited from the  $2p^4(^3P)$  ground state to the  $2p\ 3p(^1P)$  excited state using simultaneous absorption of two photons at 225.6 nm from our tunable laser system. The excited state is metastable with respect to fluorescence to the ground state but does radiate to the  $2p^3s(^3S)$  state at 844.6 nm with a lifetime of 38 ns. This detection scheme is shown schematically in Fig. 1. Figure 2 shows an excitation spectrum of O-atoms obtained by scanning the laser wavelength while recording the total fluorescence emitted. The spectrum clearly shows the characteristic single line expected for the atom  $^3P_2 \rightarrow ^3P_{0,2}$  absorption transition.

Our experiments to measure  $O_2(^1\Delta)$  deactivation were conducted using multiphoton ionization detection on the  $d^1\Pi - a^1\Delta$  transition. This process



A-8449

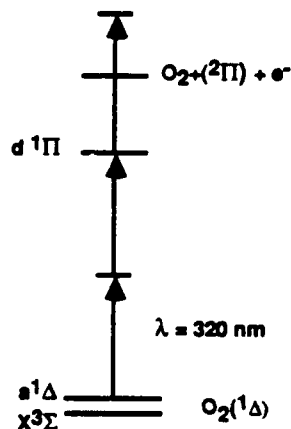
Fig. 1 Schematic Diagram of Energy Levels Employed in Two-Photon LIF Detection of O-Atoms



A-3911a

Fig. 2 Excitation Spectrum of O-Atoms Observed in Flow Reactor

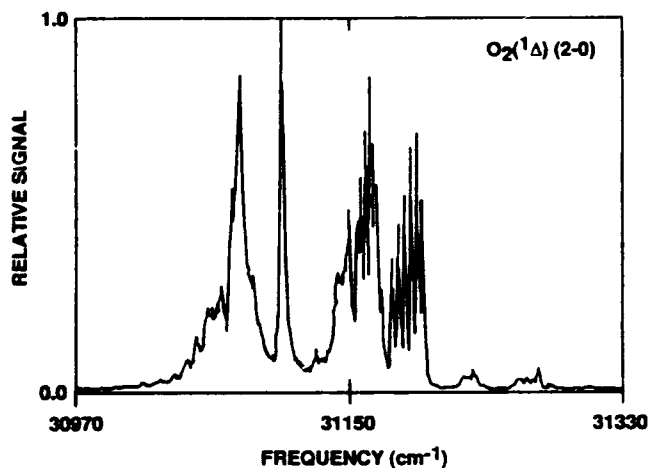
involves the absorption of two photons by  $O_2(^1\Delta)$  to the  $d^1\Pi$  state followed by subsequent absorption of a third photon to form the  $O_2^+(^2\Pi)$  ion. This process is illustrated schematically in Fig. 3.



A-8450

Fig. 3 Schematic Diagram of  $O_2(^1\Delta)$  Energy Levels Used for MPI Detection

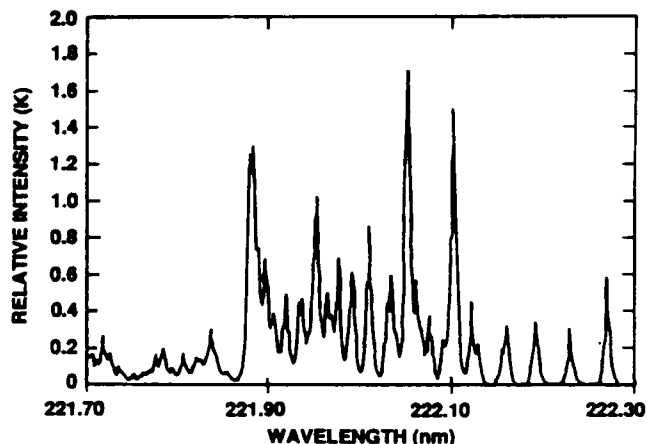
The initial simultaneous absorption of the two laser photons is the rate limiting step in the excitation process. Hence, the spectrum observed when the excitation laser is tuned in wavelength is one characteristic of the  $d^1\Pi-a^1\Delta$  transition (Fig. 4). The two-photon nature of the absorption is confirmed by recording the observed signal as a function of applied laser power while the laser wavelength is set to the peak of one of the d-a bands.



A-8466

Fig. 4 MPI Spectrum of  $O_2(^1\Delta)$  Excited Using the  $d^1\Pi-a^1\Delta$  2-0 Transition

The detection of  $N_2(X,v \gg 0)$  can be accomplished using REMPI by either a 2+2 excitation scheme for lower vibrational levels (0-4) or a 1+1 scheme for higher levels (>8). In both mechanisms the intermediate level is the  $a^1\Pi_g$  state. This state is long-lived ( $\tau \sim 80 \mu s$ ) and is predissociated for vibrational levels above  $v'=6$ . Hence it is a poor candidate for LIF detection of  $N_2(X,v)$ . However, the higher vibrational levels may be observed quite effectively using the 1+1 MPI detection scheme. A spectrum of the a-X 10-19 band (Fig. 5) dramatically indicates the high signal levels obtainable for  $v''=19$  of ground state  $N_2$  for densities of approximately  $10^{14}$  molecules  $cm^{-3}$ .



A-8487

Fig. 5 MPI Spectrum of  $N_2(a-X)$  10-19 Band Observed via a 1+1 Ionization Sequence

Our initial experiments were conducted at surface temperatures of 295 K to test the validity of the measurement techniques for measuring surface deactivation probabilities. Samples of reaction cured glass (RCG) coated quartz and polycrystalline Ni reference material were chosen for evaluation.

The experiments were conducted in a conventional discharge flow reactor. The apparatus is shown schematically in Fig. 6. The flow reactor was constructed entirely of Pyrex glass sections with an i.d. of 22 mm. Sections of the flow reactor were externally blackened with paint to eliminate interference from scattered room lights and internally coated with halocarbon wax to minimize wall recombination efficiencies for atoms and metastables.

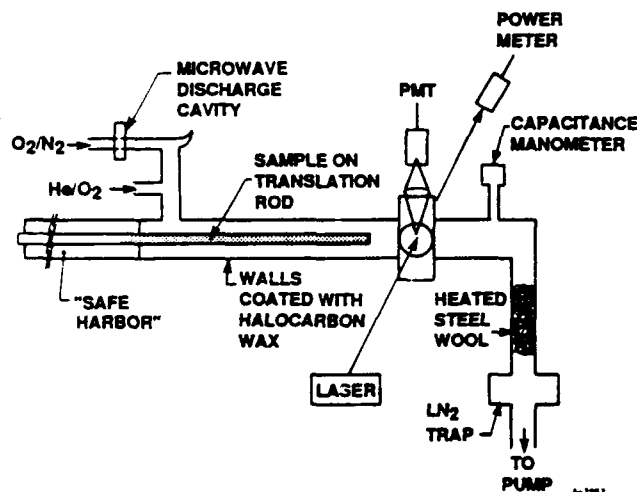


Fig. 6 Schematic diagram of discharge flow reactor apparatus used in Phase I studies.

The detection region of the flow reactor was formed from a six-arm glass cross. The gas flow through the reactor was along one axis of the cross while a second axis was used to allow the passage of the detection laser beam through the cell. The (third) vertical axis of the detection cross was used to mount either an MPI detection electrode system, a filtered photomultiplier tube, or an optical multichannel analyzer (OMA). Upstream of the detection volume a 50 cm long section of tubing formed the free flowing section of the flow reactor. This section was internally coated with halocarbon wax but was left transparent in order to determine the location of the sample in the reactor. Attached to the upstream end of the free-flowing section of the reactor was a multi-ported glass section having multiple ports for introduction of metastable molecules or atoms into the flow reactor. Each of the species studied was produced using a 2450 MHz microwave discharge in parent gases, with and without Ar or He codischarged diluent gases. These discharges were conducted in a side arm equipped with a Wood's horn to prevent any scattered light from entering the flow reactor. The discharge section was equipped with an additional side arm to allow the introduction of a diluent gas downstream of the discharge tube. In this manner the bulk flow velocity of the gas in the flow tube could be varied independently of discharge conditions.

Samples were introduced into the main section of the flow reactor from a chamber located upstream of the discharge ports. Sections of RCG-coated quartz rod (6 mm o.d.) were connected to form a section approximately 75 cm long and mounted on the end of a 6.25 mm o.d. section of solid copper rod. The copper rod was mounted in a vacuum fitting which allowed the rod to slide along the main axis of the reactor. The lengths of the copper rod and upstream "safe harbor" storage chamber were such that the RCG coated surface could be completely withdrawn into the storage chamber without exposure to the outside atmosphere and could be inserted into the flow of metastables or atoms for a distance of almost 50 cm. In this way varying lengths of the sample could be exposed to the reactant flow without contamination due to handling or exposure to atmosphere constituents. Sections of Ni rod were handled in the reactor in a similar manner.

Reactant gas flows were measured using calibrated rotameters and regulated using fine metering valves. The flow reactor was capable of achieving flow velocities of approximately  $1200 \text{ cm s}^{-1}$  at a pressure of 1 torr using He as a carrier gas. Somewhat slower flow velocities were achievable using  $\text{O}_2$  or  $\text{N}_2$  as the carriers.

The excitation laser employed in our detection system was a pulsed, Nd:YAG-pumped tunable dye laser (Quantel International). The laser has a pulse duration of approximately 15 ns and a bandwidth of  $0.08 \text{ cm}^{-1}$  in the visible region. A variety of laser dyes and dye mixtures (R590, R610, DCM, LDS 698) were employed to produce light in the region from 560 to 700 nm at pulse energies as large as 130 mJ and repetition rates of 10 pps. Our studies required the use of light tunable over the 225 to 340 nm region, hence, non-linear frequency generation techniques were employed.

### Results and Analysis

Evaluation of the variation in species concentrations to determine homogeneous, and to a lesser extent, heterogeneous decomposition rate coefficients using discharge flow reactors has been extensively reviewed in the literature.<sup>23</sup> The analysis of our data is simply an extension of the analysis developed for tubular flow reactors to a system where a concentric tube with a uniform deactivation probability has been inserted into the reactor. The range of deactivation probabilities which may be determined using a flow reactor is limited to values less than about 0.01. For probabilities greater than 0.01, the rate limiting step in the deactivation process becomes diffusion of the atom or molecule through the gas to the surface, rather than the actual deactivation step, and the process is considered "diffusion-controlled." Under these conditions a radial concentration gradient develops in the flow reactor. For deactivation probabilities below 0.01 the atom or molecule may traverse the diameter of the flow reactor many times before undergoing a deactivating collision and no radial concentration gradient should be present. Though corrections can be made to account for diffusion in the diffusion-controlled regime, the corrections often require the knowledge of binary diffusion coefficients for complicated mixtures involving excited states, which are seldom available and not easy to calculate. Hence, in this regime a flow reactor is of limited utility and measurements of

high-efficiency deactivation coefficients is best left to surface scattering experiments.

All of our measurements were made under conditions where the "plug flow" analysis of the deactivation process is appropriate and we present our solution for the case of the concentric rod below. In this regime the time-dependent loss of the species of interest is a first order process and may be given by

$$\frac{d[N^*]}{dt} = -k_v[N^*] \quad (6)$$

where  $k_v$  is the wall deactivation rate coefficient and  $[N^*]$  is the concentration of species  $N^*$ . The deactivation rate coefficient,  $k_v$ , can be simply expressed in terms of a deactivation probability,  $\gamma$ , the collision rate per  $\text{cm}^2$  per molecule,  $\bar{c}/4\pi$ , and the surface to volume ratio for the reactor ( $2/r$  for a hollow tube):

$$k_v = \frac{\gamma \bar{c}}{2r} \quad (7)$$

where  $\bar{c}$  is the average molecular velocity and  $r$  is the tube radius. When a concentric tube is inserted into the flow reactor expression (7) must be modified to account for the change in the surface to volume ratio of the reactor and the difference in deactivation probabilities for the surfaces of the tube and flow reactor walls. Under these conditions expression (7) becomes:

$$k_v = \frac{(\gamma_1 r_1 + \gamma_2 r_2)}{(r_2^2 - r_1^2)} \left(\frac{\bar{c}}{2}\right) \quad (8)$$

where the subscripts 1 and 2 refer to the surfaces of the inner concentric tube and the outer flow reactor wall, respectively.

The flow reactor is actually comprised of an initial section with the concentric insert (section a) and a final section without the insert (section b). Hence, the kinetic equations describing the loss of the species of interest must be solved for transit through each of these sections. The decay of the species in each section of the flow reactor is still first order, but the final concentration of the species after traversing section a becomes the initial concentration for a traversal of section b. The integrated rate equations for travel through each section are given in expressions (9) and (10):

$$N_f^a = N_o^a e^{-k_v^a l^a/v^a} \quad (9)$$

and

$$N_f^b = N_o^b e^{-k_v^b l^b/v^b} \quad (10)$$

where the flow time through each of the sections has been replaced by the length of the section divided by the linear flow velocity,  $l/v$ . The linear flow velocities can be expressed in terms of the tube cross sectional area and temperature, the gas pressure,  $P$ , and the measured gas molar flow rate,  $n$ :

$$v^a = \frac{nRT}{\pi P (r_2^2 - r_1^2)} \quad v^b = \frac{nRT}{\pi P r_2^2} \quad (11)$$

Combining expressions (7) through (11) gives an equation relating the measured species concentration at the detection cross to the deactivation coefficients of the concentric tube and reactor wall in terms of the molar gas flow rate, the section lengths and tube radii, and the gas temperature and pressure. This is given in expression (12):

$$\ln[N_f^b] = \ln[N_o^a] - \left(\frac{2\pi}{nRT}\right)^{1/2} \frac{P}{nN_o} [\gamma_1 r_1 l^a + \gamma_2 r_2 (l^a + l^b)] \quad (12)$$

A plot of  $\ln[N^*]$  with respect to  $l^a$  (expression (13) gives the value of  $\gamma_1$  independent of the properties of the flow reactor walls):

$$\frac{d \ln[N^*]}{dl^a} = -\left(\frac{2\pi}{nRT}\right)^{1/2} \frac{P}{nN_o} \gamma_1 r_1 \quad (13)$$

This measurement technique will not be very sensitive for determining  $\gamma_1$  if the product  $\gamma_1 r_1$  is much less than  $\gamma_2 r_2$  and, since  $r_2 > r_1$ ,  $\gamma_2$  must be as small as possible to detect small deactivation probabilities.

#### $O_2(^1\Delta_g)$ Quenching

This variable contact length method for measuring  $\gamma$  for  $O_2(^1\Delta)$  on RCG was initially employed with pure  $O_2$  at a flow velocity of  $80 \text{ cm s}^{-1}$  and gave a value of  $(1.5 \pm 0.2) \times 10^{-4}$ . Other measurements were performed using this technique for a higher flow velocity of  $125 \text{ cm s}^{-1}$  using both a pure  $O_2$  flow and an  $O_2/\text{He}$  mixture in which the  $O_2$  mole fraction was 0.63. Each of these measurements gave a value of  $(1.7 \pm 0.3) \times 10^{-4}$ . A plot of this data is shown in Fig. 7. All three of these measurements agree to within experimental errors and show that the measured value of  $\gamma_1$  is independent of gas composition and flow velocity over this range. The average value of  $\gamma_1$  from these three determinations is  $(1.6 \pm 0.3) \times 10^{-4}$ .

The deactivation of  $O_2(^1\Delta)$  on Ni was also studied using the variable contact method. These data are shown in Fig. 8 for conditions of  $100 \text{ cm s}^{-1}$  flow velocity and pure  $O_2$  gas composition. Some obvious curvature exists in the plot at short contact lengths and we have extracted a quenching efficiency of  $(1.9 \pm 0.4) \times 10^{-4}$  from the data for longer contact lengths. The deviation from linearity at short contact lengths is potentially due to imperfect flow development when gas from the injector enters the main body of the flow reactor, though one might expect to observe the same behavior for the RCG surface if this were the case. A second possibility is that some O-atoms which do survive through the injector to enter the flow reactor recombine to form some  $O_2(^1\Delta)$ , resulting in a lower observed value of  $\gamma_1$  for short contact lengths (where the O-atom concentration is greatest). Finally, there may be spatial inhomogeneities in the surface properties of the rod, through contamination or incomplete passivation, which

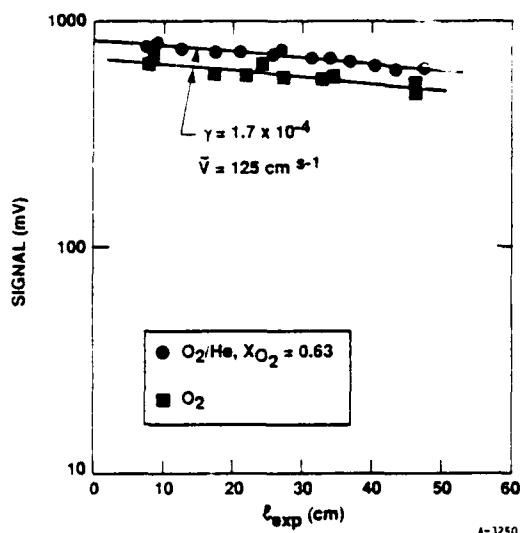


Fig. 7 Dependence of  $O_2(^1\Delta)$  deactivation coefficient on  $O_2$  mole fractions of 1.0 and 0.63 at constant pressure and flow velocity.

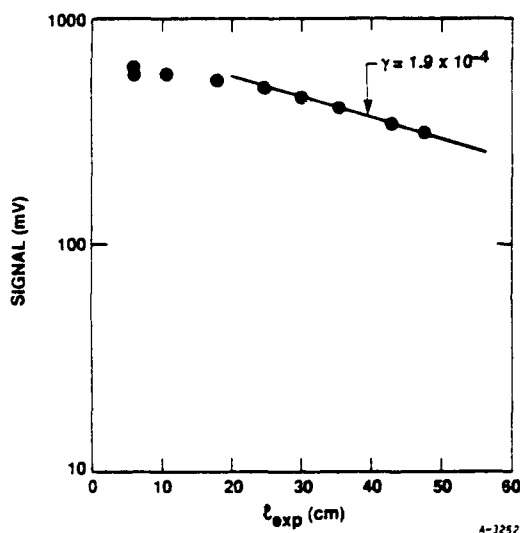


Fig. 8 Variation in  $O_2(^1\Delta)$  signal with contact length for an Ni surface.

could lead one end of the rod to have different properties than the other.

#### Oxygen Atom Quenching

O-atoms were produced in the flow reactor using flows of pure  $O_2$  through a 100 W microwave discharge at a pressure of 2 torr. Under these conditions strong air afterglow signals were observed in the reactor.

Oxygen atom quenching on Ni was studied at pressures of 1, 2, and 4 torr at a constant flow velocity of  $220 \text{ cm s}^{-1}$ . This flow velocity was considerably larger than employed in the  $O_2(^1\Delta)$  quenching studies but was the minimum flow for which appreciable O-atoms could be measured coming from the discharge. The studies were conducted at these three pressures in order to verify that diffusion was not the rate limiting step in the

deactivation process. If diffusion was important we would expect to find the measured value of  $\gamma_1$  decrease with pressure since the diffusion coefficient varies inversely with pressure. The quenching plot for the experiment at 1 Torr is shown in Fig. 9. The values of  $\gamma_1$  obtained from these experiments are  $(8.9 \pm 2.1) \times 10^{-4}$ ,  $(12.1 \pm 3.2) \times 10^{-4}$ , and  $(7.8 \pm 1.6) \times 10^{-4}$  for pressures of 1, 2, and 4 torr, respectively. There is clearly no trend with pressure in these data, which yield an average value of  $(9.6 \pm 2.4) \times 10^{-4}$ . Thus, diffusion does not play a major role in determining the deactivation rate. There also seems to be little evidence of curvature in the data for short contact lengths, in contrast to the data on  $O_2(^1\Delta)$ .

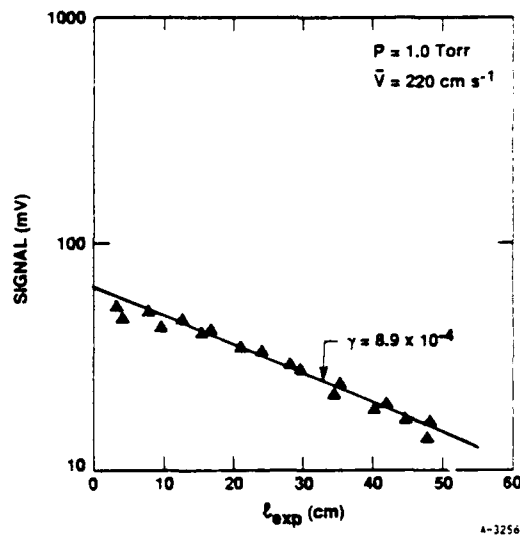


Fig. 9 Quenching plot for O-atoms on Ni at 1 torr total pressure.

In contrast to Ni, O-atom deactivation on RCG is nearly five times less efficient. The RCG experiments were conducted at a pressure of 1.0 torr and a flow velocity of  $220 \text{ cm s}^{-1}$ . The quenching plot in Fig. 10 shows a very low level of decay over the range of contact length employed and yields a value for  $\gamma_1$  of  $(2.0 \pm 0.3) \times 10^{-4}$ .

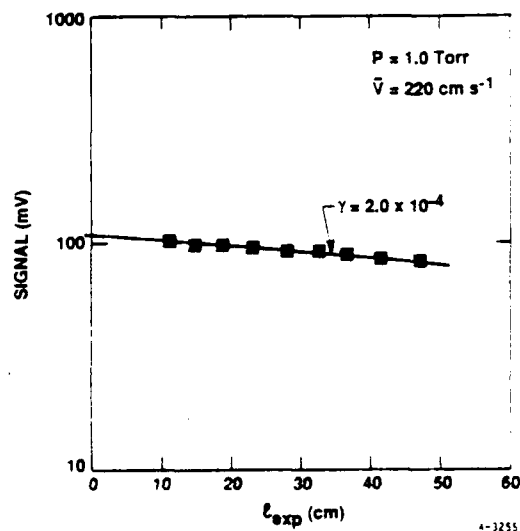


Fig. 10 Variation in O-atom signal with contact length for deactivation on RCG at 1 torr total pressure.



## Discussion

The results presented here for  $O_2(^1\Delta)$  and O-atoms on Ni and RCG are summarized in Table 1. Little quantitative work has been reported for

Table 1 Measured deactivation/recombination parameters

Species	RCG	Nickel (NiO)
$O_2(^1\Delta_g)$	$1.6 \pm 0.3 \times 10^{-4}$	$1.9 \pm 0.4 \times 10^{-4}$
$O(^3P)$	$2.0 \pm 0.3 \times 10^{-4}$	$9.6 \pm 2.4 \times 10^{-4}$

$O_2(^1\Delta)$  deactivation on surfaces other than Pyrex and various passivating coatings, such as  $H_3PO_4$ , halocarbon wax, and Teflon. Similarly, there are few reported results for quenching of excited states on RCG-type surfaces. Hence, comparisons with other workers in the field are somewhat difficult. A larger body of knowledge exists about N- and O-atom quenching, and we can compare our results to these studies. Where information about quenching on RCG surfaces at room temperature is lacking, we will try to compare our results to measurements on Pyrex, since both are silica-type structures.

Our deactivation measurements of  $O_2(^1\Delta)$  on RCG and Ni give values for  $\gamma_1$  of  $(1.6 \pm 0.3) \times 10^{-4}$  and  $(1.9 \pm 0.4) \times 10^{-4}$ . They show little difference between the behavior of the two surfaces. The results for quenching by RCG can be compared to several measurements for quenching by Pyrex.<sup>24,25</sup> These values average approximately  $2 \times 10^{-5}$ , but were measured as part of homogeneous kinetics studies conducted in flow reactors. These surfaces were passivated to varying degrees with  $H_3PO_4$  coatings, and reports of higher deactivation efficiency with uncoated walls are given. Our results are nearly a factor of 10 higher, but are for a  $(SiB_4)_n$  type surface which may behave differently. Due to the relatively low number density of O-atoms in these experiments, we believe these measurements are probably not affected by quenching of O-atoms to form  $O_2(^1\Delta)$  in the reactor. Comparable measurements could not be found for Ni; however, observations of surface catalyzed chemiluminescence from excited states of  $O_2$  formed from O-atom recombination on Ni screens by Harbeck and coworkers<sup>26,27</sup> and Ogryzlo and coworkers<sup>28-30</sup> provides qualitative evidence that the quenching is not efficient. Little can be said about the mechanism for the quenching process. In particular the question arises as to the disposition of the nearly 1 eV in electronic energy available from the  $a^1\Delta$  state. Direct energy transfer to the surface is possible but the internal conversion of electronic energy to vibrational energy in the ground electronic state cannot be overlooked.

Quenching of O-atoms on RCG has been investigated by Scott,<sup>31</sup> but at temperatures greater than 1400 K. Extrapolation of the Arrhenius expression given in Eq. (2) to 300 K does not give realistic values for  $\gamma_1$ . Our results for O-atom removal on RCG ( $\gamma_1 = (2.0 \pm 0.3) \times 10^{-4}$ ) are consistent with values of  $1.8 \times 10^{-4}$  by Greaves and Linnett<sup>32</sup> and  $1.3 \times 10^{-4}$  by Melin and Madix<sup>33</sup> for removal by Pyrex. Removal efficiencies for O-atoms of  $7.1 \times 10^{-4}$  for silica were reported by Greaves and

Linnett<sup>32</sup> as well. Greaves and Linnett reported that  $\gamma_1$  varied rapidly, but in a non-Arrhenius type manner, with temperature. The efficiency for O-atom removal increased to a value of  $1.4 \times 10^{-2}$  at 600 K. This non-Arrhenius behavior is consistent with the poor agreement of the present results with an extrapolation of Scott's results to 300 K.

Oxygen atom removal by Ni surfaces have also been reported by several groups. Myerson<sup>34</sup> observed an efficiency of 0.0085 for Ni while Greaves and Linnett<sup>35</sup> have reported 0.028 and Melin and Madix<sup>35</sup> 0.017. Somewhat lower values of  $\gamma$  have been observed for Ni oxide type surfaces, to which ours is probably quite similar. Greaves and Linnett<sup>36</sup> obtained a value of 0.0077 and 0.0089, while Breen and coworkers<sup>37</sup> have obtained a value of 0.01. These values are quite similar (the average is 0.0089) though the techniques used to distinguish between Ni and NiO surfaces in these various studies are not readily apparent. Hence, the differences between the Ni and NiO values reported may be more a matter of technique or surface preparation than actual catalytic efficiency. Our results for O-atom removal on Ni are nearly a factor of 10 lower than the average for the NiO studies for comparable temperatures. We have demonstrated that our results are not biased due to radial diffusion problems, though some curvature in the deactivation plot was observed. It is possible that the curvature extends further into the range of contact lengths than observed; however, other factors such as sample heating in the chamber or energy transfer to the surface from other species in the flow must also be considered for several of the other measurements.

A key factor concerning variation in efficiencies may be contamination of the surfaces. In our experiment we observed that our primary contaminant was pump oil, which was demonstrated to drastically increase the catalytic efficiency of the reactor walls. Careful attention was devoted to keep the system clean and to maintain highly passivated reactor walls. As stated previously, an initial incubation period was required to attain steady state conditions from which measurements could proceed. While this has been associated with the formation of a passivating oxide layer, it could also be due to the oxidation of contaminants on the surface to form an inert coatings. In spite of extreme care in all studies, possible surface contamination must be regarded as a prime reason for differences in measured results. These data point out the need for careful measures to properly clean materials to be tested or to prepare them in such a manner that they closely match the conditions of use. This treatment must be followed by routine examination of the surfaces to test for changes in their properties during the testing period.

Most of the studies reported above are basically heat transfer measurements where the role of excited state species is unsure. Clearly there exists a need for a systematic series of experiments in which the role of excited state species in the flow is eliminated or understood (i.e., no multiple collisions with the surface). Only then will the mechanisms for the formation of excited states be determined and subsequent deactivation probabilities for the excited states be available. This most certainly is required as deactivation probabilities approach unity and the reliability of

flow reactor measurements becomes questionable. These discrepancies between measurements also underscore the need for accurate surface characterization and cross comparison of samples. Our current research program described in the next section addresses some of these problems.

### Current Experiments

In contrast to the experiments reported above, molecular (atomic) beam-surface scattering experiments are done such that the species of interest undergoes a single collision with the surface of interest and then is removed from the reactor. The experiments are conducted in a low-pressure environment where sample cleanliness can be assured and verified. The vast amount of beam experiments done for chemical dynamics experiments have resulted in the development of highly specialized sources for the clean production of various chemical species, including an O-atom source which will be described below. In the past decade these sources have been directed towards the study of gas-surface interactions. Some of that work is summarized in a review by Cardillo.<sup>38</sup> The sample in these experiments may be isolated from external contamination and its properties, such as temperature, roughness, and surface composition may be varied in a straightforward manner. Because of the versatility of the beam-surface scattering technique and its ability to provide unambiguous single-collision results, we have chosen this technique for our high temperature experiments.

Due to the roughened nature of the surfaces which will be examined, scattering of atoms or molecules from these surfaces will most likely fall into the full  $2\pi$  steradians of solid angle available. Hence, to obtain a true picture of the recombination or quenching properties of the surface, the outgoing flux of the species must be measured over the entire scattering angle available in order to determine the integrated recombination or quenching efficiency. If the scattering is shown to be isotropic, then single point measurements can be employed to obtain further data. Similarly, if excited states are formed the production rate must be integrated over all scattering angles to obtain an integrated value. In general, the angle dependence of the scattering efficiency is obtained by rotating the diagnostic sensor in the scattering plane defined by incoming and outgoing specular components of the molecular beam. The incoming flux of the species of interest is determined by measuring its concentration in the beam prior to contact with the surface.

Our scattering apparatus is comprised of three vacuum chambers: the source chamber, the intermediate chamber, and the UHV chamber. A schematic diagram of the apparatus is given in Fig. 11.

The oxygen/nitrogen beam source we have chosen for the experiments was developed in the research group of Y.T. Lee at the University of California, Berkeley and has been thoroughly described in the literature.<sup>39</sup> The source consists of a high pressure (up to 350 torr) radio frequency discharge nozzle in which the discharge is conducted very close to the tip of the beam sampling orifice. When O<sub>2</sub>/Ar mixtures are employed in the source, O<sub>2</sub> dissociation efficiencies of greater than 80 percent have been observed. The O-atom beam is coupled into the intermediate chamber via a skimmer

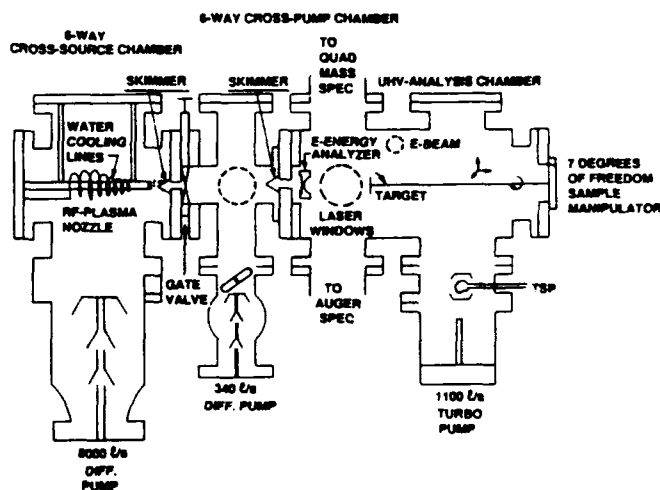


Fig. 11 Schematic diagram of O-atom/N-atom scattering experimental apparatus.

200  $\mu\text{m}$  in diameter and constructed of boron nitride to withstand the thermal load from the plasma source. The skimmer is placed 2.0 cm from the 0.076  $\mu\text{m}$  quartz nozzle orifice of the discharge. The discharge tube is constructed of quartz due to the large thermal load ( $\sim 200\text{W}$ ) and high plasma temperatures ( $T \leq 2000\text{ K}$ ) which are characteristic of the system. The RF discharge is water-cooled and powered by a standard RF plasma sprayer (500W capacity). Oxygen atom mean translational velocities from  $1.3$  to  $1.55 \times 10^5\text{ cm s}^{-1}$  ( $T > 2500\text{ K}$ ) have been measured. For O<sub>2</sub> seeded in Ar thermal Mach numbers of 3 to 4 are achieved.

After a single stage of differential pumping the O-atom beam enters the UHV sample chamber. This chamber is equipped with an Auger electron analyzer and quadrupole mass spectrometer for sample and beam characterization respectively. The sample is mounted on a manipulator with a resistive heater capable of heating the sample to 2000 K. Sample temperatures are determined using an optical pyrometer. All species are detected using REMPI detection methods described in the previous sections. The REMPI laser beam is focused by a 7.5 cm focal length lens mounted on a rotatable housing in the vacuum chamber. The system is configured to sample the incoming and outgoing atom beam 1.5 cm above the sample surface. Ions produced by the beam are accelerated to a microchannel plate by a 2.5 kV extraction grid. Signals from the detector are sent to a fast current amplifier and captured using a boxcar signal averager or high speed transient digitizer.

The efficiency of the RF discharge source for dissociation of O<sub>2</sub> is demonstrated in Figure 12. In this measurement our RF source was operated at a pressure of 55 torr with a 5 percent O<sub>2</sub>/Ar mixture. The O<sup>+</sup> ( $m/e=16$ ) signal was monitored with the mass spectrometer as a function of RF discharge power. The data indicates that the O<sub>2</sub> introduced to the chamber is fully dissociated, within our experimental errors. This is an important consideration in our measurements where we hope to be able to observe excited O<sub>2</sub> produced from atom recombination at the sample surface.

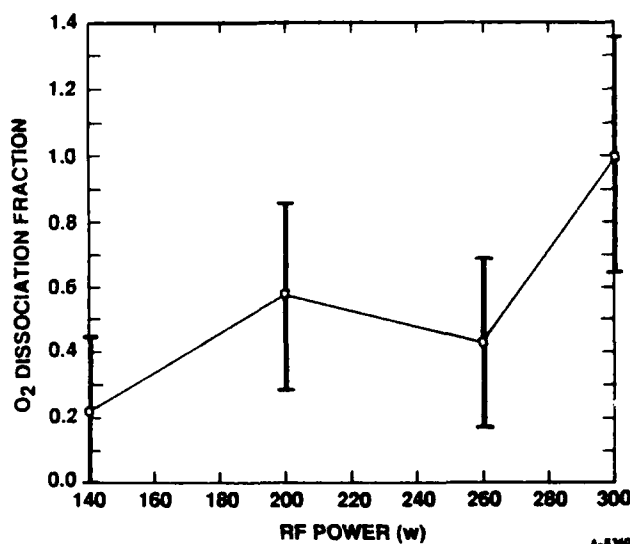


Fig. 12 O<sub>2</sub> dissociation fraction as a function of RF power in O<sub>2</sub>/Ar mixtures at 55 torr stagnation pressure.

Our current efforts are directed at measuring recombination efficiencies at temperatures up to 2000 K on reaction cured glass, coated carbon composites, and metallic structural materials. Initial measurements of O-atom recombination efficiencies are now underway.

#### Acknowledgement

This work is supported by NASA Johnson Center under Contract No. NAS9-17815. The author is grateful to B. David Green, John Campbell, Don Kaufman, Chris Gittins, and Terry Rawlins at PSI and Carl Scott at NASA JSC for their technical support.

#### References

- Hove, J.T., "Introductory Aerothermodynamics of Advanced Space Transportation Systems," *J. Spacecraft*, **22**, 19 (1985).
- Kelly, H.N. and Webb, G.L., "Assessment of Alternate Thermal Protection for the Space Shuttle Orbiter," AIAA Paper 82-0899, June 1982.
- Wurster, K.E., "An Assessment of the Impact of Transition on Advanced Winged Entry Vehicle Thermal Protection System Mass," AIAA Paper 81-1090, June 1981.
- Scott, C.D., "Catalytic Recombination of Nitrogen and Oxygen on High-Temperature Reusable Surface Insulation," AIAA Paper 80-1477, July 1980.
- Scott, C.D., "Space Shuttle Laminar Heating with Finite-Rate Catalytic Combination," reprinted from *Thermophysics of Atmospheric Entry* (Progress in Astronautics and Aeronautics, 1982), ed. by Thomas E. Horton, Vol. 82.
- Scott, C.D., "Effects of Nonequilibrium and Wall Catalysis on Shuttle Heat Transfer," *J. Spacecraft*, **22**, 489 (1985).
- Scott, C.D., "Catalytic Recombination of Nitrogen and Oxygen on Iron-Cobalt-Chromia Spinel," AIAA Paper 83-0585, January 1983.
- Rakich, J.V. and Lanfranco, M.J., "Numerical Computation of Space Shuttle Laminar Heating and Surface Streamlines," *J. Space. and Rockets*, **14**, 265 (1977).
- Stewart, D.A., Rakich, J.V., and Lanfranco, M.J., "Catalytic Surface Effects Experiments on the Space Shuttle," *Prog. in Astro. and Aero.: Thermophysics of Atmos. Entry*, **82**, 248, ed. by T.E. Horton (1982).
- Stewart, D.A., Rakich, J.V., and Lanfranco, M.J., "Catalytic Surface Effects of Space Shuttle Thermal Protection System During Earth Entry of Flights STS-2 through STS-5," Paper presented at Langley Conference on Shuttle Performance: Lessons Learned (1983).
- Rakich, J.V., Stewart, D.A., and Lanfranco, M.J., "Results of a Flight Environment on the Catalytic Efficiency of the Space Shuttle Heat Shield," AIAA Paper 82-0944, June 1982.
- Rahman, M.L. and Linnett, J.W., "Recombination of Atoms at Surfaces. Part 10. Nitrogen Atoms at Pyrex Surfaces," *Trans. Faraday Society*, **67**, 170 (1971).
- Goulard, R., "On Catalytic Recombination Rates in Hypersonic Stagnation Heat Transfer," *Jet Propulsion*, **28**, 737 (1958).
- Wood, B.J. and Wise, H., "The Interaction of Atoms with Solid Surfaces," *Rarefied Gas Dynamics*, Supplement 1, ed. by L. Talbot (Academic Press, New York, 1961).
- Dickens, P.G. and Sutcliffe, M.B., "Recombination of Oxygen Atoms on Oxide Surfaces, Part 1 - Activation Energies of Recombination," *Trans. Faraday Society*, **60**, 1185 (1964).
- Anderson, L.A., "Effect of Surface Catalytic Activity on Stagnation-Point Heat-Transfer Rates," AIAA J., **11**, 649 (1973).
- Pope, R.B., "Stagnation-Point Convective Heat Transfer in Frozen Boundary Layers," AIAA J., **6**, 619 (1968).
- Halpern, B. and Rosner, D.E., "Chemical Energy Accommodation at Catalyst Surfaces," *Chemical Society of London, Faraday Trans. I, Physical Chemistry*, **74**, 1883 (1978).
- Goldsmith, J.E.M., "Resonant Multiphoton Optogalvanic Detection of Atomic Oxygen in Flames," *J. Chem. Phys.* **78** (1983).
- Bischel, W.K., Perry, B.E., Crosley, D.R., "Detection of Fluorescence from O and N Atoms Induced by Two-Photon Absorption," *Appl. Opt.*, **21**, 1419 (1982).

21. Aldén, M., Hertz, H.M., Svanberg, S., and Wallin, S., "Imaging Laser-Induced Fluorescence of Oxygen Atoms in a Flame," *Appl. Opt.*, 23, 3255 (1984).
22. DiMauro, L.F., Gottscho, R.A., and Miller, T.A., "Two-Photon Laser-Induced Fluorescence Monitoring of O Atoms in a Plasma Etching Environment," *J. Appl. Phys.*, 56, 2007 (1984).
23. Howard, C.J., "Kinetic Measurements Using Flow Tubes," *J. Phys. Chem.*, 53, 3 (1979).
24. Yaron, M., Von Engle, A., and Vidaud, P.H., "The Collisional Quenching of  $O_2(^1\Delta_g)$  by NO and  $CO_2$ ," *Chem. Phys. Lett.*, 37, 159 (1976).
25. Winer, A.M. and Bayes, K.D., "The Decay of  $O_2(^1\Delta)$  in Flow Experiments," *J. Phys. Chem.*, 70, 302 (1966).
26. Mannella, G.G., Reeves, R.R., and Harteck, P., "Surface Catalyzed Excitations in the Oxygen System," *J. Chem. Phys.*, 34, 2177 (1961).
27. Mannella, G.G. and Harteck, P., "Surface-Catalyzed Excitations in the Oxygen System," *J. Chem. Phys.*, 34, 2177 (1961).
28. Kenner, R.D. and Ogryzlo, E.A., "Deactivation of  $O_2(A^3\Sigma_u^+)$  by  $O_2$ , O and Ar," *Int. J. Chem. Kinetics*, VII, 501 (1980).
29. Kenner, R.D. and Ogryzlo, E.A., "Quenching of  $O_2(c^1\Sigma_u^-)$   $v=0$  by  $O(^3P)$ ,  $O_2(^1\Delta_g)$  and Other Gases," *Can. J. Chem.*, 61, 921 (1983).
30. Kenner, R.D. and Ogryzlo, E.A., "Rate Constant for the Deactivation of  $O_2(A^3\Sigma_u^+)$  by  $N_2$ ," *Chem. Phys. Lett.* 103, 209 (1983).
31. Scott, C.D., "Catalytic Recombination of Nitrogen and Oxygen on High-Temperature Reusable Surface Insulation," *AIAA Paper* 80-1477 (1980).
32. Greaves, J.C. and Linnett, J.W., "The Recombination of Oxygen Atoms at Surfaces," *Trans. Faraday Soc.*, 54, 1323 (1958).
33. Melin, G.A. and Madix, R.J., "Energy Accommodation During Oxygen Atom Recombination on Metal Surfaces," *Trans. Faraday Soc.*, 67, 198 (1971).
34. Myerson, A.L., "Exposure-Dependent Surface Recombination Efficiencies of Atomic Oxygen," *J. Chem. Phys.*, 50, 1228 (1969).
35. Greaves, J.C. and Linnett, J.W., "The Recombination of Oxygen Atoms at Surfaces," *Trans. Faraday Soc.*, 54, 1323 (1958).
36. Greaves, J.C. and Linnett, J.W., "Recombination of Atom at Surfaces, Part 5 - Oxygen Atoms at Oxide Surfaces," *Trans. Faraday Soc.*, 55, 1346 (1959).
37. Breen, J., Rosner, D.E., and Delgass, W.N., et al., "Catalysis Study for Space Shuttle Vehicle Thermal Protection Systems," *NASA CR-134124*, 1973.
38. Cardillo, M.J., "Gas-Surface Interactions Studied with Molecular Beam Techniques," *Ann. Rev. Phys. Chem.*, 32, 331 (1981).
39. Sibener, S.J., Buss, R.J., Ng, C.Y., and Lee, Y.T., "Development of a Supersonic  $O(^3P)$ ,  $O(^1D_2)$  Atomic Oxygen Nozzle Beam Source," *Rev. Sci. Instrum.*, 51, 187 (1980).